Missouri S&T Library and Learning Resources

Scholars' Mine

Doctoral Dissertations | Student Theses and Dissertations

Spring 2020

Development of horizontal axis hydrokinetic turbine using experimental and numerical approaches

Abdulaziz Abutunis

Follow this and additional works at: https://scholarsmine.mst.edu/doctoral_dissertations

 Part of the Ocean Engineering Commons

Department: Mechanical and Aerospace Engineering

Recommended Citation

Abutunis, Abdulaziz, "Development of horizontal axis hydrokinetic turbine using experimental and numerical approaches" (2020). *Doctoral Dissertations*. 3028.
https://scholarsmine.mst.edu/doctoral_dissertations/3028

This thesis is brought to you by Scholars' Mine, a service of the Missouri S&T Library and Learning Resources. This work is protected by U. S. Copyright Law. Unauthorized use including reproduction for redistribution requires the permission of the copyright holder. For more information, please contact scholarsmine@mst.edu.

DEVELOPMENT OF HORIZONTAL AXIS HYDROKINETIC TURBINE USING EXPERIMENTAL AND NUMERICAL APPROACHES

by

ABDULAZIZ ABUTUNIS

A DISSERTATION

Presented to the Faculty of the Graduate School of the

MISSOURI UNIVERSITY OF SCIENCE AND TECHNOLOGY

In Partial Fulfillment of the Requirements for the Degree

DOCTOR OF PHILOSOPHY

in

MECHANICAL ENGINEERING

2020

Approved by:

K. Chandrashekhara, Advisor
Cheng Wang
Kelly Homan
Jonathan W. Kimball
V.A. Samaranayake

© 2020

ABDULAZIZ ABUTUNIS

All Rights Reserved

PUBLICATION DISSERTATION OPTION

This dissertation has been prepared in the form of three papers for publication as follows:

Paper I: Pages 18-58 have been published in the Journal of Renewable Energy.

Paper II: Pages 59-95 have been submitted to the Journal of Renewable Energy.

Paper III: Pages 96-157 are intended for submission to the Journal of Renewable and Sustainable Energy.

ABSTRACT

Hydrokinetic energy conversion systems (HECSs) are emerging as viable solutions for harnessing the kinetic energy in river streams and tidal currents due to their low operating head and flexible mobility. This study is focused on the experimental and numerical aspects of developing an axial HECS for applications with low head ranges and limited operational space. In Part I, blade element momentum (BEM) and neural network (NN) models were developed and coupled to overcome the BEM's inherent convergence issues which hinder the blade design process. The NNs were also used as a multivariate interpolation tool to estimate the blade hydrodynamic characteristics required by the BEM model. The BEM-NN model was able to operate without convergence problems and provide accurate results even at high tip speed ratios. In Part II, an experimental setup was developed and tested in a water tunnel. The effects of flow velocity, pitch angle, number of blades, number of rotors, and duct reducer were investigated. The performance was improved as rotors were added to the system. However, as rotors added, their contribution was less. Significant performance improvement was observed after incorporating a duct reducer. In Part III, a computational fluid dynamics (CFD) simulation was conducted to derive the optimum design criteria for the multi-turbine system. Solidity, blockage, and their interactive effects were studied. The system configuration was altered, then its performance and flow characteristics were investigated. The experimental setup was upgraded to allow for blockage correction. Particle image velocimetry was used to investigate the wake velocity profiles and validate the CFD model. The flow characteristics and their effects on the turbines performance were analyzed.

ACKNOWLEDGMENTS

I express my heartfelt gratitude to my advisor, Dr. K. Chandrashekhara, for his valuable guidance, assistance, and encouragement during my graduate study at Missouri University of Science and Technology. I thank him for his generous support of providing an excellent working environment and teamwork. It has been a great pleasure working with him.

I also want to express my genuine appreciation to my advisory committee members, Dr. Cheng Wang, Dr. Kelly Homan, Dr. Jonathan W. Kimball, and Dr. V.A. Samaranayake, for their valuable time and advice in the review of this dissertation.

Great appreciation goes to my teaching supervisor, Dr. S. N. Balakrishnan, for the valuable support, guidance, and encouragement he provided during my graduate teaching.

I also wish to thank my fellow colleagues—Mr. M. Fal, Mr. S. Ganguly, Dr. G. Taylor, Dr. H. Li, Dr. M. Mohamed, Dr. J. Nicholas, and Dr. R. Hussein—for their assistance during this and other research. My thanks are extended to my other fellow members for their help and advice.

I would like to acknowledge the financial support from the Department of Mechanical and Aerospace Engineering at Missouri University of Science and Technology in the form of a graduate research assistantship and a graduate teaching assistantship.

Finally, I wish to express my deepest gratitude to my wife, family, and my friends for their love, company, understanding, and encouragement. Without their support, especially my wife, I would not be able to accomplish and fulfill my goals.

TABLE OF CONTENTS

Page

LIST OF ILLUSTRATIONS

PAPER I Page

PAPER II

PAPER III

LIST OF TABLES

SECTION

1. INTRODUCTION

1.1. BACKGROUND ON HYDROKINETIC TURBINES

Hydrokinetic energy convergence systems (HECSs) are considered a promising technology for power generation. Unlike conventional hydropower turbines, HECSs can operate at zero hydraulic head and do not need structures to elevate the water level. Thus, HECSs are environmentally friendly and have a lower infrastructure cost. A horizontal axis hydrokinetic turbine (HAHkT) is a HECS that is categorized by the fact that its rotational axis is parallel to the flow direction. HAHkTs are intended to be deployed in water streams and marine currents in order to convert kinetic energy into mechanical energy and then into electricity by means of a rotor and generator, respectively. HAHkTs share many similarities with horizontal axis wind turbines (HAWTs) in terms of flow and load characterization and design process. These similarities allow for an exchange of knowledge between the two technologies. However, some important differences exist between the two technologies and should be considered during the design process (e.g., free surface and cavitation phenomenon).

1.2. HYDROKINETIC ENERGY POTENTIAL

Hydrokinetic energy is an excellent addition to the United States' renewable energy portfolio. A hydrokinetic system does not disrupt the flow of a river as a dam would because it is deployed in the free streams of the river. The Office of Energy Efficiency & Renewable Energy estimates a technical resource potential from river currents of up to 120

TWh/yr, 48% of which is in the lower Mississippi area, while 17% is in Alaska. Tidal streams, which are similar but with a bidirectional flow that follows the tide, add another potential of 222–334 TWh/yr (for perspective, total conventional hydroelectric production in 2015 was 251 TWh). In some cases, a hydrokinetic system can complement an existing structure, reducing the cost of installation and the environmental impact.

1.3. HYDRODYNAMIC DESIGN PARAMETERS OF HAHKTS

A HAHkT's performance is assessed by its power coefficient. Hydrokinetic turbines usually experience a low power coefficient if they are not optimized, which is the main barrier to the commercialization of this technology [1]. Optimization of HAHkTs is a challenging task that necessitates the comprehension of several interrelated design parameters such as pitch angle, angle of attack, solidity, number of blades, blockage, and flow characteristics. In this section, several important hydrodynamic parameters are presented.

1.3.1. Generated Power and Power Coefficient. The generated power (P) is calculated by the multiplication of the torque and turbine rotational speed. The power coefficient (C_P) is the ratio of the generated power to the kinetic energy passing through the turbine's swept area.

1.3.2. Pitch Angle and Angle of Attack. Pitch angle (θ) is a geometric characteristic and is measured as the angle between the hydrofoil chord and the rotational plane of the rotor. Alteration of θ allows for the control of the rotational speed and power output. The angle of attack (α) is the angle between the incoming relative flow and the hydrofoil chord. Optimizing α along a turbine blade is more challenging than that of a plane

wing because α along a turbine blade is affected by the angular velocity, radial location, and local pitch angle.

1.3.3. Tip Speed Ratio. Tip speed ratio (TSR) is also used to control the power output. The operational range of the TSR is the range in which the turbine operates at high efficiency. The tip speed ratio is calculated by dividing the tangential speed of the blade tip by the upstream flow velocity.

1.3.4. Solidity. Solidity (σ) has a large effect on turbine performance. For a single HAHkT, increasing the rotor solidity positively affects turbine performance. If the solidity is increased beyond its optimal level, the efficiency will start to decrease due to the increased flow impediment [2-4]. Turbine solidity is defined as the ratio of the sum of the chord length of all the blades to the circumference of the rotor

1.3.5. Lift and Drag Coefficients. Pressure difference and viscous stresses (caused by water flowing over blades) generate hydrodynamic forces that rotate the turbine. The pressure difference generates forces that are normal to the blades' surfaces. The viscous stresses generate forces that are both normal and tangential to the blade surfaces. However, the normal component of the viscous force is small and can be neglected. These forces are componentized into either parallel to the relative flow (drag force) or normal to the relative flow (lift force). The viscous forces mainly contribute to the drag component. The pressure forces contribute to both the drag and the lift components. When a hydrofoil stalls, the drag will significantly increase due to the increased pressure forces in the streamwise direction [5, 6]. The lift coefficient (C_L) and drag coefficient (C_D) are non-dimensional parameters that relate the lift and drag forces, respectively, to the dynamic pressure acting on the rotor's swept area. In hydrokinetic turbines, these coefficients are a

function of the angle of attack, local Reynolds number, rotational speed, and radial location.

1.4. STALL PHENOMENON

Hydrokinetic turbines have a similar flow dynamic principle to that of a hydrofoil. However, in turbines, α varies along the blade's span which results in varied sectional forces that rotate the turbine. When a sectional angle of attack (α_r) is within a moderate range, the chordwise flow is attached, and the sectional C_L is proportional to α_r. The sectional C_L continues to increase with α_r until it reaches an optimum value. Increasing α_r beyond its optimum value causes flow separation. At this condition, the blade section is said to stall, and the sectional C_L starts to decline. The stall happens because the flow on the upper side of the blade accelerates at the leading edge (LE) and generates a suction pressure region. The flow then deaccelerates (the pressure increases) as fluid moves along the chord so that the pressure at the trailing edge (TE) on the upper side is equal to that at the TE on the lower side. If the pressure increment is high enough, it may create an inverse flow close to the blade surface, which may lead to a separation [5].

1.5. WAKE CHARACTERISTICS

A wake is generated when the flow momentum obstructed by an object such as in the operating turbine case. The fluid applies a torque on the blades and rotates the turbine, and the blades exert an equal but opposite torque upon the passing flow. Consequently, the downstream flow rotates in a direction opposite to that of the blades, which reduces its axial momentum [7].

The wake can be divided into two regions based on the physics that govern the wake behavior: the near-wake region and the far-wake region [8]. The near-wake region extends streamwise from the rotor to a distance of about 1 rotor diameter [8-10] (25 rotor diameters in other references [11-13]). This region is highly influenced by the turbine's geometric characteristics. A significant pressure gradient is developed in this region, which controls the wake velocity deficit and wake expansion [10, 11]. The far-wake region is located farther downstream, and it is separated from the near wake by a transient-wake region. Here, the rotor shape impact is limited to the velocity deficit and the increased turbulence intensity [11]. Moreover, the far-wake structure is driven by convection and turbulent mixing [8, 9, 14]. The focus in this region is on the modeling of the wake, turbulence, and wake-interaction rather than the rotor [9, 10].

As the turbine is loaded, the thrust on its rotor increases. The increase in thrust results in a higher flow impedance, which causes the wake behind the rotor to slow down. A shear layer is developed as a result of the difference in the velocity between the flows inside and outside the wake. The shear layer thickness increases as the wake travels farther downstream. If the turbine is heavily loaded, a large amount of kinetic energy is converted to a large-scale turbulent motion, and the rotor enters the turbulent wake status.

The mixing of the low stream inside the wake with the fast stream in the surrounding outer region causes a momentum transfer. This in turn allows for wake expansion and flow recovery [8, 9, 15]. Studying wake development is essential for improving the performance of turbines that operate interactively at the same site such as in wind farms and multi-turbine systems.

1.6. BLOCKAGE EFFECTS

The flow characteristics around and behind a turbine operating in a confined environment differ from that when the same turbine operates in an open environment. When a turbine operates in a confined flow, it generates a partial blockage that affects the turbine performance. This blockage accelerates the flow speed at the rotor plane and enhances the system efficiency [16, 17]. The wake structure behind a constrained rotor is controlled by the surrounding effects, including walls, bed, or other wakes developed by neighboring turbines [13, 18]. This increases the dynamic pressure at the rotor plane, which generates a higher passing flow and thus a higher harnessed power when compared to a turbine operating in unconfined flow. The blockage effects are essential and should be considered when designing a hydrokinetic turbine.

2. LITERATURE REVIEW

Parametric studies on the various hydrodynamic design parameters of HAHkTs are essential to help grow our understanding of these parameters and their interactive effects on turbine performance. A computationally cheap yet satisfactory numerical model, such as BEM theory, is crucial for a preliminary investigation to provide a primary design of a HAHkT for an available operational environment. Furthermore, higher levels of fidelity provided by methods such as CFD simulations are also important for characterizing a hydrokinetic turbine system and its surrounding flow behaviors. In addition, an experimental study of a small-scale hydrokinetic turbine system is important in terms of the system's parametric study and validation of the developed numerical tools.

During the last two decades, several experiments and numerical simulations have been performed to understand flow dynamics and the effects of various aero/hydrodynamic factors on turbine performance. Nevertheless, few investigations have focused on the effect of solidity and pitch angle on small hydrokinetic turbine performance. To the best of the authors' knowledge, the following topics have not been covered in detail.

1. The use of artificial neural networks for enhancing the performance of blade element theory.
2. The use of multi-turbine systems to overcome the very high solidity effect and operational space limitation.
3. Solidity and blockage interactive effects on hydrokinetic turbine performance.

2.1. BEM THEORY: CONVERGENCE FAILURE

Blade element momentum theory is usually used in the preliminary design of HAWTs due to its relative simplicity and lower computational cost when compared to CFD simulation [19]. Because of the many similarities between the HAHkTs and HAWTs, many researchers have used the BEM model in the design of hydrokinetic turbines [20-23]. BEM theory uses iterative methods to solve the model's equations to obtain axial and tangential induction factors (*a* and *á*, respectively) and other aero/hydrodynamic properties [5, 21, 24]. During the iteration of the model, convergence failure is sometimes encountered [8-11], which is inconvenient and hinders the design process.

Several studies were performed in order to understand and eliminate the source of the convergence issue. Maniaci [25] suggested that a source of convergence failure was due to the singularity introduced by the drag term in the *á* equation when *a* approaches 1. To avoid the singularity, he eliminated the drag-dependent term from an adapted *á* equation in the region of high fluctuation close to the singularity. Masters et al. [26] employed Monte Carlo simulation to locate initial values of *a* and *á* that were not within local minima (local minima regions cause convergence failure). These initial values were used as a starting point for an optimizer to find the final values of *a* and *á* with less calculation effort. Nonetheless, these methods were reported to have convergence problems at some flow incidents [27].

Ning [27, 28] replaced the unknown induction factors in BEM's equations by both the local inflow angle (Ø) and the local velocity magnitude. He numerically solved for one variable, Ø, using a root-finding algorithm. The singularity was forced to occur only at specific inflow angles, namely $Ø = 0$ and $Ø = \pm \pi$. In this work, this model was programmed

to predict the performance of the small-scale turbine. The model was found to perform well up to a specific TSR after, which the results started to oscillate. Moreover, this model would require reformulation if a blockage correction model similar to [29] is integrated into the BEM theory.

2.2. PITCH ANGLE AND ANGLE OF ATTACK

Batten et al. [30, 31] showed that altering the pitch angle and the hydrofoil camber affects the stall mechanism and the cavitation appearance when water flows over marine current turbine blades. In their study, they have employed both experiments and BEM theory. Madrigal et al. [32] used a CFD simulation with a shear-stress transport (SST) k–ω turbulence model and showed that a small change in the blade pitch could slightly alter the C_P, but it also significantly modifies the blade loading. Thumathae and Chitsomboon [33] simulated a horizontal axis wind turbine with untwisted blades using the k–ε turbulence model. Using a section at 80% of the blade span, they suggested that an optimal angle of attack is close to the maximum C_L point rather than the maximum C_L/ C_D point (C_L/ C_D is considered when designing an aircraft wing). The pitch angle also controls the TSR operational range; a decrease in the pitch angle causes an increase in the operational range of the TSR [2, 4].

2.3. SOLIDITY AND NUMBER OF BLADES

Several experimental and numerical studies have been conducted to investigate the effects of solidity and blade number on wind/water turbine performance [2-4, 32, 34]. In

general, increasing the solidity and the number of blades had a favorable effect on the aero/hydrodynamic gains.

Subhra et al. [3] performed a CFD simulation and found that a 3-blade HAHkT with untwisted blades generated more power than both 2- and 4-blade HAHkTs with similar solidities. It was also observed that the power peak shifted to lower TSR as the solidity increased. Using a simple BEM model, Duquette and Visser [2] examined the effects of changing the solidity level and blade number on the performance of HAWT with untwisted blades. They found that at a fixed solidity, increasing the rotor blade number would yield an increased C_P at the peak. The optimum TSR was significantly influenced by the solidity variation but was only slightly affected by the change in the blade number. Madrigal et al. [32] studied the solidity effect on the performance of an axial water turbine when operated at a lower flow velocity than what it was designed for. The level of solidity was adjusted by changing the number of blades (though, the number of blades has its own effects on turbine performance regardless of the solidity variation [2, 3]). The range of power against different tip speed ratios shrunk as blades were added. The highest torque was produced by the 3-blade rotor, which corresponded to solidity of 0.21. The study also found that the C_P at the peak increased by 2% for each blade added, which was deemed to be not worth the blades added.

2.4. DUCT REDUCER AND DIFFUSER

A number of researchers have studied the duct components, as well as their inner and outer shapes. Their goal was to improve the turbine aero/hydrodynamic performance. The majority of these studies focused on the wind turbines, while a few studies considered

integrating the duct with water turbines. Even though wind turbine efficiency is increased when shrouded under ideal conditions, it has been argued that the additional cost of constructing a duct will far surpass the advantages. This is because of the increased weight and drag of the system that must be supported by the turbine tower. This is not the case for the water turbines where the duct weight effect is alleviated by the buoyant forces [35, 36]. Moreover, hydrokinetic turbines can assume that the flow is effectively fixed, and shrouding the rotor with a duct diffuser will further modify the flow and eliminate the need for yaw control.

Gilbert and Foreman [37] performed a series of experiments in a wind tunnel to study the effect of a duct diffuser on a wind turbine performance. They found that the efficiency of the ducted turbine improved by about 4.25 times that of the conventional bare turbine. They recommended that slots be made on the duct walls to control the boundary layer inside the duct. Setoguchi et al. [38] studied the performance of three types of duct diffusers that were characterized by different outer surface shapes. The ducts used had a circular cross section and were compromised of a front nozzle, a straight middle tube, and a tail diffuser with a flange around its exit. They confirmed that the duct diffuser with a straight-profile outer surface performed better than the base and bulge type duct diffusers. Nasution and Purwanto [39] investigated the effect of a diffuser's interior surface shape on its performance. Two conical diffusers were used, one with a straight-profile inner surface and another with an optimized airfoil-profile (curved) inner surface. The diffuser with the curved interior surface was capable of improving the local velocity by 65.5%. They noted that the reason for this high velocity augmentation was the increased formation of turbulence downstream the diffuser.

2.5. WAKE

Studying the wakes generated by turbines is essential to understand how these turbines may alter both the efficiency of and the loading on other downstream turbines [8]. Researchers have used several techniques such as flow visualization, small-scale turbines experiments, and numerical simulations to investigate the wake characteristics and the response of the turbines to the wake.

Stergiannis et al. [40] investigated the wake characteristics of two wind turbines placed in an array. They used k–ω and k–ε CFD turbulence models and incorporated a moving reference frame technique. The CFD solutions then were compared against a simplified actuator disk model (ADM). The k–ω model provided the least error when validated against experimental results from the first rotor wake. The ADM under estimated the velocity deficit inside the wake. Stevens et al. [41] used ADM and an actuator line model (ALM) in relatively coarse large eddy simulations (LES). The performance of ALM was better than the performance of ADM within the near-wake region. However, in the case of wind farm simulations, the performance of the ADM model was more accurate even farther downstream. Incorporating the nacelle in the simulation further improved the wake prediction, especially at the centerline. Chamorro et al. [42] used a three-dimensional (3-D) particle image velocimetry (PIV) system to investigate the wake behind a 3-blade HAHkT. They suggested that the near-wake expansion is proportional to $x^{1/3}$; where x is the streamwise distance. The tangential velocity near the tip of the blades was small because of the surrounding flow. Therefore, tangential velocity can be neglected in this region. The radial velocity was high near the tip of the blades and decreased toward the center due to the rotor symmetry. Mukherji et al. [3] performed a 3-D CFD simulation to

study the wake behind an axial hydrokinetic turbine. Expansion and decay of the wake were observed as the wake traveled downstream. The axial velocity deficit decreased significantly after two rotor lengths downstream. The radial and tangential velocities had smaller magnitudes compared to the axial velocity, signifying that the axial velocity component had the biggest effect on power extraction.

3. SCOPE AND OBJECTIVES

This dissertation is comprised of three papers. The first paper is titled "A Neural Network Approach to Enhance Blade Element Momentum Theory Performance for Horizontal Axis Hydrokinetic Turbine Application." In this paper, a modified BEM theory was developed to accurately predict the performance of a small-scale HAHkT with no convergence problems. Different BEM correction models, such as tip and hub losses, high induction factor thrust, and blockage effects were integrated to enhance the BEM performance. An XFoil-MATLAB interface was modified to calculate C_L and C_D over the operational range of the Reynolds number. A 2-D CFD simulation was used to validate XFoil's accuracy. A stall delay model was then employed to account for the rotational effect and adjust the 2-D lift and drag coefficients. The two neural networks (NNs) used to predict the C_L and C_D coefficients were integrated into the BEM model. Another two NNs were coupled with the BEM model to obtain the induction factors that failed to converge during the BEM iteration. The structures of the first two NNs (relating to C_L and C_D) were varied and their performances were observed. The NN structures with the highest correlation coefficients against XFoil were approved for integration into the BEM model. Experimental, classic, and modified BEM models were used to examine the performance of the proposed BEM-NN model. The proposed model successfully operated at higher $TSRs$ with no convergence failures when compared to other classic and modified BEM models. The integration of NNs as multivariate interpolation tools for C_L and C_D calculation further enhanced the BEM's accuracy. Moreover, this method was found to be easy to integrate into any modified BEM model.

The second paper is titled “Experimental Evaluation of Coaxial Horizontal Axis Hydrokinetic Composite Turbine System.” In this study, a multi-coaxial 3-blade HAHkT system was designed, built, and tested in a water tunnel. The purpose of this work was as follows: (a) to provide insight into the operating characteristics of the tested turbine system, (b) to overcome the rotor swept area constraints imposed by the operational space limitation such as in river streams and artificially-made channels, and (c) to mitigate the high solidity effect. The experimental setup was built and equipped with a clutch, time-averaged torque, and time-averaged rotational speed sensors for time-averaged power measurements. The acquiring and processing of the data were achieved with the help of LABVIEW software and MATLAB software. Experiments were conducted to understand the operating characteristics of a single 3-blade turbine by varying its tip speed ratio, pitch angle, and flow velocity. The effects of distance between rotors, rotors’ relative installation angle, and shrouding on the multi-turbine system performance were also investigated. The BEM theory was used to study the stall mechanism over the blades of the single-turbine system. A PIV system was utilized to study the wake generated by different turbine configurations. It was found that the two-turbine system had improved efficiency when compared to the single-turbine system. The third rotor also enhanced the turbine system efficiency, but its contribution was less compared to the second rotor due to the higher velocity deficit produced by the wake. The duct had a significant effect on the multi-turbine performance due to the accelerated flow through the turbine system.

The third paper is titled “Coaxial Horizontal Axis Hydrokinetic Turbine System: Numerical Modeling and Performance Optimization.” In this paper, a single-turbine and a multi-turbine system were modeled under different configurations, and their performance

was numerically evaluated and experimentally validated. The objective was to derive optimum design criteria for the proposed multi-turbine system. Solidity, blockage, and their interactive effects were numerically investigated. The configuration of the multi-turbine system model was altered by changing the number of rotors and the distances between them. Multi-fidelity simulations were performed in this study. A lower-fidelity Reynolds-averaged Navier–Stokes (RANS) model utilizing shear-stress transport (SST) k–ω turbulence model and moving reference frame (MRF) technique was used for power calculation, solidity and blockage effect investigation, and flow field examination. Sliding mesh modeling (SMM) was used to verify the calculation of SST k–ω utilizing MRF. A high-fidelity large eddy simulation (LES) was used to verify the RANS model's prediction of the wake. A grid independent study and time step effect study were performed to verify that the solution is independent of mesh characteristics and time step size, respectively. The power experiment setup was upgraded from the previous work which allowed for the thrust force measurement. The measured thrust data were used in the validation of the numerical results and in the blockage correction model. A rotor with optimum solidity was manufactured and integrated into both the single-turbine and multi-turbine systems for numerical validation and performance evaluation. A PIV system was utilized to evaluate the wake structure and validate the numerical results of the flow characteristics. The blockage effect was found to be more pronounced as solidity increased. The rotor with optimum solidity in the confined flow maintained its performance as the highest even in the unconfined flow environment. The performance of the multi-turbine system comprising three-rotors with optimum solidity was improved by about 47% compared to the single-turbine system with optimum solidity. Increasing the distance between rotors in the multi-

turbine system from 2 dia. to 4 dia. had an insignificant effect on system efficiency peak. However, the 4 dia. distance increased the range of operational tip speed ration (i.e., flattered the C_P peak). Increasing the number of rotors from three to five had slightly enhanced the performance by 4%. This was due to the wake/wake-interaction effects.

PAPER

I. A NEURAL NETWORK APPROACH TO ENHANCE BLADE ELEMENT MOMENTUM THEORY PERFORMANCE FOR HORIZONTAL AXIS HYDROKINETIC TURBINE APPLICATION

Abdulaziz Abutunis, Rafid Hussein, K. Chandrashekhara

Department of Mechanical and Aerospace Engineering

Missouri University of Science and Technology, Rolla, MO 65409, USA

ABSTRACT

Blade element momentum (BEM) theory is a commonly used tool to predict the performance of horizontal axis conversion systems, such as wind and water turbines. Moreover, BEM theory can be easily integrated into many optimization techniques to improve the turbine structure and performance reliability. BEM theory though conceptually simple has different sources of convergence issues. The main focus of this work was to introduce a computational intelligence technique, namely, multilayer perceptron (MLP) neural networks (NNs) to overcome the convergence issues regardless of their sources. To improve the BEM accuracy, NNs were also employed as a multivariate interpolation tool to calculate the lift and drag coefficients over an operational range of local Reynolds numbers. This technique was found to be easy to integrate into any modified BEM model such those account for blockage in channels. The BEM-NNs model was able to operate at a higher tip speed ratio, with no convergence problems, compared to other models. Integration of NNs as multivariate interpolation tool for hydrodynamic coefficient

calculation further improved the power prediction compared to that when using a constant representative Reynolds number

1. INTRODUCTION

Hydrokinetic energy conversion systems (HECSs) are used to generate electricity from rivers and marine currents. They convert the kinetic energy of flowing water into mechanical energy and then into electricity by the means of generators. The most known types of HECSs are horizontal axis hydrokinetic turbines (HAHkTs) and vertical axis hydrokinetic turbines (VAHkTs), though, most of the developed HECSs are the horizontal axis devices [1].

A hydrokinetic turbine success at a specific site is determined by the power it can generate at a competitive cost. Therefore, rotor hydrodynamic efficiency and structural sturdiness are essential factors that must be considered in the design stage. Testing a HAHkT performance experimentally in a water tunnel, over a possible operational environment, is a costly and time-consuming process. Therefore, it is imperative to construct a computationally cheap (fast) yet satisfactory method that allows evaluating a rotor performance and optimizing its blades hydrodynamic shape and structure.

Most of the current literature on energy conversion is based on wind turbines. BEM theory is a commonly used tool to evaluate the efficiency of horizontal axis wind turbines due to its relative simplicity and low computational requirements compared to computational fluid dynamics (CFD) [2]. Performing a higher fidelity unsteady 3D CFD simulation, such as Reynolds-Averaged Navier-Stokes (RANS) based turbulence models,

can resolve the detailed flow around a rotor's blade and can provide accurately predicted aero/hydrodynamic forces. These turbulence models incorporate the compressibility, rotational and 3D, transitional, and turbulence effects, which make them an accurate tool for turbine rotor modeling. However, this high accuracy comes at the expense of higher computational cost which makes it infeasible for the preliminary design stage of a turbine rotor where numerous simulations are required. In the availability of accurate airfoil aerodynamic characteristics (lift coefficient (C_L) and drag coefficient (C_D)), BEM theory offers quick and reasonable estimation of the generated power over a wide range of operational conditions. The theory can also satisfactorily predict the loading distribution along the blade; thus, it is an appropriate tool for preliminary aerodynamic and aeroelastic analysis and for providing conceptual modeling of axial HECSs blades.

BEM theory was first developed by Glauert [3] where the blade element and momentum theories were coupled to investigate propeller performance. BEM theory comprises various assumptions for simplicity. Several studies were performed later to improve the BEM theory by accounting for some of its inherent flaws, such as the assumption of an infinite number of blades, thrust at high induction factor, and skewed wakes [3-5]. A comprehensive discussion of the theory derivation and implemented corrections can be found in several textbooks and papers, for example [3, 4, 6-9]. Only the final equation forms will be presented in the relative sections of this work.

A HAHkT has similar operational principles to that of a wind turbine [9]. However, there are a number of essential differences, such as stall characteristics, Reynolds number (Re) variation effect, free surface effect and cavitation effect should be taken into consideration during the design phase [10, 11]. Due to the similarity between the two

technologies, several studies had applied BEM theory to HAHkT application, for example [10-13]. BEM theory formulates equations as a function of axial and tangential induction factors (a and a', respectively), and solves for these variables numerically, for instance, using fixed-point iteration [6], objective function [12], or Newton-Raphson method (solves only for a) [14]. Regardless of the solution technique, convergence failure is sometimes encountered during BEM theory iteration at some blade radial locations and operational conditions [15-18]. Convergence failure is inconvenient, especially during the design process.

Various studies were conducted to understand the convergence problem sources and to find numerical schemes that overcome the issue. Maniaci [18], attributed a type of convergence failure to the singularity caused by the drag term in the tangential induction factor (a') equation when axial induction factor is around unity ($a \approx 1$). To remove this singularity, he suggested a restricted elimination of drag-dependent term from a modified tangential induction factor equation in the region of extreme oscillation around the singularity. For maintaining smooth transition and continuity in the induction factors during the restricted elimination, a sine curve singularity transition model was used. Masters et al. [15] combined Monte Carlo algorithm and sequential quadratic programing. Monte Carlo was used to initiate a and a' with values that were not within a local minima (a source of convergence issue) and close to the final solutions. These values were used as an initial input for the optimizer. Nevertheless, these aforementioned schemes still struggle to converge at some instants [17]. Ning [16, 17] developed a method to insure induction factors convergence by replacing the unknown variables a and a' by the local inflow angle (ϕ) and local velocity magnitude. Using ϕ as unknown allows the update of the required

lift and drag coefficients without implementation of the induction factors. Consequently, the two equations developed in the classical BEM theory were reduced to one residual equation and the commonly used fixed-point iterative method was altered by a one-variable root-finding method, which eventually simplified the solution process. The technique was developed to impose the singularity to occur only at predefined instances ($\phi = 0, \mp \pi$). These boundaries were convenient since they separated the regions between the momentum/empirical region where $\phi \in (0, \pi)$ and the propeller brake region ($a > 1$) where $\phi \in (-\pi, 0)$. In the current work, this algorithm was coded and the results were compared to MLP-NN BEM model (see Section 6.3). The current models results agreed over most of the operational range. The model suggested in [16, 17] operated without a problem, but it would need fundamental changes if a blockage model such as in [19] would be integrated into BEM theory.

The main objective of this work was to integrate MLP-NNs algorithm into the BEM theory in order to predict the values of induction factors that failed to converge during the iteration process. Moreover, the NN approach also served as a multivariate interpolation tool to compute sectional C_L and C_D during the iteration at different operational incidents.

2. BLADE ELEMENT MOMENTUM THEORY

BEM theory combines momentum theory and blade element theory. The integration of both theories permits computing the reduced velocities and forces acting on the blade elements.

2.1. CLASSICAL MODEL

A control volume represents the flow passing a rotor is discretized into annular elements each corresponds to a blade element, as shown in Figure. 1a. The flow speed through an annular element cross-section is assumed a uniform, but it varies from upstream to downstream as shown in Figure. 1b. From the conservation of axial and angular momentum for an annular element, the differential thrust (dT_r) and torque (dM_r) on a blade element are

$$dT_r = 4\pi r \rho U_\infty^2 a(1-a)dr \quad (1)$$

$$dM_r = 4\pi r^3 \rho U_\infty \omega(1-a)a'dr \quad (2)$$

where ρ is the water density, U_∞ is the free stream velocity, ω is the blade angular velocity, and r and dr are the radial distance from the rotor center and the thickness of the annular element, respectively.

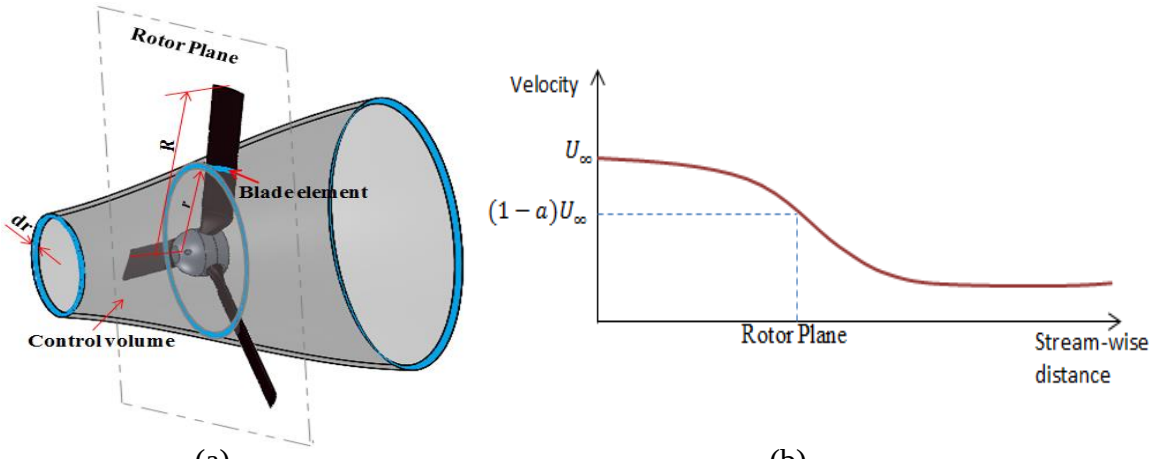

(a) (b)

Figure 1. (a) Annular element control volume with corresponding blade element and (b) flow speed variation along the stream through the control volume

Blade element theory assumes that the loads on a blade element are obtained by the hydrodynamic forces (lift and drag) of a given blade profile, which require the calculation of the local angle of attack (α_r) (shown in Figure. 2) and Reynolds number. The Reynolds number in this study was calculated based on the sectional relative velocity u_{r_rel} and referred to as a sectional Reynolds number (Re_r) which is given by

$$Re_r = \frac{u_{r\_rel} c_r}{\nu} \tag{3}$$

where c_r is the sectional chord length and ν is the kinematic viscosity of the working media (water). The angles ϕ_r and θ_r in Figure. 2 are the local inflow angle and the local pitch angle, restively. The angle ϕ_r is determined by the ratio of local axial velocity to the local tangential velocity and given by

$$\tan(\phi_r) = \frac{(1-a)U_\infty}{(1+a')\omega.r}. \tag{4}$$

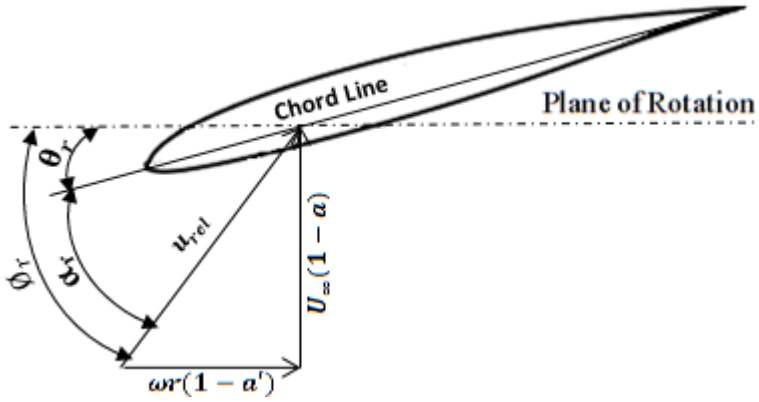

Figure 2. Local velocity diagram at the rotor plane

$C_L(\alpha_r, Re_r)$ and $C_D(\alpha_r, Re_r)$ are conventionally obtainable by interpolating through a look-up two-dimensional $(2D)$ data table, thus, the elemental lift (L) and drag

(D) forces can be computed as shown in Figure. 3. The normal and tangential forces acting on an element (dF_{n_r} and F_{t_r}, respectively) and their equivalent force coefficients (C_{n_r} and C_{t_r}) are calculated as

$$C_{n_r} = \frac{L\cos\phi_r + D\sin\phi_r}{\frac{1}{2}\rho u_{r\_rel}^2 c_r} = \frac{dF_{n_r}}{\frac{1}{2}\rho u_{r\_rel}^2 c_r} \tag{5}$$

$$C_{t_r} = \frac{L\sin\phi_r - D\cos\phi_r}{\frac{1}{2}\rho u_{r\_rel}^2 c_r} = \frac{dF_{t_r}}{\frac{1}{2}\rho u_{r\_rel}^2 c_r}. \tag{6}$$

For a rotor with B blades, according to the blade element theory [6], the differential thrust (dT_r) and torque (dM_r) on a blade element are given by

$$dT_r = \sigma_r \pi r \rho \frac{U_\infty^2 (1-a)^2}{\sin^2\phi_r} C_{n_r} dr \tag{7}$$

$$dM_r = \sigma_r \pi r^3 \rho \frac{U_\infty \omega (1-a)(1+a')}{\sin\phi_r \cos\phi_r} C_{t_r} dr \tag{8}$$

where σ_r is the local solidity at a radial distance r and defined as.

$$\sigma_r = \frac{Bc_r}{2\pi r}. \tag{9}$$

Equating the differential thrust in (Eq. 1) and (Eq. 7) allows calculation of the axial induction factor (Eq. 10). Similarly, equating the differential torque in (Eq. 2) and (Eq. 8), an expression for the tangential induction factor is obtained (Eq. 11)

$$a = \frac{1}{\frac{4\sin^2\phi_r}{\sigma_r C_{n_r}} + 1} \tag{10}$$

$$a' = \frac{1}{\frac{4\sin\phi_r \cos\phi_r}{\sigma_r C_{t_r}} - 1}. \tag{11}$$

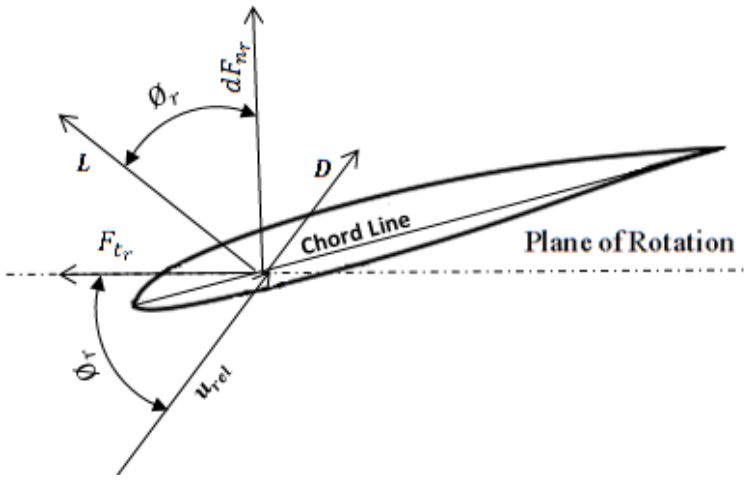

Figure 3. Local forces on a blade element

2.2. BEM THEORY CORRECTIONS

The classical BEM theory lacks the precision due to the inherent assumptions for simplifications. To generate satisfactory results when validating against a water tunnel test, three correction models were integrated to account for the tip and hub losses, correct the thrust coefficient, and account for the blockage effects.

2.2.1. Tip and Hub Losses. BEM theory assumes that the normal and tangential forces exerted by the blades on the flow are evenly distributed upon annular elements. For a turbine with a limited number of blades (e.g., 3 to 6 blades), the fluid tends to stream around the tip and root form the pressure side to the suction side, which generates vortices at the trailing edge [6]. These vortices cause a lift force reduction, and it is most pronounced at the tip, which has the highest influence on the turbine torque. A method was developed by Prandtl to define tip loss factor (F_{tip}) and then was introduced into BEM theory by Glauert [20] is given by

$$F_{tip_r} = \frac{2}{\pi} cos^{-1}\left[exp\left\{-\left(\frac{B}{2}\frac{R_{rotor}-r}{r\,sin\phi_r}\right)\right\}\right]. \quad (12)$$

where R_{rotor} is the radius of the rotor. Similar to the tip loss factor, a hub loss factor (F_{hub}) was developed by Moriarty and Hansen [21] is defined as

$$F_{hub_r} = \frac{2}{\pi} cos^{-1}\left[exp\left\{-\left(\frac{B}{2}\frac{r-R_{hub}}{r\,sin\phi_r}\right)\right\}\right]. \quad (13)$$

Tip and hub losses collectively affect the hydrodynamics of a blade element, therefore, a total loss factor ($F_r = F_{tip_r}\,F_{hub_r}$) must be added into the momentum Eqs. 1 and 2 (see [21]), consequently, the induction factors are updated to

$$a = \frac{1}{\frac{4F_r\,sin^2\phi_r}{\sigma_r C_{nr}} + 1} \quad (14)$$

$$a' = \frac{1}{\frac{4F_r\,sin\phi_r\,cos\,\phi_r}{\sigma_r C_{tr}} - 1} \quad (15)$$

2.2.2. High Axial Induction Factor. According to the momentum theory, the thrust coefficient (C_T) starts to decrease as a increases above 0.5. However, based on measured data, C_T, in fact, increases and could reach up to 2 (for 2D flat plate) as a reaches unity [7, 12]. Buhl [4] developed a mathematical relation based on Glauert empirical relation [3] and F_r. The new relation overcame the discontinuity in the curve of sectional thrust coefficient (C_{T_r}) verses a that appears when using Glauert relations for $F_r < 1$. The new generalized relation by Buhl [12] for C_{T_r} has a transition from the momentum theory to the empirical relation occurs at $a_{critical} = 0.4$ is given by

$$C_{T_r} = \frac{4C_{Ta}}{9} + \left(4F_r - \frac{20C_{Ta}}{9}\right)a + \left(\frac{25C_{Ta}}{9} - 4F_r\right)a^2 \quad (16)$$

where C_{Ta} is the desired C_{T_r} when $a = 1$ and could be determined experimentally and was suggested that a value of about 1.6-1.8 is appropriate [12]. Solving Eq. 16 for a, a new axial induction factor in Eq. 14, when $C_{T_r} \geq 0.96$, can be updated as

$$a = \frac{18F_r - 10C_{Ta} - 3\sqrt{12F_r\left(3F_r - 3C_{T_r} - 2C_{Ta}\right) + 25C_{T_r}C_{Ta}}}{36F_r - 25C_{Ta}} \tag{17}$$

2.3. BLOCKAGE MODEL

The flow characteristics around, though, and downstream of a rotor operating in a confined flow (e.g., wind/water tunnel, manmade/natural channel, or wind farm) are different from a rotor operating solely in an open environment. The flow speed around and through the rotor in confined flow is augmented [22, 23] and the wake expansion is driven by the surrounding effects, such as lateral walls, bed, free surface (for water turbine) or turbulent generated by neighboring turbines [24, 25]. Consequently, the hydrodynamic loads act on confined rotor blades are larger and the power harnessed is higher [19, 23, 25].

The widely used technique is representing a rotor in a confined flow by an actuator disk and applying the principles of continuity and equilibrium of momentum to the streamtube volume that passes through and around the disk. Blockage correction models based on an actuator disk concept have been addressed in various studies (see for example [19, 23, 24, 26, 27]). Most of these models require the measurement of the thrust acts on the rotor. Due to the current work experimental limitation, the model presented by Whelan et al. [19], where no thrust measurement is needed, was integrated into the BEM model.

3. HYDRODYNAMIC CHARACTERISTICS

In the current work, the manufactured and tested rotor blades have Eppler 395 foil with a constant chord and pitch angle (untwisted and untapered). The 395 hydrofoil was selected because of its high ratio of C_L/C_D [10, 28]. Lift and drag coefficients for the Eppler 395 hydrofoil were calculated at a range of sectional Reynolds number, based on sectional relative velocity, using the $2D$ panel code, XFoil [29, 30]. The XFoil model is a panel technique integrates coupled viscous-inviscid interaction method. XFoil-Matlab interface [31] was modified to accelerate calculating the lift and drag over the range of operational Re_r.

3.1. ROTATION AND 3D EFFECTS

The lift and drag behavior of a rotating blade differs from that of a $2D$ aero/hydrofoil flow such as that calculated by XFoil. The rotation causes the dynamic pressure to increase toward the blade tip, which results in increasing the relative velocity with the radial distance [32]. Moreover, centrifugal and Coriolis forces start to appear and accelerate the flow in the span-wise and chord-wise directions, respectively [32, 33]. The combination of these rotational effects delays the stall angle of attack, which increases the lift [32]. To account for the stall delay caused by the rotational effects, the model suggested by Du and Selig [34] was implemented to correct the lift and the model developed by Eggers et al. [35] was coded to correct the drag. The optimum representative linear segment from the C_L versus α relation was obtained by scanning for the maximum coefficient of determination (R^2) which is a measure of how well the regression line fits the data (see Eq.

18). The linear segment slope and intersection were required by the three-dimensional ($3D$) lift coefficient (C_{L3D}) calculation. Figure. 4 shows the Eppler 395 $2D$ lift (C_{L2D}) and drag (C_{D2D}) coefficients and the $3D$ effects at two different randomly selected sectional Reynolds numbers.

$$R^2 = 1 - \frac{\text{Sum of squared error between the actual and predicted } C_{L2D} \text{ values}}{\text{Sum of squared error between the actual values of } C_{L2D} \text{ and their mean}} \quad (18)$$

3.2. COEFFICIENTS EXTRAPOLATION

The data generated by the XFoil ranged between -10^o to 25^o angles of attack, if no convergence failure had been encountered. Therefore, Viterna model [36] was employed to extrapolate the hydrofoil hydrodynamic data over a wider range of angles of attack ($\pm 180^o$).

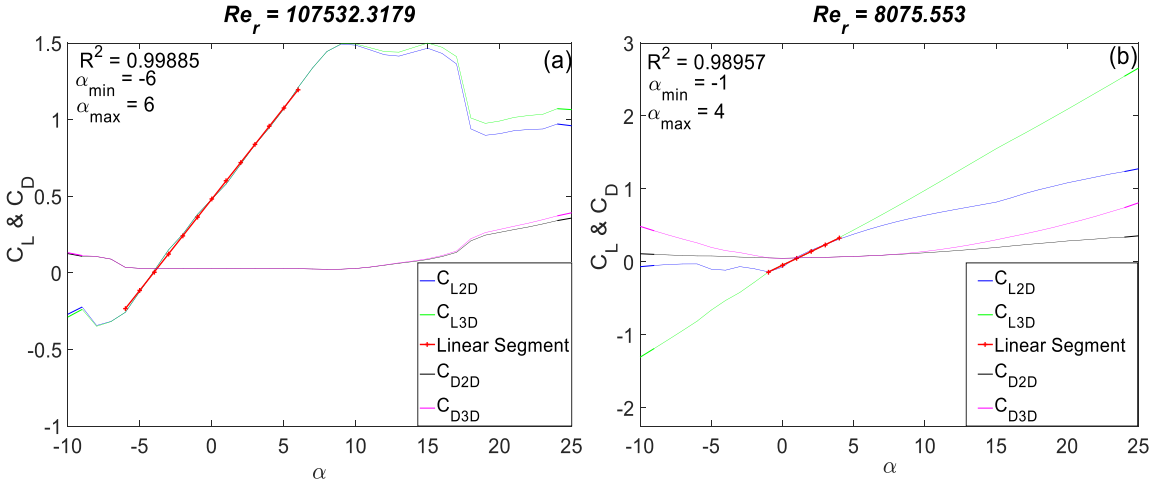

Figure 4. C_{L2D}, C_{L3D}, C_{D2D}, and C_{D3D} vs. α at two different operational conditions: (a) ω=200 *RPM*, $U\infty$=0.727 m/s, and r/R_{rotor}=0.0906 and (b) ω=400 *RPM*, $U\infty$=0.594 m/s, and r/R_{rotor}=0.893

3.3. LIFT AND DRAG VALIDATION

A reliable prediction of the BEM models mainly depends on the accuracy of the measured or simulated aero/hydrodynamic properties of a blade's foils. Applying the correct lift and drag coefficients at an operational Re will decrease the uncertainty of the BEM model performance and allow for accurate loading and power prediction. Therefore, it was essential to inspect the accuracy of the generated XFOIL results.

Gharali and Johnson [37] validated different CFD models results against experimental data. For the range of Re (10^4-10^6) and steady airfoil, they concluded that the shear-stress transport (SST) k–ω turbulent model, developed by Menter [38], yielded the highest agreement with the experimental results compared to the other tested models. The model was able to predict the lift variation in the region before the stall. SST k–ω is sensitive to the adverse pressure gradient, which occurs at the upper surface of the air/hydrofoil and affects the separation mechanism.

The current study assumes steady and incompressible flow. The numerical CFD simulation was conducted by solving for a conservation of mass and momentum using an unstructured grid finite volume methodology in the commercial CFD software of ANSYS 15.0/Fluent. The geometry was built in Workbench/Design Modeler and meshed in Workbench /ICEM. The hydrofoil was meshed using a C grid layout with different mesh resolutions and varied initial wall grid point spacing (y'). To investigate the effect of mesh grid resolution on the results, the lift coefficient was calculated each time the mesh size was changed. The mesh size was varied by changing the number of elements in the stream direction and normal to the stream direction with a ratio of approximately 1.7. The independence between the aero/hydrodynamic forces and the grid size was approved at

mesh size of around 151,000 elements and absolute relative approximate error less than 1% (see Figure. 5a). A number of 285 grids were assigned along the hydrofoil. The first grid spacing, y', was set such that the highest value of y^+ is less than 0.8. Figure. 5b shows a flow domain and a close view of a meshed Eppler 395 with a very dense grid close to the wall ($y^+ < 0.8$).

The solver was set to Absolute Velocity Formulation, Steady, 2D Planar, and Pressure-Based (for incompressible flow). The front and lateral sides of the flow domain were set to a velocity inlet (marked blue in Figure. 5b) with a turbulent intensity (I) of 3.56% and length scale (l) of 0.00117. These input turbulent parameters were calculated from empirical relationships based on the operational conditions: $I = 1.6(Re)^{-1/8}$ and $l = 0.07$ c where c is the chord length. The inlet velocity components were specified based on the angle of attack. The rear side was set to a pressure outlet (marked red in Figure. 5b) with zero gauge pressure and turbulent viscosity of 10. The hydrofoil was considered as a stationary wall with no slip boundary conditions. A second order upwinding discretization schemes were selected for solving all the flow equations. The Coupled algorithm was selected for solving pressure and velocity in a coupled manner. Convergence criteria have been set such that the residuals for the continuity, x-momentum, y-momentum, z-momentum, k, and ω were less than 10^{-5}.

Due to the lack of experimental measurements of the C_L and C_D for Eppler 395, the experimental results for NACA 63-215, NACA 64-415 [39], NACA 63-415 [40], and S809 [41] airfoils were used to validate the CFD and XFoil models. Beforehand, the performance of various turbulence models was inspected using the experimental results for NACA 63-415. The selected models were Spalart-Allmaras, Standard k–ε, SST k–ω, and

RNG k–ε. All these models were run at the same experimental operational conditions of NACA 63-415 (Re of $1.6 * 10^6$ and an angle of attack of 5˚ and 10˚). SST k–ω model prediction had better agreement with the experimental results compared to the other turbulence models. Hence, SST k–ω was used to model the other airfoils with experimental results from the literature.

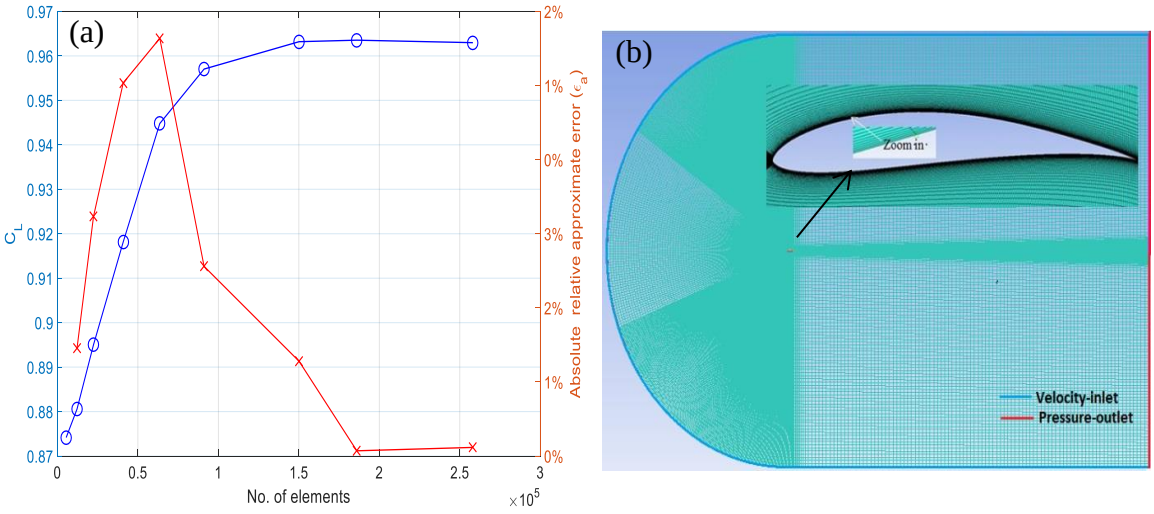

Figure 5. (a) Mesh independence study and (b) mesh around the foil with a closer view of the refined grid and colored boundary conditions

The C_L and C_D against the angle of attack for the airfoils with experimental data are presented in Figures. 6a, b, c, and d, and for Eppler 395 are presented in Figure. 7. For all airfoils, both SST k–ω and XFoil models satisfactorily predicted C_L up to angles of attack close to the stall region. However, at angles of attack beyond the stall, SST k–ω model slightly overestimated C_L, for NACA 63-415 and S809 and slightly underestimated C_L for NACA 63-215 and 64-415. XFoil prediction of the C_L in the stall region was higher than the experimental results due to the inaccurate prediction of the transition location. The

drag coefficient was slightly overestimated by SST k–ω for all airfoils except NACA 63-415 in which the predicted C_L started to deviate near the stall angle of attack. XFoil model performance was more accurate in predicting the C_D compared to SST k–ω. It should be noted that references [39] and [41] provide limited range of experimental data of C_D. Therefore, C_D was not plotted to cover the full range of angles of attack in Figures. 6b, c, and d. In general, the performance of the SST k–ω model simulating these airfoils was found satisfactory. Therefore, SST k–ω was employed as a validation tool for Eppler 395 XFoil results.

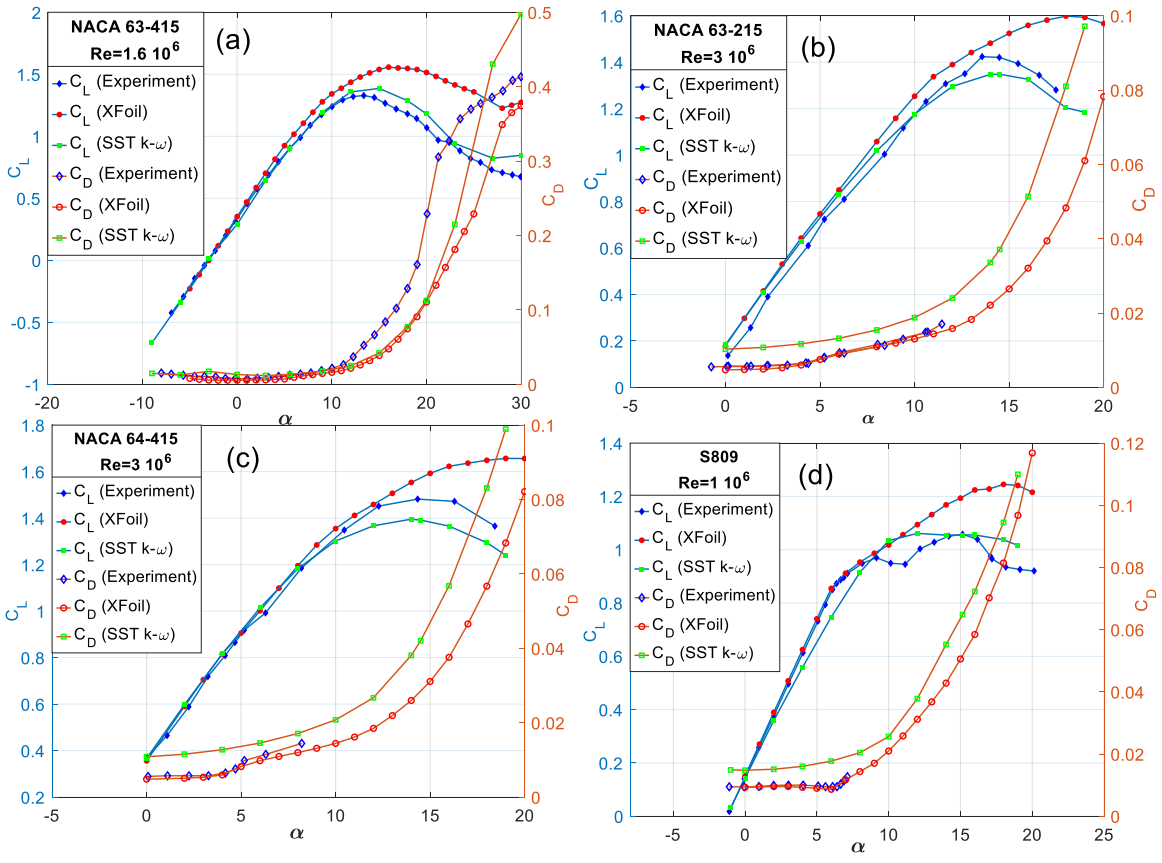

Figure 6. C_L and C_D curves for the NACA and S809 airfoils

In Figure. 7, the general trend of C_L curves generated by XFoil and SST k–ω is similar to the respective curves in Fig 6. The lift curve generated by XFoil gradually deviated from the lift curve generated by SST k–ω as the angle of attack increased. This behavior was likely due to the moderately low Re, which critically affected the XFoil prediction accuracy of the transition location on the hydrofoil suction side [19]. Similar behavior to the C_D calculate by XFoil and SST k–ω in NACA 63-415 was observed in Eppler 395. No correction was made for the lift and drag beyond the stall angle of attack because the tested rotor stopped before the stall region as a result of stall delay. This means a large portion of the blade span still operates at angles less than the stall angle of attack (detailed explanation of this behavior can be found in [42, 43]).

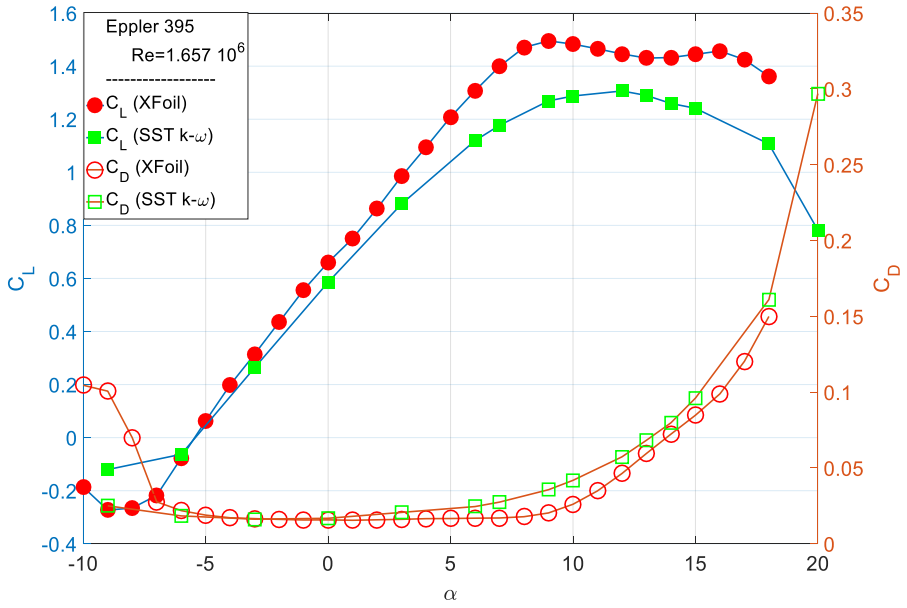

Figure 7. C_L and C_D curves for Eppler 395 at Re=1.657*10^5

4. NEURAL NETWORK DESIGN

The principle of a neural network is such that, it comprises of an input layer that consists of input neurons. Each input neuron is multiplied by a specific weight, shown in Figure. 8 as W_{ki}. The weighted input neurons are then summed in hidden neurons and computed by an activation (transfer) functions. Different hidden neurons will have different combination of weighted input W_{ki}. A second hidden layer combines the computed outputs from the preceding layer and transfers the information to the next hidden layer neurons using other weights (W_{ij} in Figure. 8) and activation functions. The same process continues until the computed hidden layers outputs are passed to the output layer neurons.

Neural networks have been used to control and design complex systems and analyze structures because of their ability to carry out complex mapping based on sets of inputs and their corresponding outputs, regardless of knowing the details of the mathematical model of these systems [44-48]. A simple NN with one hidden layer and arbitrary activation functions has the ability to approximate any complex function [49]. There is a large number of different types and architectures of NN, varying fundamentally in the way they learn, where the learning function is used to update the weights between the neurons based on the neural based algorithm.

For the present study, a feed-forward MLP-NN with back-propagation training method was used. Different NN architectures were structured and their performance was evaluated. Figure. 8 illustrates sample NNs that were trained to obtain C_L and C_D (Figure.

8a), and a and a' (Figure. 8b). All hidden layers had sigmoid transfer functions, $f(x) = 1/(1+e^{-x})$, whereas the output layer had a linear transfer function, $f(x) = x$.

For building different MLP-NN models, MATLAB scripts were developed with the aid of Neural Network built-in functions. The different MLP-NN models were structured by varying the number of neurons, the number of hidden layers and the training method as shown in Table 1. The models' performance error was monitored using the performance functions in MATLAB (e.g., the mean square error (MSE) and the R value). Based on the performance, the architecture of the neural network was selected.

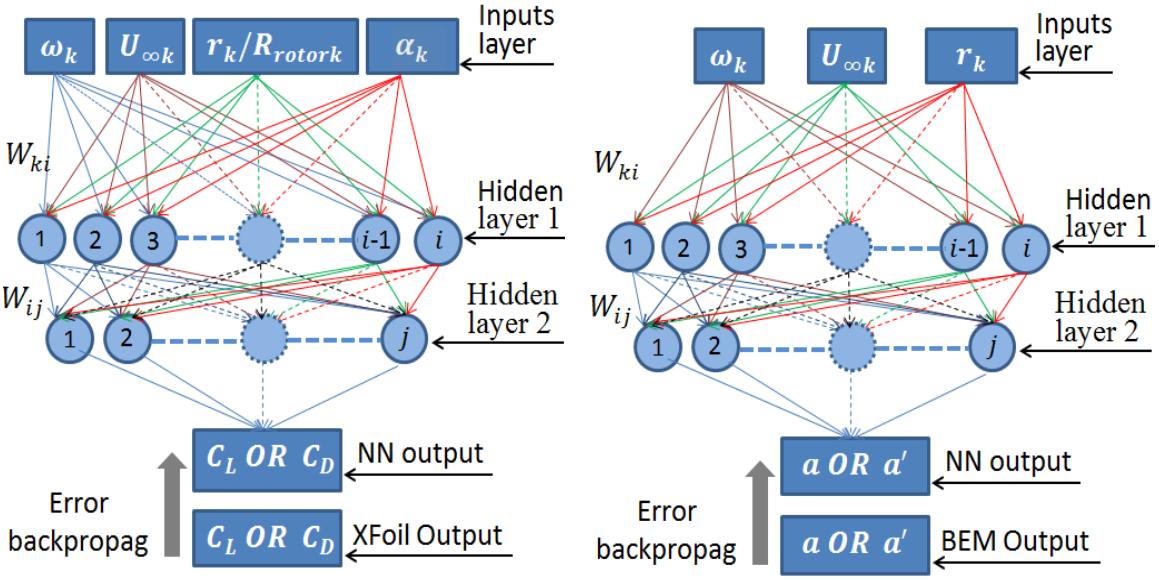

Figure 8. Architecture of feed-forward back-propagation MLP-NNs for (a) C_L and C_D prediction and (b) a and a' prediction

5. INTEGRATION OF BEM-NNS MODELS

The purpose of the models' integration was two-fold: (a) to calculate the lift and drag coefficients during the BEM iteration and (b) to predict the axial and tangential induction factors that had a convergence problem.

Firstly, the two MLP-NNs concerning the lift and drag coefficients were trained beforehand and then loaded to the BEM algorithm. This was to calculate C_L and C_D through $2D$ interpolation from a $3D$ surface: C_L or C_D against range of angles of attack ($\pm 180^o$) and a range of operational Re_r ($7.5 * 10^3 \leq Re_r \leq 1.657 * 10^5$). The sectional Reynolds number was not explicitly considered as an input to these NNs, but the variables ω, U_∞ and r/R_{rotor}, which used in Re_r calculation, were considered instead. The reason was to separate the sensitivity of these NNs toward the changes in these input variables. When BEM model searches for a solution, the trained NNs were called iteratively to simulate the updated variables ($\omega, U_\infty, r/R_{rotor}$ and α_r) and to interpolate for the new sectional C_L and C_D. The process continued until the convergence criteria of local induction factors were met. In case the blade is twisted and tapered, the varied pitch angle and chord length should be also considered in the BEM and NN input variables.

The other two MLP-NNs used to predict a and a' that failed to converge, were trained during the BEM model calculation: after BEM finishes calculating the induction factors overall the operational space and before BEM integrates for sectional forces overall the blade span. The process is such that, the converged induction factors (a and a') and their corresponding operational characteristics (ω, U_∞ and r) were assigned to two matrices. Then, these matrices were used to train the MLP-NNs, where ω, U_∞ and r are the

inputs and a and a' are the targets. The constrained induction factors at the blade tip and root were excluded from the trained data to improve the NNs performance. The trained NNs, then, were used to calculate the induction factors with convergence problems based on their corresponding operational characteristics (ω, U_∞ and r). Finally, the BEM model resumed the calculation as in the ordinary way. The flow chart diagram presented in Figure. 9 describes the combined algorithms process.

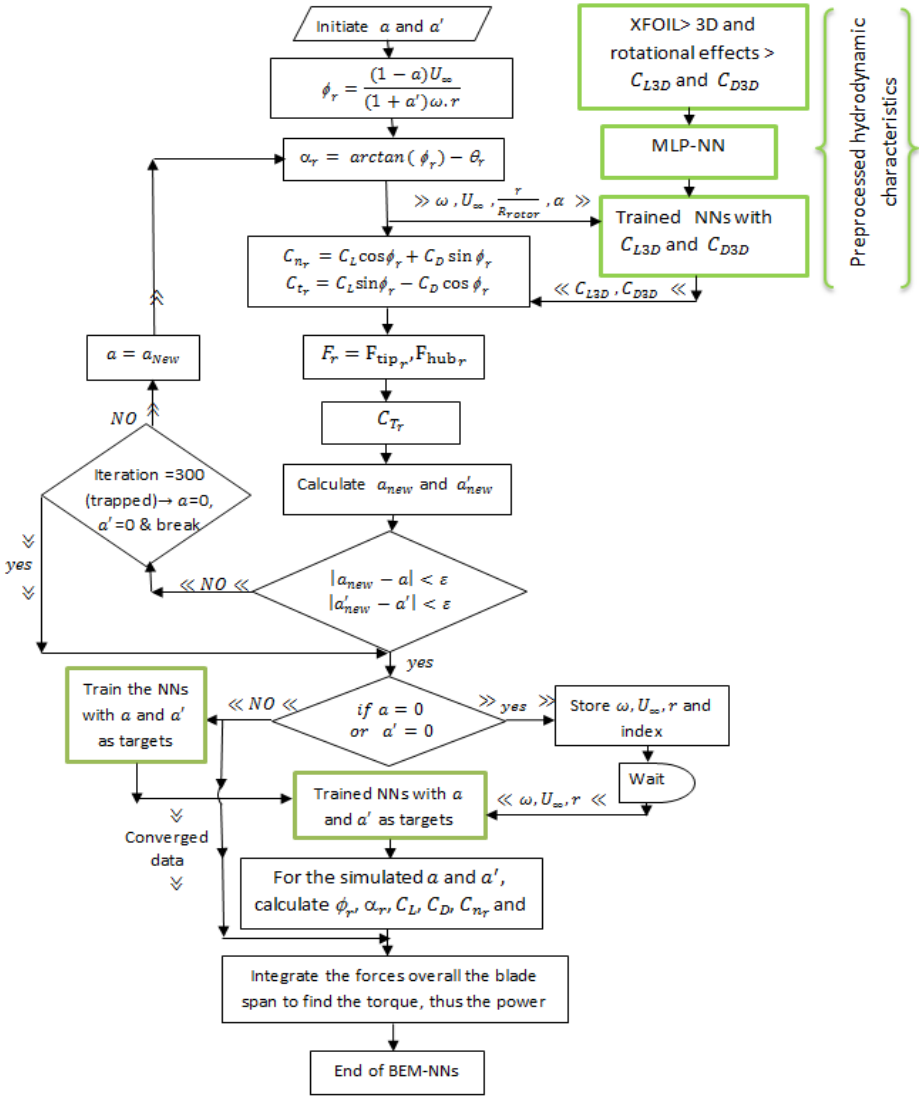

Figure 9. Flowchart of the integrated algorithm BEM-NNs

6. EXPERIMENTAL METHODOLOGY

Hydrokinetic turbine power experiments were conducted to validate the proposed model in this study. A description of the experimental work is given in this section. Detailed information of the experimental setup and experimental procedure can be found in a previous work by the authors [42].

6.1. WATER TUNNEL FACILITY

A water tunnel facility at Missouri University of Science and Technology was used to perform the hydrokinetic turbine power test. The water tunnel test section had width, depth, and length of 0.381 m x 0.508 m x 1.524 m (15 in. x 20 in. x 60 in.) respectively, and a maximum water velocity of 1 m/s. A speed controller was used to vary a water pump frequency, and thus to control the flow speed in the test section. Figures. 10a and b are images of the water tunnel facility and tested turbine system, respectively.

(a) (b)

Figure 10. (a) Water tunnel facility and (b) operating turbine system

6.2. EXPERIMENTAL SETUP

The mechanical power generated by the turbine was transmitted to torque and rotational speed sensors through two coupled horizontal transmission shafts and one vertical transmission shaft. A bevel gear was used to connect the vertical and horizontal transmission shafts. A three-blade horizontal axis hydrokinetic turbine was used in this study. The blades were manufactured from composite materials (carbon/epoxy prepreg) using out-of-autoclave (OOA) technique [42]. The manufactured blade had Eppler 395 hydrofoil. The blades were untwisted and had a fixed chord length of 16.76 mm (0.66 in.). The blade span was cut to 96.32 mm (3.79 in.) to reduce the high blockage effects (blockage ratio was approximately 20%). The manufactured blade is shown in Figure. 11a.

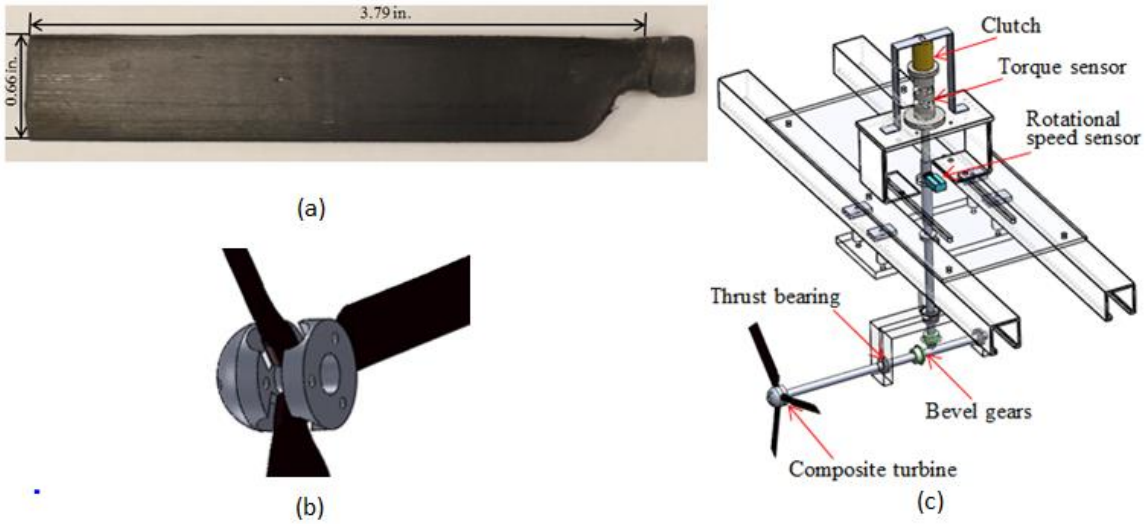

Figure 11. (a) Manufactured blade with Eppler 395 hydrofoil, (b) two-part hub assembly and (c) schematic of hydrokinetic turbine-generator system

A hub with diameter and length of 25.4 mm (1 in.) was used. The hub was designed to have two parts to clamp the blades' roots (as illustrated in Figure. 11b) so that the blade's

pitch angle was adjustable. The power was calculated by measuring the torque and rotational speed by means of a FUTEK reaction sensor with maximum torque of 0.353 N.m and a time-average Hall Effect sensor, respectively.

6.3. EXPERIMENTAL PROCEDURE

The power coefficient (C_P) versus tip speed ratio (TSR) curve was produced by varying the applied load on the turbine system shaft using a controllable magnetic particle clutch with maximum torque of 0.226 N.m. A power supply with controllable voltage and current was connected to the clutch to alter the turbine torque and the rotational speed.

The integrated torque sensor was calibrated out of the water tunnel using a set of similar weights (8.45 gm) and a wheel. The wheel was attached to the torque sensor assembly horizontal shaft. In order to simulate the torques acting on the rotor, the weights were added gradually to a light bag that was attached to the wheel via a thread. The sensor reading in millivolt per volt was averaged and collected for every weight increment by using a data acquisition and LabVIEW code. The integrated torque sensor calibration was done to account for the turbine system friction torque and to obtain a relationship between the sensor output signals and the applied torque. An electrical engine (with a speed controller) was used to calibrate the time-average rotational speed sensor at various rotational speeds. The reason of using the time-average sensor instead of traditional tachometer was to manage the data acquisition time (the time was similar to the time of collecting torque data) and also to account for the fluctuations in the rotational speed reading of the rotor. The pitch angle was measured for the hydrofoil chord, with respect to the plane of rotation, by a digital angle gauge.

The turbine system assembly was placed upon the water tunnel shoulders (the rotor was centered the width of the test section facing, perpendicularly, the incoming flow). The water was maintained at the same level of 0.4826 m (19 in.) to avoid the effect of changing the free surface proximity on the power output [50]. Figure. 11c shows the hydrokinetic turbine-generator assembly.

7. RESULTS AND DISCUSSION

7.1. NN PERFORMANCE

The C_L and C_D NNs structure and training method were varied for performance investigation as listed in Table 1. Each configuration was used to train around 60,000 $3D$ corrected extrapolated data form XFoil. The input parameters to these NNs were ω, U_∞, r/R_{rotor} and α_r. The input parameters were selected based on their effect on C_L and C_D.

Table 1. Design parameters of the NNs used to calculate C_L and C_D

	Number of Hidden Layers	Number of Neurons per Hidden Layer	Training Type
Number of Neurons Effect	1	[5],[10],[20], [30],[40],[70]	Levenberg-Marquardt
Number of Hidden Layers Effect	1	[20],[30]	Levenberg-Marquardt
	2	[20-10],[30-15]	
	3	[20-10-5],[30-15-5]	
Training Methods Effect	2	[20-10]	Levenberg-Marquardt Bayesian Regularization BFGS Quasi-Newton Resilient Backpropagation

7.1.1. Effect of the Number of Hidden Neurons. To examine the effect of the number of hidden neurons (N), the other design parameters were kept constant: one hidden layer (1H) was considered and a Levenberg-Marquardt (LM) training method was selected. The number of hidden neurons was varied to 5, 10, 20, 30, 40 and 70 N. Each design was run three times. The correlation coefficient (R) was used to evaluate the NN performance. The correlation coefficient is an indicator of the degree of the relationship between the original and the predicted data. An R value of 1 would represent a perfect fit linear regression between the targets (XFoil outputs) and the NN outputs. The highest correlation coefficient from each design is listed in Table 2 and the best NNs performance was underlined. The correlation coefficient for the NN calculating C_L was observed to slightly increase with increasing the number of neurons. However, for the NN calculating C_D, 40N provided the highest correlation coefficient which was likely due to that NN was overfitted at 70N. Moreover, the rate of change in NN performance was noticed to be very small when number of neuron increased to 70N (0.06% and -0.03% for C_L and C_D, respectively) so no further investigation was sought.

Table 2. Effect of the number of hidden neurons

Number of Neurons per Hidden Layer	Correlation Coefficient (R)	
	C_L	C_D
[5N] (1 Hidden Layer)	0.96965	0.98546
[10] (1 Hidden Layer)	0.98881	0.99351
[20] (1 Hidden Layer)	0.99401	0.99552
[30] (1 Hidden Layer)	0.99506	0.99607
[40] (1 Hidden Layer)	0.99617	<u>0.99751</u>
[70] (1 Hidden Layer)	<u>0.99674</u>	0.99722

7.1.2. Effect of the Number of Hidden Layers. In this part, Levenberg–Marquardt was selected as the training method. The number of neurons was specified as listed in Table 1. The change in NNs performance with an altered number of hidden layers is listed in Table 3. The NN with 3H and the higher number of neurons, [30-15-5], had the highest correlation factor. It was observed that the 2H NN with [30-15] N had higher performance than the 3H NN with [20-10-5]. No further increase in hidden layers was sought due to the small rate of improvement and the satisfactory R value reached.

Table 3. Effect of the number of hidden layers

Number of Neurons per Hidden Layer	Correlation Coefficient (R)	
	C_L	C_D
[20] (1 Hidden Layer)	0.99401	0.99552
[30] (1 Hidden Layer)	0.99506	0.99607
[20-10] (2 Hidden Layers)	0.99837	0.99841
[30-15] (2 Hidden Layers)	0.99869	0.99894
[20-10-5] (3 Hidden Layers)	0.99845	0.99876
[30-15-5] (3 Hidden Layers)	0.99898	0.99913

7.1.3. Effect of the Training Method. To investigate for an optimum training method for modeling the C_L and C_D, the NN structure was maintained to have 2H (20N-10N). The selected training methods and their performance are demonstrated in Table 4. From the listed R values, it is obvious that the Resilient Backpropagation had the lowest

performance over most of the tested angles of attack for lift calculation; however, the method was the fastest. Since learning rate is a design parameter for the Resilient Backpropagation training algorithm, it was varied to be 0.4, 0.1 and 0.001. Nevertheless, the Resilient Backpropagation performance for the C_L calculation showed no better performance than the other methods and results were not included. Levenberg-Marquardt demonstrated slightly higher R compared to the other models. More investigation of each training method design parameters could improve their performance even further.

Table 4. Training method effect

Training Model	Correlation Coefficient (R)	
	C_L	C_D
Levenberg-Marquardt	0.99401	0.99552
Bayesian Regularization	0.99367	0.99418
BFGS Quasi-Newton	0.99005	0.99097
Resilient Backpropagation	0.98031	0.995

7.2. NN VALIDATION

XFoil was run at extra new Reynolds numbers and the results were used to validate the trained NNs performance. The validation was achieved after the trained NNs simulated the new unseen operational inputs (the new validation Reynolds numbers). The lift and drag coefficients calculated from NNs and XFoil were plotted together (Figures. 12 and

13) for the illustration of the curves behavior and results' comparison. The NNs showed satisfactory results overall the range of angles of attack. Nevertheless, as shown in Figure. 13b, at a high rotational speed above 350 revolutions per minute (*RPM*) and relatively high flow velocity ($U_\infty \geq 0.75$ m/s), C_D curves generated by the NN tended to slightly deviate from the XFoil results at the vicinity of extreme angles of attack ($\pm 180^o$). A similar behavior of deviation was noticed when plotting a response surface of the C_D generated by the NN. Although these regions with a poor performance could be met during the models iteration, but it is most likely not within the practical solution range of α [17].

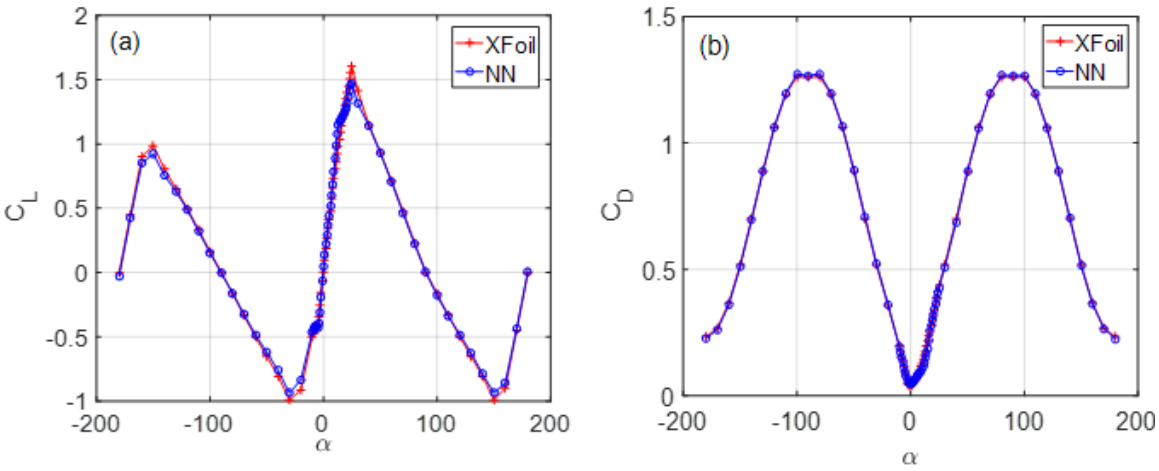

Figure 12. (a) C_L and (b) C_D generated by XFoil and NN at ω=250 *RPM*, U_∞= 0.75 m/s, and r/R_{rotor}= 0.5

7.3. BEM-NNS PERFORMANCE AND VALIDATION

The BEM-NNs were structured to fulfill two cases: case 1) BEM-NNs had no integration of NN as a multivariate interpolation tool or the blockage model and case 2) BEM-NNs had complete integration of NN as a multivariate interpolation tool and the blockage model.

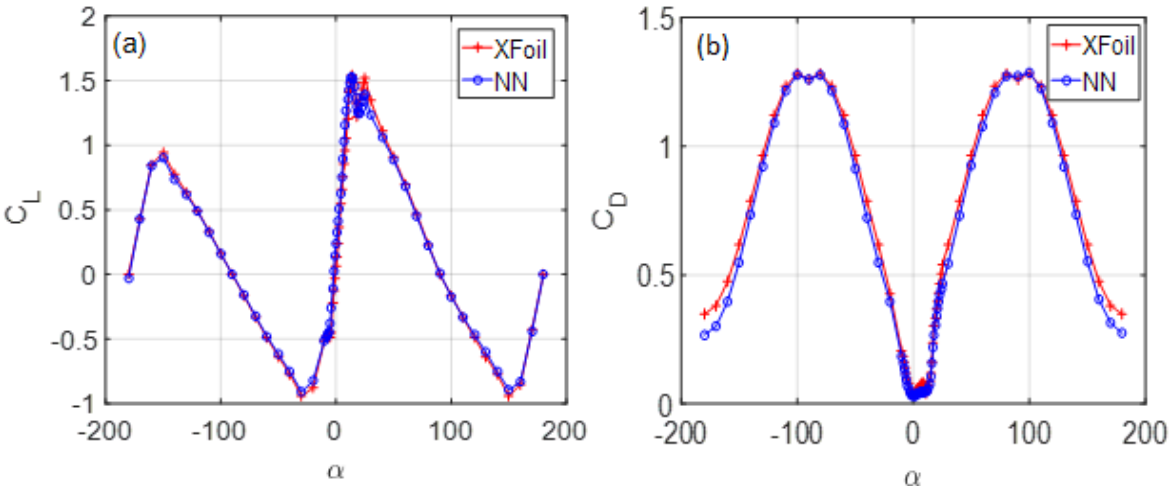

Figure 13. (a) C_L and (b) C_D generated by XFoil and NN at ω=425 *RPM*, U_∞= 0.75 m/s, and r/R_{rotor}= 0.5

Case 1 was considered for evaluating the validity of the NNs of handling the induction factors convergence issue through the comparison with other models. The case was for a three-blade turbine pitched to 15^o and operated at a water velocity of 0.8161 m/s. The selection of these operational characteristics was based on the existence of the convergence failure in the conventional BEM theory.

Figure. 14 shows a comparison between the BEM-NNs results, the conventional BEM theory (as the algorithm presented in [21]), and the BEM model developed by Ning [16, 17]. The suggested model was valid to run at higher *TSR* with no issues compared to other models. Another advantage was that the suggested model was easily and successfully integrated with the blockage model in [19] (see case 2). The Ning model was faster by around 80% $\left(\frac{15.76\ sec}{19.62\ sec} * 100\%\right)$ than the BEM-NNs model when both models run at the same operational conditions. The BEM-NNs mode execution speed depended on the number of the failed to converge data. The Ning, model, however, would require fundamental derivation if a blockage model such as in [19] would be integrated.

The conventional BEM model loop was interrupted when the iteration was trapped during searching for a sectional solution of the induction factors. The interrupted iterations were assigned the previous neighboring converged induction factors so that the loop could continue to search for the next sectional solution. The discontinuity in the conventional BEM curve was caused by the fact that, during the iteration at specific *TSR*s and at sections close to the tip, the local incoming flow angle (ϕ_r) approached zero. As a result, the exponents in the loss factors equations (Eqs. 9 and 10) had large positive values. Consequently, $F_{\mathrm{hub_r}}$ tended to negative infinity so the later iteration failed to converge and all the data at that *TSR* was not plotted for all the radial sections. If the absolute value of $\sin\phi_r$ (Eqs. 9 and 10) was considered to maintain the exponent to have a negative sign, as in [16] model, the power curve would deviate from the correct solution. The source of these behaviors was not tracked back because it was out of the scope of this work.

Case 2 used the NNs to overcome the convergence issue as well as to properly calculate the sectional C_L and C_D at different sectional Reynolds numbers and angles of attack during the iteration process. The model in case 2 had also integrated the blockage model developed in [19] to allow for validation against the experimental results of the rotor operates in a confined flow (the water tunnel) with a blockage ratio of approximately 20%.

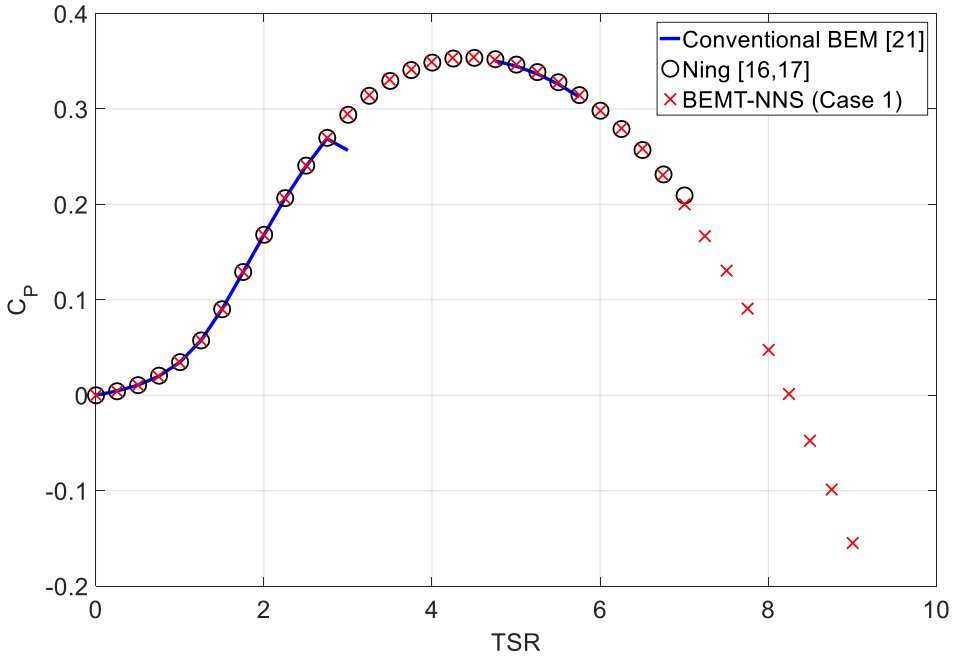

Figure 14. BEM models comparison

The power coefficient verses *TSR* curves at a flow speed of 0.8161 m/s and pitch angle of 20^o, produced from the current work experiments (the three-blade rotor operates in a water tunnel), BEM-NNs with integrated blockage model [19], and the classical BEM with integrated blockage model [19] are illustrated in Figure. 15. The classical BEM blockage model utilized a representative Re and had no integration of NNs. A representative Re is a fixed value of Reynolds number which is used in all BEM calculation, at a specific flow condition, regardless of the radial location of the blade element. The representative Re was calculated at approximately 57% and 78% of the blade span (see Table 5). The 78% was selected because it was the closest element to the 75% which was the ratio used in [19]. The BEM-NNs blockage model results showed a reasonable agreement with the present experimental results. Nevertheless, the BEM-NNs slightly overestimate C_P 0.11124 at *TSR*s close to the curve peak ($2.75 \leq TSR \leq 3.5$).

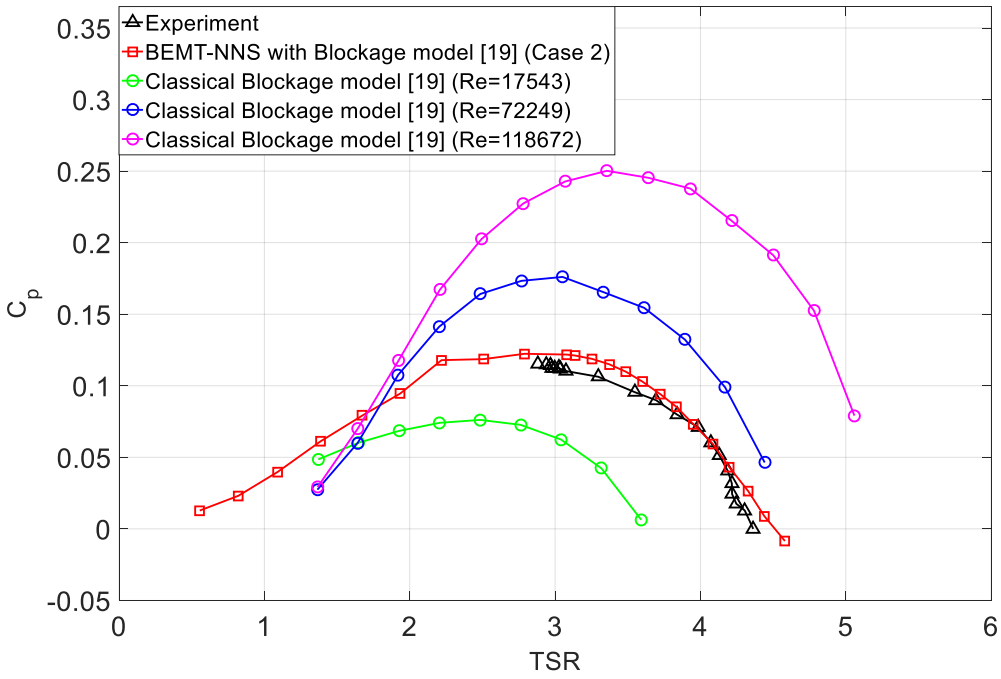

Figure 15. BEMT-NNs blockage model validation at flow speed of 0.8161 m/s for a three-blade turbine

The overprediction was attributed to the fact that XFoil calculated lift gradually deviated from the experimental results toward the stall angle of attack (see Figures. 6 and 7). At high *TSR* beyond 4.2, the predicted results started to deviate again from the experiment due to the rotor entered a turbulent wake status and a model such that developed by Buhl in section 2.2.2 for unconfined flow is required by the blockage model. In fact, ref. [19] had incorporated a correction model at high *TSR* based on Maskell theory [51] but it was not integrated when coding the current blockage model portion. The other classical BEM blockage models curves were generated at the three aforementioned representative Reynolds numbers. The classical BEM blockage model failed to converge at the corrected *TSR* less than 1.371. Moreover, due to the high rotational speed variation for the small-scale rotor, the classical blockage with constant Reynolds numbers poorly estimated the

power curve. No further investigation was made toward analyzing the representative Re. The left side of the experimental C_P curve was not completed because of the stall delay where the turbine stopped as a result of increasing the applied load. An experiment was also conducted for a six-blade turbine at the same flow speed and pitch angle. However, the BEM-NNs blockage model showed poor agreement (the results were not included). The reason of this poor agreement was not linked to the BEM-NNs blockage model performance but was likely due to how the blockage model [19] handled the high solidity of the six-blade turbine (0.222), which was double the solidity of the three-blade rotor. The blockage model [19] was originally performed for a low solidity two-blade turbine. Nevertheless, the solidity variation should have been considered as a model factor [23]. Other factors, besides the solidity that likely to affect the blockage model performance, are the *TSR* and pitch angle [22]. The time to execute the BEM-NNs blockage model was 12.2 min when it was run at the same operational conditions in case 1. This time was longer than the execution of BEM-NNs model in case 1, mainly due to the iterative calling of the two trained NNs for C_L and C_D calculation and secondly due to the blockage model calculation.

Table 5. Representative Reynolds numbers calculated at different operational incidents

Re_r	Rotational speed (*RPM*)	Flow velocity (m/s)	r/R_{rotor}
17543	50	0.8161	0.5722
72249	300	0.8161	0.7861
118672	500	0.8161	0.7861

8. CONCLUSIONS

8.1. NNS FOR C_L AND C_D PERFORMANCE

For the range of current evaluated data, increasing number of hidden neurons improved the NN performance. Excessively increased number of neurons declined the NN performance due to the overfitting. The optimum number of hidden layers was found to be 3H with [30-15-5] hidden neurons. Levenberg- Marquardt had slightly better correlation coefficient compared to the other tried training methods.

The integrated NNs successfully predicted the C_L and C_D at any operational condition met during the iteration of BEM model. However, close to the upper limit of the operational conditions (rotational speed above 350 *RPM* and flow velocity above 0.75 m/s), the lift coefficient was slightly underestimated at angles of attack neighboring the limits ($\pm 180^o$).

8.2. BEM-NNS PERFORMANCE

BEM-NNs successfully overcame the convergence problem that occurs during the BEM model iteration. The comparison with a conventional BEM model and a modified BEM model from the literature was promising. The suggested model was valid to run at higher *TSR* with no convergence issues. Furthermore, a blockage model was readily integrated into the BEM-NNs and the results were satisfactory for the low solidity turbine. The use of NNs to simulate the variation in the local C_L and C_D further enhanced the BEM performance compared to the BEM with a constant Re.

REFERENCES

[1] F. O. Rourke, F. Boyle, and A. Reynolds, "Marine current energy devices: current status and possible future applications in Ireland," *Renewable and Sustainable Energy Reviews,* vol. 14, no. 3, pp. 1026-1036, 2010.

[2] H. Yang, W. Shen, H. Xu, Z. Hong, and C. Liu, "Prediction of the wind turbine performance by using BEM with airfoil data extracted from CFD," *Renewable Energy,* vol. 70, pp. 107-115, 2014.

[3] H. Glauert, "Airplane propellers," in *Aerodynamic theory*: Springer, 1935, pp. 169-360.

[4] M. L. Buhl, *A new empirical relationship between thrust coefficient and induction factor for the turbulent windmill state*. National Renewable Energy Laboratory Golden, Colorado, USA, 2005.

[5] W. Z. Shen, R. Mikkelsen, J. N. Sørensen, and C. Bak, "Tip loss corrections for wind turbine computations," *Wind Energy,* vol. 8, no. 4, pp. 457-475, 2005.

[6] M. O. Hansen, *Aerodynamics of wind turbines*. Routledge, 2013.

[7] J. F. Manwell, J. G. McGowan, and A. L. Rogers, *Wind energy explained: theory, design and application*. John Wiley & Sons, 2010.

[8] R. E. Wilson and P. B. Lissaman, "Applied aerodynamics of wind power machines," Oregon State Univ., Corvallis (USA) 1974.

[9] T. Burton, N. Jenkins, D. Sharpe, and E. Bossanyi, *Wind energy handbook*. John Wiley & Sons, 2011.

[10] H. Li, G. A. Taylor, A. M. Abutunis, K. Chandrashekhara, A. R. Kashyap, and J. W. Kimball, "Design and performance evaluation of a hydrokinetic composite turbine system," presented at the SAMPE, Long Beach, CA, 2013.

[11] W. Batten, A. Bahaj, A. Molland, and J. Chaplin, "The prediction of the hydrodynamic performance of marine current turbines," *Renewable Energy,* vol. 33, no. 5, pp. 1085-1096, 2008.

[12] J. Chapman, I. Masters, M. Togneri, and J. Orme, "The Buhl correction factor applied to high induction conditions for tidal stream turbines," *Renewable Energy,* vol. 60, pp. 472-480, 2013.

[13] A. S. Bahaj, W. M. J. Batten, and G. McCann, "Experimental verifications of numerical predictions for the hydrodynamic performance of horizontal axis marine current turbines," *Renewable Energy,* vol. 32, no. 15, pp. 2479-2490, 2007.

[14] M. McWilliam and C. Crawford, "The behavior of fixed point iteration and Newton-Raphson methods in solving the blade element momentum equations," *Wind Engineering,* vol. 35, no. 1, pp. 17-32, 2011.

[15] I. Masters, J. Chapman, M. Willis, and J. Orme, "A robust blade element momentum theory model for tidal stream turbines including tip and hub loss corrections," *Journal of Marine Engineering & Technology,* vol. 10, no. 1, pp. 25-35, 2011.

[16] A. Ning, G. Hayman, R. Damiani, and J. M. Jonkman, "Development and validation of a new blade element momentum skewed-wake model within AeroDyn," *33rd Wind Energy Symposium*, pp. 5-9, 2015.

[17] S. A. Ning, "A simple solution method for the blade element momentum equations with guaranteed convergence," *Wind Energy,* vol. 17, no. 9, pp. 1327-1345, 2014.

[18] D. C. Maniaci, "An investigation of WT_perf convergence issues," presented at the 49th AIAA Aerospace Sciences Meeting including the New Horizons Forum and Aerospace Exposition, Orlando, FL, January 04 -07, 2011.

[19] J. Whelan, J. Graham, and J. Peiro, "A free-surface and blockage correction for tidal turbines," *Journal of Fluid Mechanics,* vol. 624, pp. 281-291, 2009.

[20] O. d. Vries, "Fluid dynamic aspects of wind energy conversion," DTIC Document1979.

[21] P. J. Moriarty and A. C. Hansen, *AeroDyn theory manual*. National Renewable Energy Laboratory Golden, Colorado, USA, 2005.

[22] T. Chen and L. Liou, "Blockage corrections in wind tunnel tests of small horizontal-axis wind turbines," *Experimental Thermal and Fluid Science,* vol. 35, no. 3, pp. 565-569, 2011.

[23] T. Kinsey and G. Dumas, "Impact of channel blockage on the performance of axial and cross-flow hydrokinetic turbines," *Renewable Energy,* vol. 103, pp. 239-254, 2017.

[24] A. Bahaj, L. Myers, R. Rawlinson-Smith, and M. Thomson, "The effect of boundary proximity upon the wake structure of horizontal axis marine current turbines," *Journal of Offshore Mechanics and Arctic Engineering,* vol. 134, no. 2, p. 021104, 2012.

[25] N. Kolekar and A. Banerjee, "Performance characterization and placement of a marine hydrokinetic turbine in a tidal channel under boundary proximity and blockage effects," *Applied Energy*, vol. 148, pp. 121-133, 2015.

[26] C. Garrett and P. Cummins, "The efficiency of a turbine in a tidal channel," *Journal of Fluid Mechanics*, vol. 588, pp. 243-251, 2007.

[27] G. Houlsby, S. Draper, and M. Oldfield, "Application of linear momentum actuator disc theory to open channel flow," *Report no. OUEL*, vol. 2296, no. 08, 2008.

[28] H. Li, K. Chandrashekhara, and R. S. Mishra, "Fatigue life investigation for a medium scale composite hydrokinetic turbine blade," 2012.

[29] M. Drela, "XFOIL: An analysis and design system for low Reynolds number airfoils," in *Low Reynolds number aerodynamics*: Springer, 1989, pp. 1-12.

[30] M. D. drela. (2013, February 3, 2017). *XFOIL, subsonic airfoil development system*. Available: http://web.mit.edu/drela/Public/web/xfoil/

[31] R. Oliveira. (2011, May 18, 2017). *XFOILinterface*. Available: http://www.mathworks.com/matlabcentral/fileexchange/30478-xfoil-matlab-interface

[32] S.-P. Breton, "Study of the stall delay phenomenon and of wind turbine blade dynamics using numerical approaches and NREL's wind tunnel tests," PhD, Department of Civil and Transport Engineering, Norwegian University of Science and Technology, 2008.

[33] I. Herráez, B. Stoevesandt, and J. Peinke, "Insight into rotational effects on a wind turbine blade using Navier–Stokes computations," *Energies*, vol. 7, no. 10, pp. 6798-6822, 2014.

[34] Z. Du and M. S. Selig, "A 3-D stall-delay model for horizontal axis wind turbine performance prediction," *AIAA Paper*, vol. 21, pp. AIAA-98-0021(1-19), 1998.

[35] A. Eggers, K. Chaney, and R. Digumarthi, "An assessment of approximate modeling of aerodynamic loads on the UAE rotor," *ASME 2003 Wind Energy Symposium*, pp. 283-292, 2003.

[36] L. A. Viterna and R. D. Corrigan, "Fixed pitch rotor performance of large horizontal ax is wind turbines," 1982.

[37] K. Gharali and D. A. Johnson, "Numerical modeling of an S809 airfoil under dynamic stall, erosion and high reduced frequencies," *Applied Energy*, vol. 93, pp. 45-52, 2012.

[38] F. R. Menter, "Two-equation eddy-viscosity turbulence models for engineering applications," *AIAA journal*, vol. 32, no. 8, pp. 1598-1605, 1994.

[39] I. H. Abbott and A. E. Von Doenhoff, *Theory of wing sections, including a summary of airfoil data*. Courier Corporation, 1959.

[40] C. Bak, P. Fuglsang, J. Johansen, and I. Antoniou, "Wind tunnel tests of the NACA 63-415 and a modified NACA 63-415 airfoil," Risø National Laboratory 2000.

[41] D. M. Somers, "Design and experimental results for the S809 airfoil," National Renewable Energy Lab., Golden, CO (United States)1997.

[42] A. Abutunis, G. Taylor, M. Fal, J. Nicholas, and K. Chandrashekhara, "Performance evaluation of coaxial horizontal axis hydrokinetic composite turbine system," presented at the Composites and Advanced Materials Expo (CAMX) Conference, Dallas, TX, October 26 - 29, 2015, 2015.

[43] L. Myers and A. S. Bahaj, "Power output performance characteristics of a horizontal axis marine current turbine," *Renewable Energy*, vol. 31, no. 2, pp. 197-208, 2006.

[44] A. S. Yilmaz and Z. Özer, "Pitch angle control in wind turbines above the rated wind speed by multi-layer perceptron and radial basis function neural networks," *Expert Systems with Applications*, vol. 36, no. 6, pp. 9767-9775, 2009.

[45] J. Hu, S. Sundararaman, V. Menta, K. Chandrashekhara, and W. Chernicoff, "Failure pressure prediction of composite cylinders for hydrogen storage using thermo-mechanical analysis and neural network," *Advanced Composite Materials*, vol. 18, no. 3, pp. 233-249, 2009.

[46] H. Li, K. Shi, and P. McLaren, "Neural-network-based sensorless maximum wind energy capture with compensated power coefficient," *Industry Applications, IEEE Transactions on*, vol. 41, no. 6, pp. 1548-1556, 2005.

[47] H. Gaja and F. Liou, "Defects monitoring of laser metal deposition using acoustic emission sensor," *The International Journal of Advanced Manufacturing Technology*, vol. 90, no. 1-4, pp. 561-574, 2017.

[48] H. Gaja and F. Liou, "Defect classification of laser metal deposition using logistic regression and artificial neural networks for pattern recognition," *The International Journal of Advanced Manufacturing Technology*, vol. 94, no. 1-4, pp. 315-326, 2018.

[49] K. Hornik, M. Stinchcombe, and H. White, "Multilayer feedforward networks are universal approximators," *Neural Networks*, vol. 2, no. 5, pp. 359-366, 1989.

[50] A. S. Bahaj, A. F. Molland, J. R. Chaplin, and W. M. J. Batten, "Power and thrust measurements of marine current turbines under various hydrodynamic flow conditions in a cavitation tunnel and a towing tank," *Renewable Energy,* vol. 32, no. 3, pp. 407-426, 2007.

[51] E. Maskell, "A theory of the blockage effects on bluff bodies and stalled wings in a closed wind tunnel," DTIC Document 1963.

II. EXPERIMENTAL EVALUATION OF COAXIAL HORIZONTAL AXIS HYDROKINETIC COMPOSITE TURBINE SYSTEM

A. Abutunis, G. Taylor, M. Fal, and K. Chandrashekhara

Department of Mechanical and Aerospace Engineering

Missouri University of Science and Technology, Rolla, MO 65409

ABSTRACT

Hydrokinetic energy conversion systems are emerging as a viable solution for harnessing kinetic energy. However, the typical deployment location is highly space-constrained due to both the nature and the other uses of the river. Therefore, a modified conversion device to overcome these constraints is preferred. The research objective of this work was to evaluate and enhance the performance of multiple coaxial horizontal axis hydrokinetic turbines (HAHkTs) mounted on a single shaft. The hydrodynamic performance of different configurations of single and multi-coaxial HAHkT systems with composite blades was evaluated experimentally in a water tunnel. Increasing the number of rotors of the turbine system from one to two rotors enhanced the efficiency by approximately 75% and lowered the operational tip speed ratio. The third rotor also enhanced the efficiency but improvement was less due to the slower flow passing this rotor. A duct reducer was also incorporated and its effect was studied. Finally, the wake behavior and its effect on the multi-turbine system's operation were examined by using a particle image velocimetry system. From the structure aspect, composite materials have the

appropriate properties that suit the water turbine blades. The composite turbine blades were manufactured using the out-of-autoclave process.

1. INTRODUCTION

HAHkTs are designed to be deployed in river streams and marine currents to convert the kinetic energy flux into mechanical energy. Then, generators are used to convert the mechanical energy into electrical energy. The operational principle of the HAHkT is similar to the horizontal axis wind turbine (HAWT) with the exception of the existing effects of free surface and cavitation phenomenon. Although the range of a river's current (1-3 m/s) is slower than wind's speed (11-13 m/s), HAHkTs offer higher energy generation per unit square of rotor swept area. In some instances, the power generated by a HAHkT may reach four times as much power per year/m^2 of swept area as that of similar size HAWT [1]. The reason is that the water is approximately 830 times denser than the air which allows for higher kinetic energy conversion per unit area.

Unlike a wind turbine, hydrokinetic systems can assume that the flow direction is effectively fixed. Therefore, yaw control is of less concern, and structures may be built around the turbine to control the flow. For example, a duct reducer/diffuser may be used to modify the local flow velocity magnitude and direction and additionally to protect the turbine from debris.

The United States is abundant with rivers. The yearly coverable hydrokinetic energy of the rivers in the United States is approximately 119.9TWh [2]. Unfortunately, a large portion of streams flow down the shallow river beds causing the kinetic energy to

dissipate over long distances [3]. The deployment of hydrokinetic turbines in these rivers will collect this energy before it is lost and offer significant economic advantages to the neighboring communities. However, several economic and technical challenges must be overcome before commercialization.

Over the last two decades, several studies have been performed to establish better knowledge about flow dynamics and the effect of various aero/hydrodynamic parameters on turbine output. Batten et al. [4] conducted experiments in a cavitation tunnel and performed a numerical method using blade element momentum (BEM) theory. Their results illustrated how changes in both pitch angle and hydrofoil camber can affect the delay stall performance and cavitation inception for marine current turbines.

Subhra et al. [3] performed computational fluid dynamics (CFD) simulation to investigate the solidity and number of blades effect on HAHkT performance. They found that 3-blade HAHkT with untwisted blades generated more power than 2-blade or 4-blade turbines that had the same solidity. It was also found that the power peak sifted to lower *TSR* as the solidity increased. Ashrafi et al. [5] employed a BEM model to investigate the effect of flow variation on HAWT performance. They found that the change in wind speed affects the design parameters and causes a decline in the turbine efficiency when operates off-design operational conditions. To improve the off-design performance, they developed a non-linear function that is to be incorporated to maintain the optimum pitching which results in maximum harvested power. Duquette and Visser [6] used a simple BEM theory, with different commonly used corrections (e.g., corrections for tip and hub losses and for rotational effects), to examine HAWT with untwisted blades. They found that increasing the number of blades at a given solidity will always increase the maximum C_P. The

optimum *TSR* was strongly affected by solidity alteration but was slightly influenced by the change in the blade number.

A number of researchers have studied the duct diffuser inner and outer shape and duct components in an attempt to improve the turbine aero/hydrodynamic efficiency [7-9].

Similar to the wind farm turbines, the performance of the latter rotors in the multi-turbine system is influenced by the upstream wake that generated by the frontal rotors. Analyzing the development of wake and wakes-interaction is essential for improved performance of turbines operating in a wind farm. Several researchers conducted experimental and numerical studies to investigate the structure of wake and wakes-interaction and their effect on power generation (see for example [10-13]).

Traditional HAHkTs suffer from low-efficiency as a result of their non-optimized rotor configuration. Solidity, for example, has a great effect on turbine performance. For a single HAHkT, increasing the rotor solidity has a favorable effect on the turbine performance. However, increasing the solidity beyond its optimum limit causes a decline in the generated power because of the high flow impediment [3, 6, 14]. Moreover, extremely high rotor solidity (larger chord) requires a stronger blade structure (more composite layers) to withstand the large thrust force loading. Increasing rotor's swept area can also influence the generated power but is limited by the river depth.

In this work, a multi-turbine system of two/three rotors mounted coaxially to a single shaft was employed to mitigate the high solidity effect resulting from increasing the blades' chord or adding blades to the same rotor. Using the coaxial turbine system can also overcome the limitation on the swept area of the rotor (more rotors increases the swept area). Another key advantage of the proposed approach is that the increase in power

requires one large generator and a single power convertor, rather than multiple smaller generators and power converters per HECS such as in wind farm case. Since generator performance metrics tend to improve with the power rating, one large generator is generally more effective than multiple small generators that add up to the same rating. Control effort is reduced as well, with fewer shaft speeds to control and fewer converters to synchronize or otherwise coordinate. The installation cost and electrical losses in the cables and generators are also reduced.

From the structural aspect, the high kinetic flux by the water stream means that the turbine blades undergo significant loadings during operation. Thus, the bending moment at the blades' root and deflection at the blades' tip are of main concern during the designing and manufacturing of the water turbine blades. Composite materials (especially, carbon fibers) possess properties of high specific strength, specific stiffness, and corrosion resistance that suit marine energy applications [15, 16]. Composite blades are advantageous over the traditional modeled metal blades because composite blades are corrosion-resistant, lighter and have high durability in long-term operation [17]. Moreover, carbon fiber reinforced polymer composite (used in this work) possess high stiffness that causes less deflection of the operating blades which reduces hydrodynamic losses [16]. In the current work, an effort was made to design and build a small-scale horizontal axis turbine with composite blades. The material chosen for the blades was carbon/epoxy prepreg, and the manufacturing technique employed was out-of-autoclave. The manufactured composite turbine then was tested in the water tunnel for the performance evaluation of single and multi-turbine systems.

2. TURBINE SYSTEM TERMINOLOGY AND THEORY

2.1. HYDRODYNAMIC PARAMETERS

HAHkTs performance is controlled by different parameters such as tip speed ratio (*TSR*), flow velocity (U_∞), solidity (σ), blade number (*N*)**,** pitch angle (θ), angle of attack (α), and swept area (*A*). These parameters interact with each other and affect the power output of the turbine in a complex manner. The output power (*P*) and power coefficient (C_P) are given by

$$P = T\omega \tag{1}$$

$$C_P = \frac{P}{\frac{1}{2}\rho U_\infty^3 A} \tag{2}$$

where *T* is the torque magnitude (N.m), ω is the rotational speed (rad/sec), and ρ is the water density (kg/m^3). The denominator, $1/2\ \rho U_\infty^3 A$, in Equation 2, is the kinetic energy passing through the rotor's swept area. The tip speed ratio is another important parameter to consider when designing hydrokinetic turbines because the power coefficient is affected by this ratio. It is also adequate when comparing similar turbines with different sizes [18]. The tip speed ratio is defined as the ratio of the blade tip tangential speed (ωR) to the incoming flow velocity, where *R* is the turbine radius

$$TSR = \frac{\omega R}{U_\infty} \tag{3}$$

Turbine solidity is proportional to the number of blades and the blade chord length (*c*). The local solidity is defined as the ratio of the local chord length of all of the blades to the circumference of the rotor

$$\sigma_r = \frac{Nc_r}{2\pi R} \tag{4}$$

where *r* represents a local property of a hydrofoil located at an *r* distance from the rotor center.

2.2. BLADE ELEMENT MOMENTUM THEORY

Blade element momentum (BEM) theory [19, 20] was used in this work to analyze the stall characteristics along the blade span which provided a better understanding of the efficiency curve behavior. The BEM theory couples blade element theory and momentum theory and utilizes a numerical method (e.g., fixed-point iterative) to iteratively calculate blade sectional properties such as reduced velocities, angle of attack, and forces. To improve the solution accuracy of the BEM model, two correction models were integrated to account for the tip and hub losses [21], correct the thrust coefficient [22]. In the present section, only the equations related to the calculation of the reduced velocity and angle of attack are discussed.

The theory equates the two sectional thrust equations and the two sectional moment equations generated from both the blade element and momentum theories. Equating these equation allows for the calculation of the axial (*a*) and tangential (*a'*) induction factors

$$a = \frac{1}{\frac{4F_r sin^2 \emptyset_r}{\sigma_r C_{n_r}} + 1} \tag{5}$$

$$a' = \frac{1}{\frac{4F_r sin\emptyset_r \cos \emptyset_r}{\sigma_r C_{t_r}} - 1}, \tag{6}$$

where F_r is the total loss factor (accounts for both tip and hub losses) as defined in [21]. $\emptyset_r$ is the local incoming flow angle (illustrated in Figure 1) and defined as

$$\emptyset_r = arctan\left(\frac{(1-a)U_\infty}{(1+a')\omega r}\right), \tag{7}$$

where the induction factors, a and a', in Equation 7 are assigned the values from the previous iteration (initial values are zeros). The sectional properties C_{n_r} and C_{t_r} in Equation 5 and 6 are the normal and tangential forces coefficients respectively and calculated from

$$C_{n_r} = C_l\, cos\emptyset_r + C_d\, sin\,\emptyset_r \tag{8}$$

$$C_{t_r} = C_l\, sin\emptyset_r - C_d\, cos\,\emptyset_r, \tag{9}$$

where C_l and C_d are the lift and drag coefficients respectively that calculated at an operational Reynolds number, approximately 0.858×10^5, using XFoil panel method [23]. The operational Reynolds number was obtained based on the sectional properties at approximately 70% of the blade span (This 70% is an appropriate span for the design investigation [24, 25]). The XFoil output two-dimensional (2D) C_l and C_d data were corrected to account for the rotational effect. The model provided by Du and Selig [26] was applied to correct C_l and the model developed by Eggers et al. [27] was employed to correct C_d. The corrected hydrofoil properties to account for rotational effects are shown in Figure 2a. The sectional angle of attack (α_r), as illustrated in Figure 1, is given by

$$\alpha_r = \emptyset_r - \theta_r \tag{10}$$

where θ_r is the local pitch angle defined by the angle between the local blade chord and the rotor's plane of rotation. Finally, after the BEM model converged (the change in two consecutive a and a' are less than a given tolerance), the sectional hydrodynamic properties

are available. The total rotor torque and thrust are attainable through the integration of the sectional moment and thrust along the blade span. The power then is calculated using equation 2. The results generated by the BEM theory were validated against the experimental results as illustrated in Figure 2b. Good agreement between the predicted and the experimental results was observed. However, predicted C_P deviated from experimental C_P toward increased *TSR* which was likely due to XFoil over-predicting C_l within the stall regions which caused by the inaccurate estimation of the transition location [28, 29].

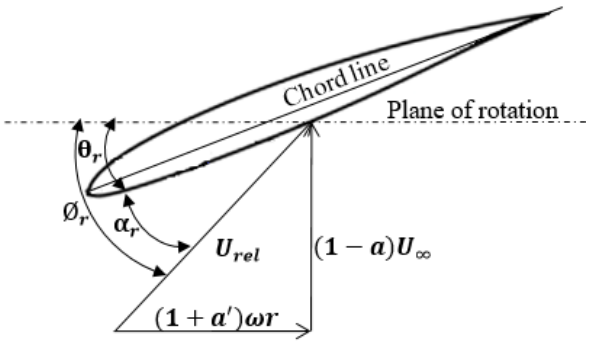

Figure 1. Sectional pitch angle and angle of attack

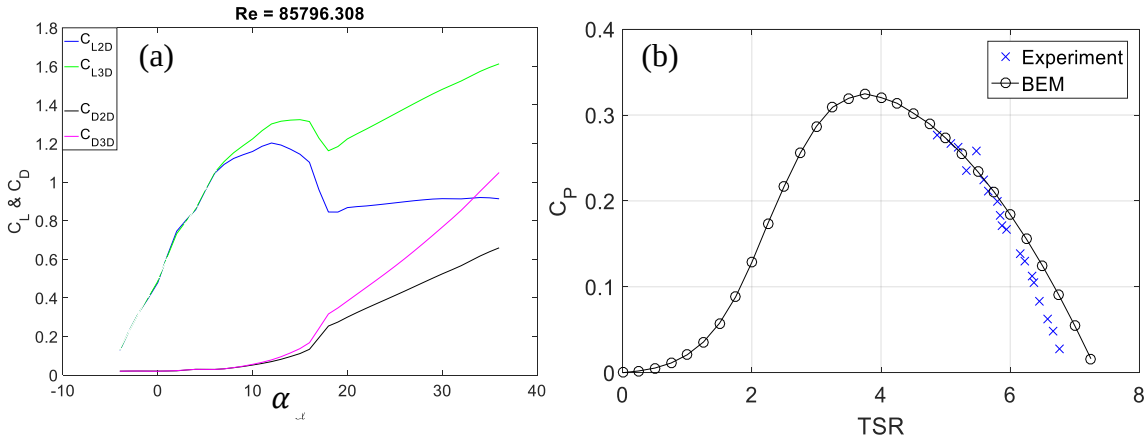

Figure 2. (a) Corrected C_l and C_d to account of rotational effects and (b) BEM results validation

3. EXPERIMENTAL METHODOLOGY

3.1. EXPERIMENTAL SETUP

3.1.1. Water Tunnel. The proposed hydrokinetic turbine systems were tested at the water tunnel facility at Missouri University of Science and Technology (Missouri S&T). The Water Tunnel Laboratory at Missouri S&T is a Rolling Hills Research Corp. model 1520-HK with test section dimensions of 0.381 m (15 in) wide, 0.508 m (20 in) deep, and 1.524 m (60 in) long. The test section surfaces were made principally of tempered glass to allow maximum viewing of the tested model. The maximum water velocity that could be reached in the test section was approximately 1 m/s. A speed controller was used to vary a pump engine frequency in the range between 2.5 to 40 Hz so that the flow speed in the test section could be controlled. An illustration of the facility used in this study is given in Figure. 3.

3.1.2. Hydrokinetic Composite Turbine. The 3-blade and 6-blade horizontal axis hydrokinetic turbines that were used in this study had a radius of 10.896 cm (4.29 in). These composite blades had untwisted and constant chord. Twisted blades have been proven to have better performance compared to their counterparts (the untwisted blades). Twisted blades can yield lift at low drag while providing better starting torque. Moreover, twisted blades can have a larger range of operational *TSR*. Whereas, untwisted blades are beneficial for small and medium turbines owing to the ease in manufacturing, thus low cost [30, 31]. The blade's Eppler 395 hydrofoil was chosen because it provides a high lift to drag ratio (C_l/C_d) [32].

The 3-blade turbine hub was 25.4 mm (1 in) diameter and had two components to clamp the blade's root so the blade pitch was adjustable. The 6-blade turbine hub was 31.75 mm (1.25 in) diameter and was one component with a set of setscrews placed at the bottom of the hub, fixing the blades' roots firmly. Both hubs were made of aluminum.

3.1.3. Turbine System Configuration. The turbine system (see Figures 3, 4, and 6) was comprised of one, two, or three rotors as well as transmission shafts. The mechanical power generated by the turbine system's rotors was transmitted to sensors platform (torque and the rotational speed sensors assembly) via two coupled horizontal shafts and one vertical shaft. A bevel gear was used to connect the vertical and horizontal transmission shafts. Figure 3a shows the turbine system with three rotors operating inside the water tunnel test section and Figure 3b shows a closer view of the sensors platform assembly.

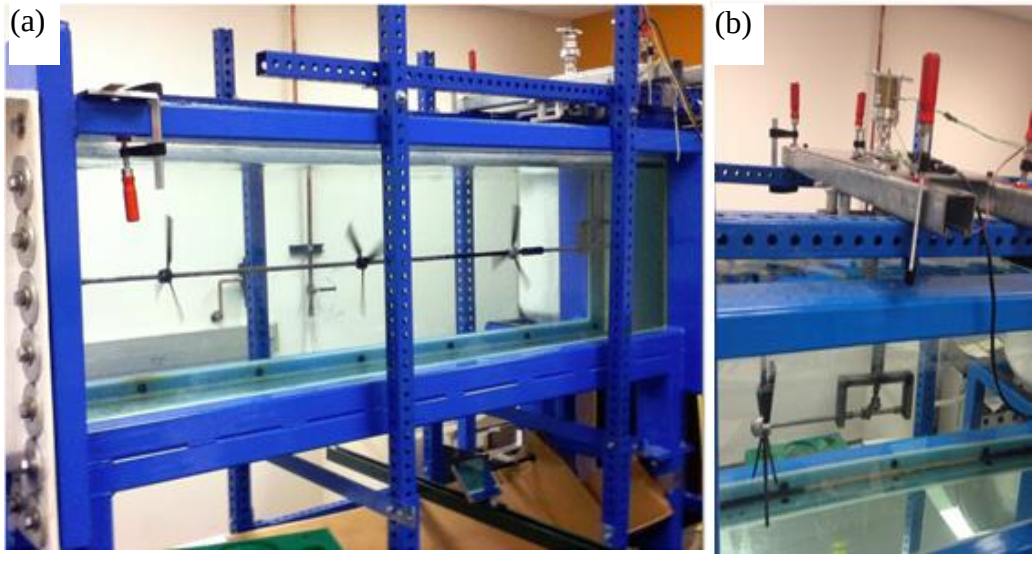

Figure 3. (a) Multi-turbine system operating in a water tunnel and (b) sensors platform assembly

The multi-turbine system was arranged to have either two or three rotors attached to the same horizontal shaft by using setscrews. The rotors' blades were pitched to 20º. The axial distance between the rotors (x) and the rotors' relative installation angle (the azimuth angle difference, ϕ) were varied. Figure 4 demonstrates these two experimental parameters.

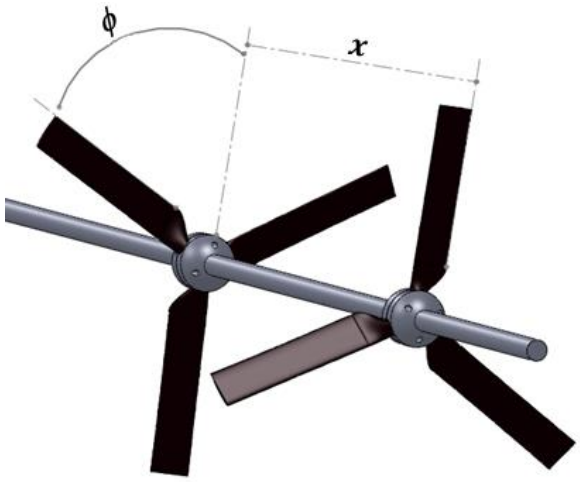

Figure 4. Multi-turbine system with axial distance (x) and relative installation angle (ϕ)

3.1.4. Duct Reducer. A duct reducer was used to enhance the flow through the turbine rotor(s) thus increasing the generated power. The duct reducer was comprised of LaserLock galvanized metal that had a thickness of 1.27 mm (0.05 in.). The entire duct consisted of two parts. The front part (the reducer), which accelerated the flow, had a length of 0.1905 m (7.5 in.), an inlet diameter of 0.3048 meters (12 in.), and an outlet diameter of 0.2286 meters (9 in.). The rear part (the pipe), which housed the multi-turbine system, had a length of 0.9017 meters (35.5 in.) and a diameter of 0.2286 meters (9 in.). The multi-turbine system positioned at the center of the rear part. The gap between the blade tip and

the housing rear part inner walls was 5.334 mm (0.21 in). The gap size may have effect on the multi-turbine system performance, but it was not investigated in this study. All duct dimensions are provided in Figure 5b. The two parts were joined by a clamp, and the entire assembly was hung on the water tunnel's shoulders as illustrated in Figure 5a. An outlet diffuser and a flange around the exit can further enhance the duct performance [8, 33], but they were not integrated due to the water tunnel size limitation.

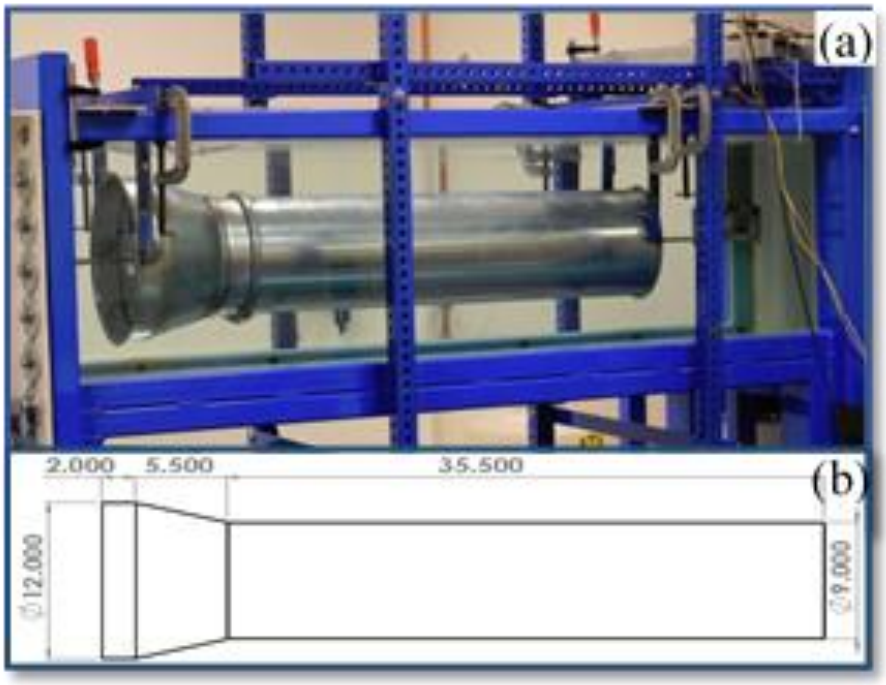

Figure 5. (a) Shrouded multi-turbine system operating in the water tunnel and (b) dimension of the duct reducer

3.1.5. Experimental Data Acquisition Devices. The experiment outputs were the torque and rotational speed which were required to calculate the harvested power by the turbine system (see Equation 1). A FUTEK reaction time-averaged torque sensor (TATS) with maximum torque of 0.353 N.m (50 in-oz) was used to measure the system's

output torque. The torque sensor was aligned with and attached at its upper end by a magnetic particle clutch C2 which had a maximum torque of 0.226 N.m (32 in-oz.). The lower end of the torque sensor was rigidly attached to the platform of the sensors assembly. The clutch shaft was coupled through a universal joint to the top end of the turbine system's vertical output shaft (see Figure 6). The torque sensor was then wired to a FUTEK USB210 device (which works as a data acquisition.) This device continually received and stored torque data signals. Then, the data was transferred to a LabVIEW interface program that provides the average torque continuously. A power supply with controllable voltage and current was connected to the clutch to control the applied torque.

A time-averaged rotational speed (TARS) sensor was used instead of the traditional tachometer to account for the fluctuations in the rotor's rotational speed reading and thus ensure the accuracy of the collected data. The rotational speed sensor was developed in the lab and was comprised of a Hall Effect sensor, an earth magnet, a breadboard, a data acquisition device (NI myDAQ), and a LabVIEW interface. The Hall Effect sensor was wired and embedded in a plastic case. It was then properly glued to protect the sensor and to ensure firm joints between the sensor ports and the wires. The Hall Effect sensor was mounted on the sensors assembly platform, 3 mm apart from the magnet that was attached earlier to the turbine's output vertical shaft. The data acquisition device received and processed signals from the sensor and transported them to the LabVIEW interface program which in turn outputs the averaged rotational speed over a predefined period of time (this detection time was compatible with the time used to collect the averaged torque).

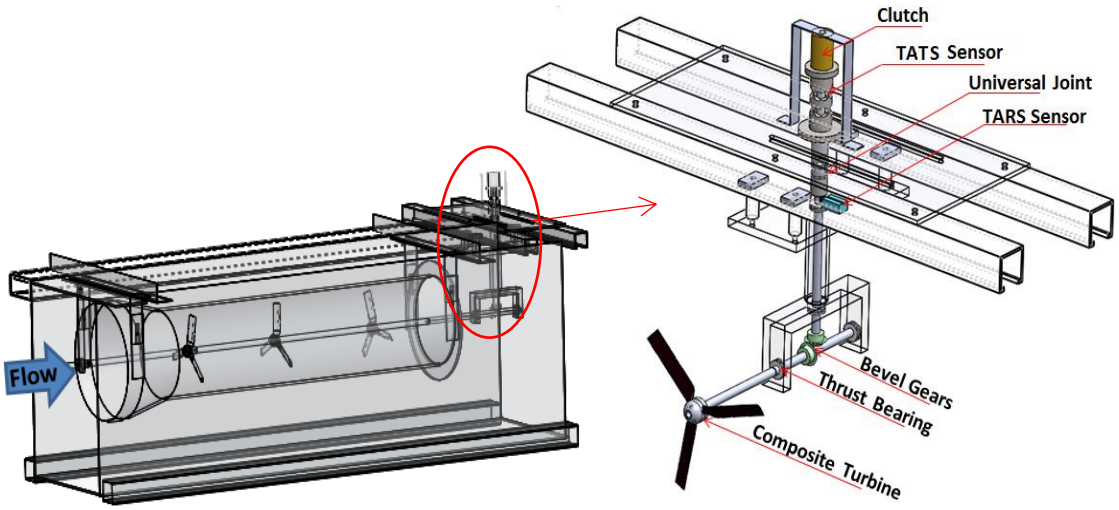

Figure 6. Schematic of torque and *RPM* sensors assembly setup

3.1.6. Blade Manufacturing. Out-of-autoclave (OOA) technique was employed to manufacture the composite blades. Figure 7a shows a mold (ULTEM 9085 obtained from Stratasys) for an Eppler 395 hydrofoil that was used to form the turbine's composite blades.

OOA process began by placing the upper and lower molds on an aluminum plate. For each mold, three layers of carbon fiber/epoxy prepreg (Cycom 5320) were cut to dimension and laid up in the order of 0º/90º/0º (angles are referenced to the mold's longitudinal direction). Next, each set of three layers was placed between two layers of Ethelyne Tetra Fluoro Ethylene (ETFE). The prepreg stacks were then placed on and aligned to the molds (ULTEM 9085). The ETFE was used so that the manufactured blade parts would be easy to remove after curing was completed. A layer of Airweave N10 breather was applied to cover the two molds. An outlet air valve was placed on the breather, and the entire aluminum plate was sealed using a vacuum bag (see Figure 7b). Vacuum of

760 mm (29.92 in) of Hg was applied, and the sample was put in an oven and cured according to the manufacturer's recommended cure cycle.

The cured upper and lower parts of the composite blade were matched and adhered together using an acrylic epoxy. A steel rod was fitted to the inside of the composite blade's root to serve as reinforcement. Finally, the blade's span length was trimmed down to 96.32 mm (3.79 in.) to reduce the high blockage effects (blockage ratio was approximately 20%). The blade lateral edges were trimmed and sanded down to the foil chord width of 16.76 mm (0.66 in). Figure 7c is an image of manufactured blades before and after cutting and polishing.

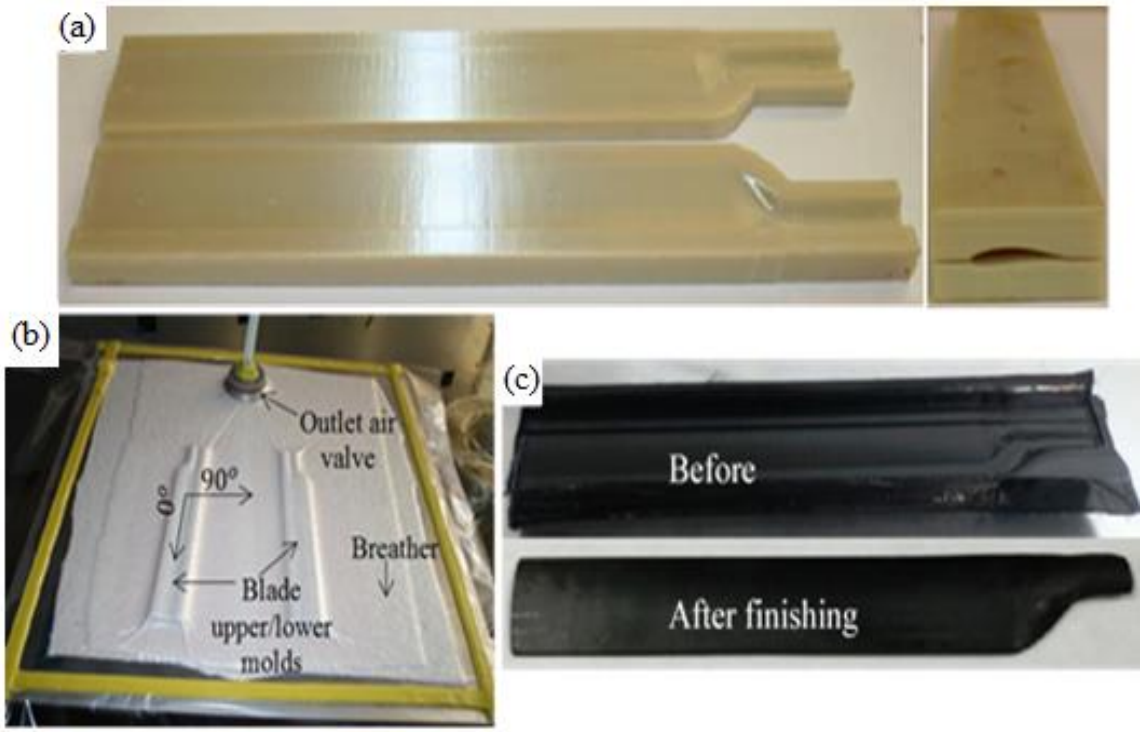

Figure 7. (a) Composite blade upper and lower molds, (b) out-of-autoclave technique, and (c) manufactured composite blades before and after finishing

3.1.7. Experimental Calibration. The particle image velocimetry (PIV) system was used to calibrate the water tunnel because the sensors could either deviate or fail over time. The calibration was performed to validate the relationship between the water tunnel flow velocities and pump engine frequencies originally submitted by the water tunnel's manufacturer. The integrated torque sensor was calibrated out of the water tunnel using a set of similar weights (8.45 gm) and a wheel. The wheel was attached to the torque sensor assembly horizontal shaft. In order to simulate the torques acting on the rotor, the weights were added gradually to a light bag that was attached to the wheel. This torque sensor calibration was done to account for the turbine system friction torque and to obtain a relationship between the sensor output signals and the applied torque An electrical engine (with a speed controller) was used to calibrate the time-averaged rotational speed sensor at various rotational speeds.

3.2. TESTING PROCEDURES

The turbine system assembly was placed upon the water tunnel shoulders close to the test section exit. The rotor was centered across the width of the test section perpendicular to the incoming flow. The water level was maintained at 50.8 mm (2 in.) below the water tunnel's shoulders edges. This level was considered for two purposes: (a) prevent the water from spilling over the walls during the test and (b) avoid the effect of changing the free surface proximity on the power output [34, 35].

Even though the blockage created by a turbine operating in a channel will increase the potential extracted energy [36-38], no considerations were taken to correct this increase

in the experimental results. The reason was that all the turbine arrangements had a similar moderate swept area (the blockage ratio was approximately 20%).

Four sets of experiments were performed in the water tunnel to study small-scale HAHkT with various configurations. The first experiment was to provide insight into the operating characteristics of a 3-blade single-turbine. The performance of the multi-turbine system with both two and three rotors was evaluated in the second experiment. In the third experiment, the duct reducer was used and its effect on the single-turbine system and the multi-turbine system performance was examined. The PIV was used in the last experiment to examine the downstream flow pattern and analyze its effects on the turbine system performance.

3.2.1. Pitch Angle and Flow Velocity. The 3-blade single-turbine system's performance was examined at different pitch angles. For each pitch angle, the turbine system was exposed to different flow velocities ranged between the cut-in speed to the flow speed of 0.9789 m/s.

3.2.2. Multi-turbine System. The second set of experiments was conducted to investigate the multi-turbine system's performance at different configurations. All of the rotors in the multi-turbine system were tested at a pitch angle of 20º. To investigate C_P versus *TSR* relationship, several runs were performed at different flow velocities (0.7272, 0.8146, 0.8996, and 0.9789 m/s). From the gathered data, representative curves were plotted for each test. The turbine system loaded torque was increased gradually, at proper increments, for each of these flow velocities until the system came to a complete rest. The distance *x* between the rotors was varied to have lengths of either 2 dia. or 4 dia. (where

dia. is the turbine diameter). For each axial distance, the angle ϕ between consecutive rotors' blades was also changed to be either 0º or 60º.

3.2.3. Duct Reducer. In the third experiment, the duct reducer was utilized to compare performance change through measured power in both single and multi-turbine systems under enhanced flow speeds. Here, the pitch angle remained the same (20º) for each system. In the multi-turbine system, the distance *x* was fixed to 2 dia. due to duct length limitations. The angle ϕ was fixed at 60º.

3.2.4. Flow Visualization Experiments. The final experiment utilized a PIV system to examine the effects of the number of blades (i.e., solidity) and downstream distance on the wake structure. The study of the wake provides details about the turbine's energy loss at an ambient flow condition. Moreover, investigation of the far wake region helps improve the arrangement of the rotors in the multi-turbine system.

Each run in this experiment used either a 3-blade or 6-blade turbine pitched to 20º. The rotor was referenced to a reference point downstream so that the axial distance effect behind the rotor could be investigated. A digital camera (with a CCD chip) was leveled and adjusted to point toward the test section, covering the area of interest. Seeding particles of glass spheres (with a mean diameter of 9-13 μm and a density of 1100 kg/m3) were dispersed in the water tunnel. A laser (with a cylindrical lens) was used to shoot a laser sheet at a mirror at the bottom of the test section. This mirror reflected the laser sheet upward. Then, the mirror was adjusted until the laser sheet was aligned with the center of the turbine axis as illustrated in Figure 8.

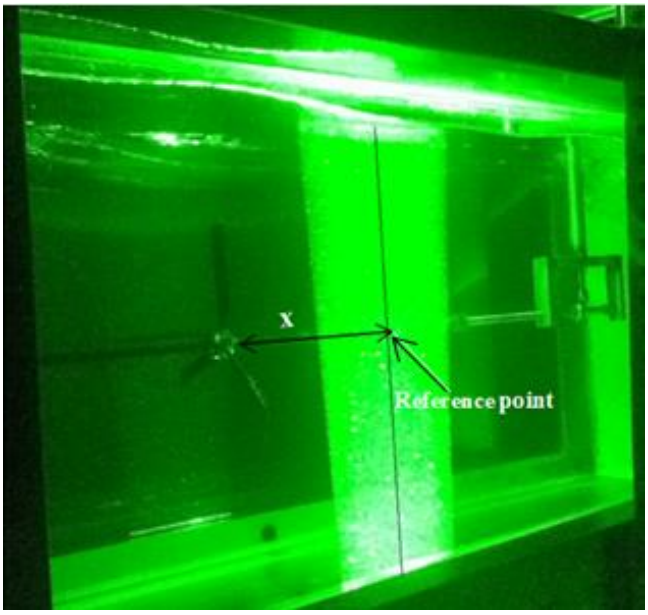

Figure 8. Centered laser sheet at distance *x* behind the rotor

4. RESULTS AND DISCUSSION

4.1. THREE-BLADE SINGLE-TURBINE OPERATING CHARACTERISTICS INVESTIGATION

Figure 9 illustrates P and C_P versus U_∞ for different θ when the applied torque is 0.0153 N.m. Figure 9a demonstrates that P increases as θ decreases from 20º to 5º. Comparing the pitch angle 5º with 20º, P is doubled (at $\theta = 5º$). This increase occurs because of the angle of attack, α, increases as θ decreases (see Equation. 10), allowing more lift to be exerted by the flow on the pressure side of the blade. It was observed that P increases, at given θ, as the flow velocity increases. This increase is caused by the higher kinetic energy flux passing the rotor's swept area (see Equation 2). On the other hand, this increase in U_∞ causes the turbine angular velocity, ω, to increase at a faster rate; therefore, the ratio (U_∞/ω) decreases. This causes α to decrease, which in turn decreases the C_P (Figure

9b). A hydrofoil section located at 80% of the blade span was examined to validate this decrease in α. Here, the blade's pitch angle was set to 5º, and the applied torque was approximately 0.015 N.m. Using the experimental data with a simple calculation (no reduced velocity was considered, $\emptyset_r = U_\infty/\omega r$), it was found that α decreased from 8.2271º to 4.3418º as the flow velocity increased from 0.4939 to 1.0054 m/s. Thus, at a higher free stream velocity, a higher relative velocity, U_{rel}, strikes the pressure side of the blade with a smaller α. This behavior causes a smaller percentage of the available kinetic energy to be captured. Consequently, relatively higher P and lower C_P may be resulted (as compared to the lower flow velocity). It was also observed that at a specific applied torque, decreasing the pitch angle is always combined with an increase in the rotor's angular velocity. However, the turbine tends to stop at lower applied torque when the rotor is gradually loaded. Reducing the pitch angle to 2º produces a lower P and a lower C_P. It can be theorized that this decline in performance is partially due to the small pitch angle causing a larger portion of the turbine blades' spans to operate at angles of attack above a stalled α. Moreover, blades pitched to angles less than 5º observed to have larger tip deflection (under the effect of thrust force) than the blades pitched to angles higher than 5º. This larger tip deflection also takes part in the decline of the rotor's efficiency.

The C_P peak has leftward shift (lower TSR) and lower magnitude as the pitch angle increases (Figure 10). In general, C_P increases for all pitch angles as the TSR decreases. This was due to the increase in the angle α along the blade length as observed in Figure 11.

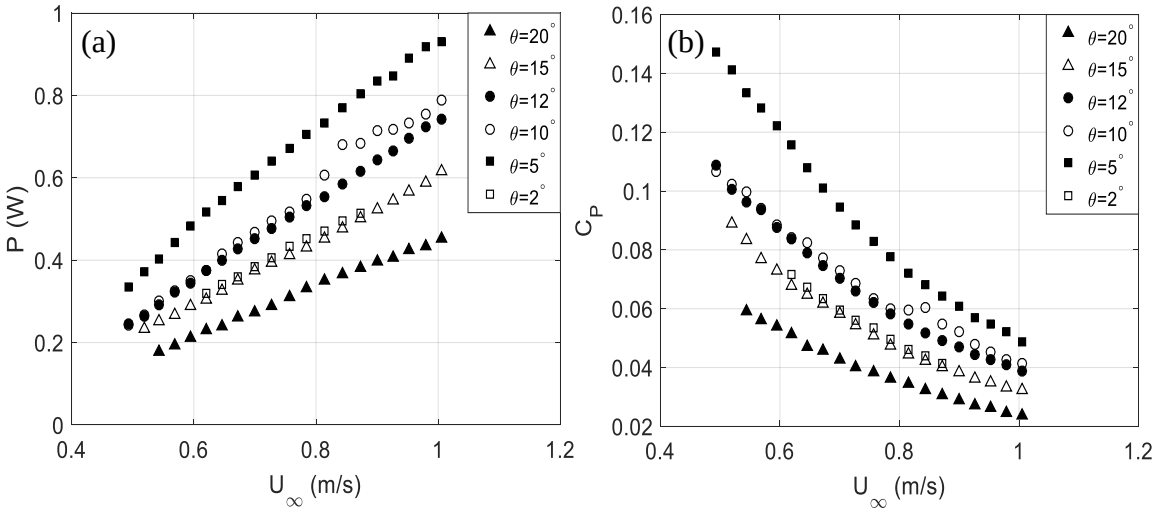

Figure 9. (a) P and (b) C_P vs. U_∞ at various pitch angles

The relationship in Figure 10 is linear at higher *TSR* for defined pitch angles (e.g., at a *TSR*>5.75 when the turbine has a pitch angle of 5º). A large percentage of the blade's length (approximately 70% of the outboard section of the blade) operates either below or close to the stall α (Figure 11). Reducing the *TSR* so that it is near its optimum value (e.g., 4.75< *TSR*<5.25 when θ=5º) decreases the rate at which the C_P changes. This decline in the slope is caused by a larger portion of the inboard part of the blade operates above the stall α as *TSR* decreases (Figure 11). If *TSR* was more decreased, the stalled portion of the blade would increase which would cause a decline in C_P. This left side of the C_P curve, where power starts to decline, was not reached because of the stall delay where the turbine stopped as a result of increasing the applied load.

Figure 11 was generated using the blade element momentum model [19, 20]. The stall α and hydrodynamic properties (C_l and C_d) were obtained from the 2D panel code, XFoil (discussed in Section 2.2).

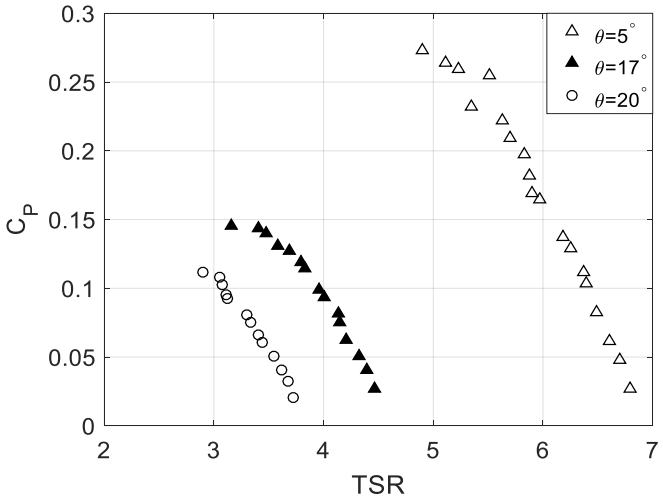

Figure 10. C_P vs. *TSR* for 3-blade single-turbine operates at U_∞ of 0.9789 m/s

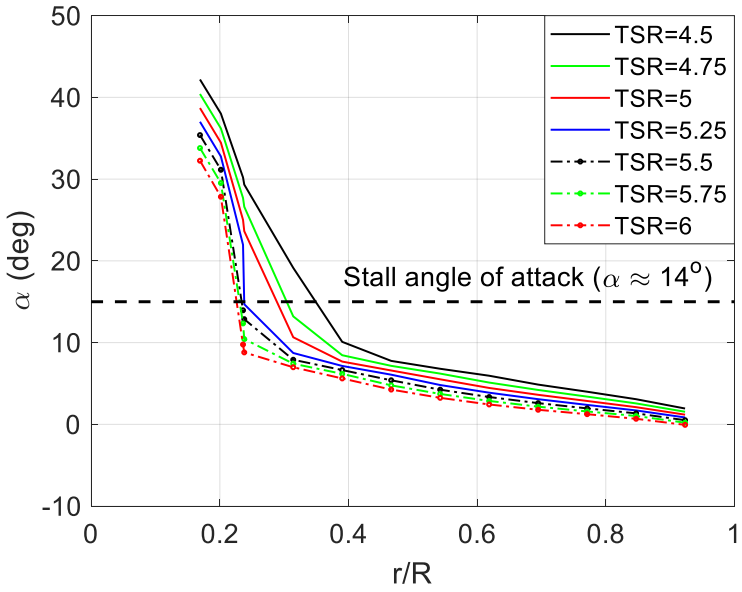

Figure 11. Angle of attack along the blade's span when θ was 5º and U_∞ was 0.9789 m/s

An experiment was also conducted to examine the effect of flow velocity on *P* and C_P versus *TSR*. At specific *TSR*, both *P* and C_P are proportional to the flow stream velocity (Figures 12a and 12b). However, this seems to be not consistent with Figure 9b where C_P

has a non-proportional relationship with the flow velocity. In fact, the turbine's rotational speed will be greater when it is exposed to a higher flow velocity. The applied torque must be higher for this turbine to operate at the same *TSR* as when it is exposed to a lower flow velocity. Based on the flow conditions and hydrofoil shape this higher applied torque may result in a large increase in α before the stall. This delay in the stall is attributed to rotational effects caused by both centrifugal and Coriolis forces [39, 40]. Consequently, the yielded C_P is higher because this angle α is larger than when the turbine is exposed to a slower flow. To confirm this finding does not conflict with the data illustrated in Figure 9b, red circles were drawn to border a group of four points that were generated when the turbine was loaded with approximately the same torque and exposed to different flow velocities (see Figure 12b). This figure is consistent with the data plotted in Figure 9b; C_P decreases as the flow velocity increases if the torque is fixed.

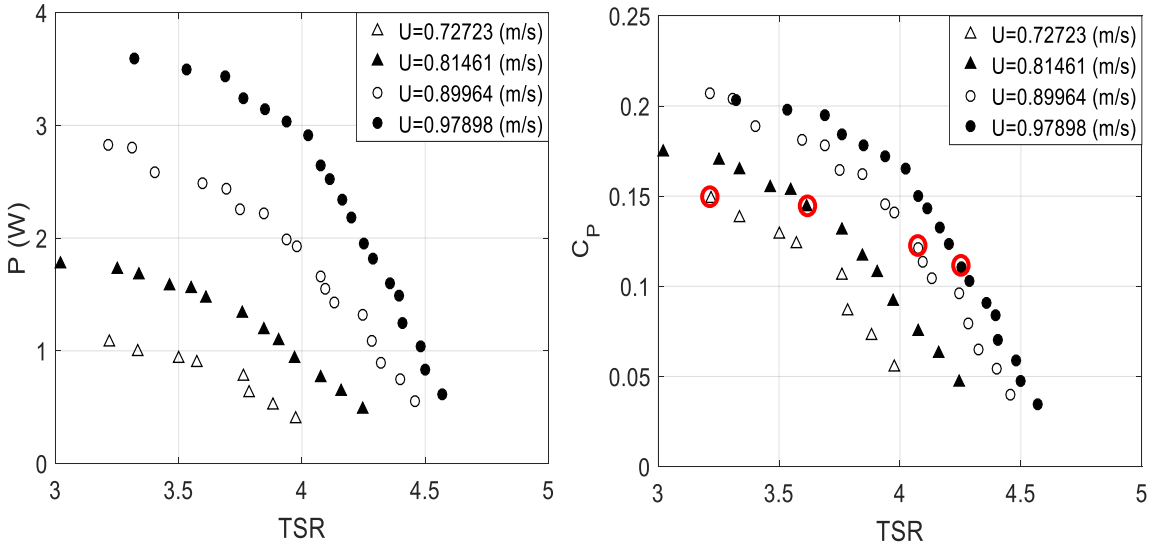

Figure 12. (a) *P* and (b) C_P vs. *TSR* for 3-blade single-turbine exposed to different velocities

4.2. MULTI-TURBINE SYSTEM PERFORMANCE EVALUATION

The number of blades that can be added to a rotor is limited by the geometry or the high solidity. The number of blades in this study was increased by adding, coaxially, more 3-blade rotors to the turbine system shaft. The 3-blade HAHkT with untwisted blades was found to generate more power than 2-blade or 4-blade turbines that had the same solidity [3].

Two differences exist between the C_P curves for the different turbine configurations illustrated in Figures 13a and 13b:

1. The maximum reached $_{CP}$ is higher for turbine systems with larger blade number.
2. The operational *TSR* at maximum performance is lower for turbine systems with larger blade number.

Figure 13a shows that the efficiency of the multi-turbine system improved by approximately 75% (when the flow velocity is 0.9789 m/s) before the turbine came to a complete stop. The multi-turbine system has higher blade surfaces exposed to the flow which results in higher lift force thus higher power output. Similar C_P improvement was observed for the 6-blade turbine for the same reasons. The decrease in the operational *TSR* (*TSR* that yields maximum performance) for the multi-turbine system is likely attributed to the slower stream velocity through the second rotors. The second rotor is exposed to a slower flow velocity due to the wake effect. This slower flow requires slower rotational speed (smaller *TSR*) to get a larger α along the span, (see Equations 3, 7 and 10), and thus larger lift and better performance. Meanwhile, the velocity used to define the *TSR* is the unreduced velocity so the ratio $\omega R/U_\infty$ is small thus *TSR* shifted to the left. Similar decrease in the operational *TSR* was observed for the 6-blade turbine. Though, for this 6-blade rotor,

the higher blade number causes a higher flow impedance that lowers the stream velocity through its rotor [3].

A third rotor was added to the multi-turbine system and tested at a flow velocity of 0.9789 m/s. When it was compared to the turbine system with two rotors, the results showed the same behavior as in the previous comparison. The system that contained three rotors had a higher C_P peak that shifted to a lower *TSR* (see Figures 14a and 14b). Nevertheless, the resulting improvement in the performance was less for the three-rotor turbine system configuration (about 32%) than it was for the two-rotor turbine system. The multi-turbine system's rotors acted collectively to increase the extracted power. Due to that the third rotor operating under slower flow velocity than the second rotor, its contribution to the power generation was less than the second rotor.

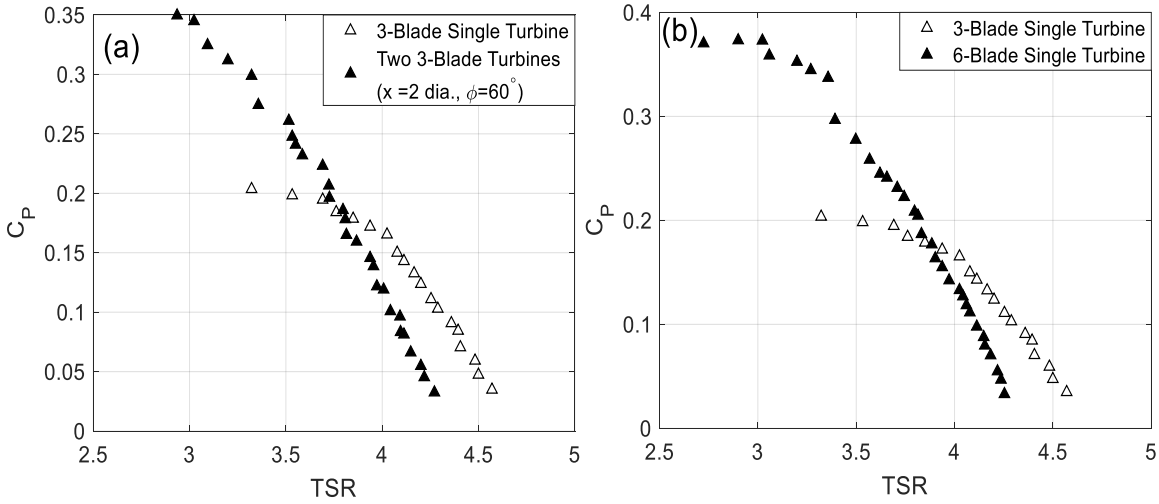

Figure 13. C_P vs. *TSR* for 3-blade single-turbine as compared to (a) two 3-blade turbine system and (b) 6-blade single-turbine

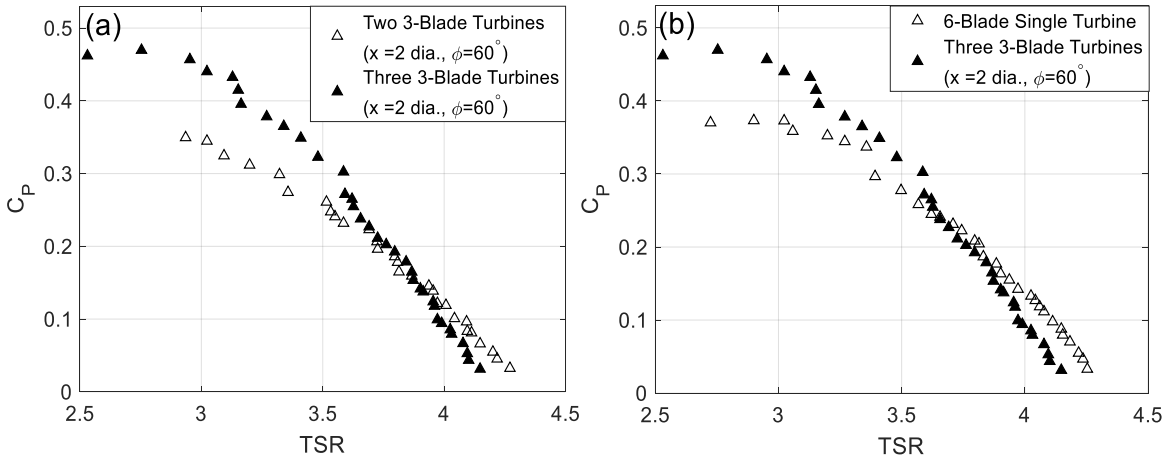

Figure 14. C_P vs. *TSR* for three 3-blade turbine system as compared to (a) two 3-blade turbine system and (b) 6-blade single-turbine

The effect of the two experimental parameters, rotors' relative installation angle, Ø, and axial distance between rotors, *x*, was investigated for better turbine system configuration (these variables are defined in Section 3.1.3). The effect of Ø when the flow speed was 0.9789 m/s is presented in Figures 15a and 15b. No obvious change occurred in the generated power curves when Ø was varied, neither when x= 2 dia. nor x= 4 dia. However, at low flow velocity when the distance between rotors was set to 2 dia., the system with Ø set to 60º was observed to generate slightly higher power than when Ø was set to 0º. This suggests more investigation is required to examine the effect of Ø when the distance between the rotors is smaller than 2 dia.

The effect of changing the distance between the rotors, when the flow speed was 0.9789 m/s, was also examined (Figure 16). The gathered results suggest that the power output improved as the axial distance between rotors increased. An improvement in C_P for the system with an axial distance of 4 dia. was observed to be around 11% relative to the other system configuration (*x*= 2 dia.). This improvement occurred because the axial

velocity deficit inside the wake created by the frontal rotor decreased as the flow traveled further downstream as we can see in the wake structure discussion in Section 4.4.

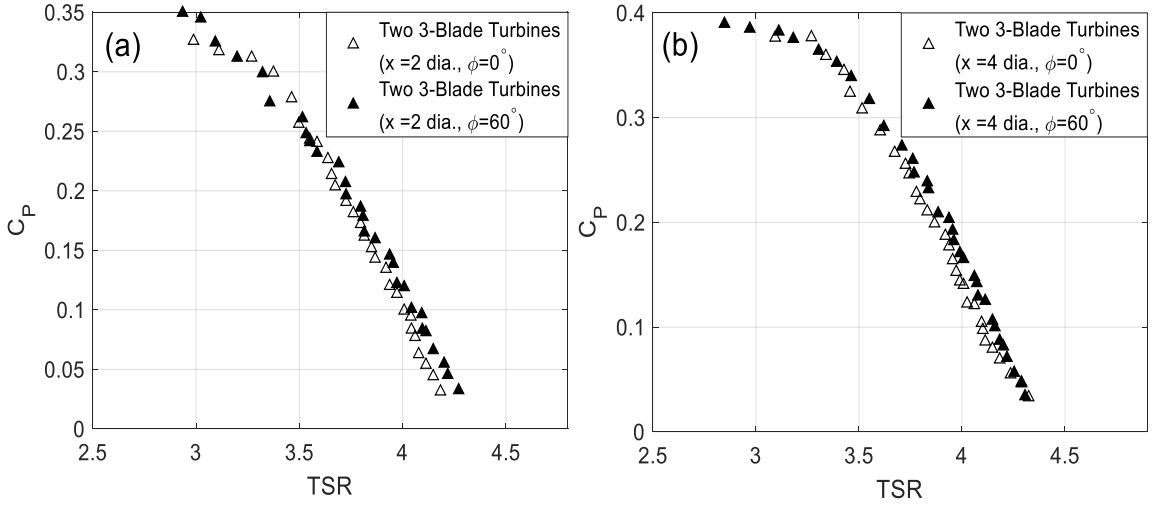

Figure 15. The effect of rotor's relative installation angle on the multi-turbine system performance

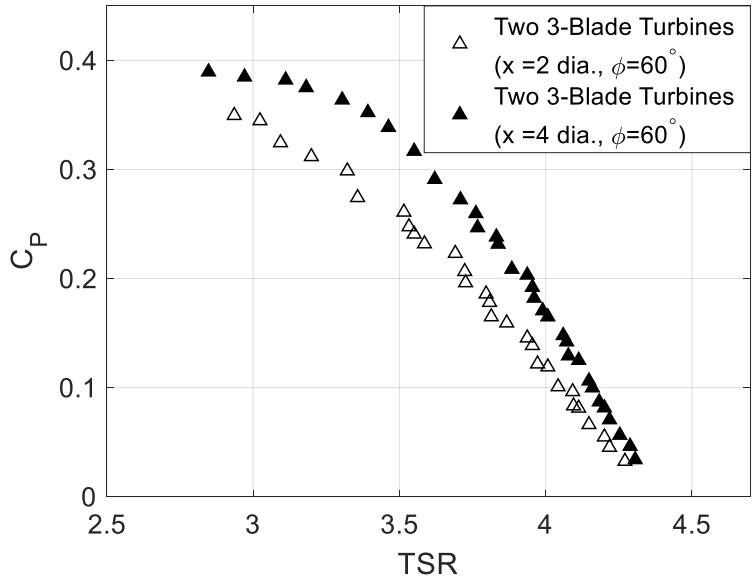

Figure 16. The effect of the distance between rotors, x, on the multi-turbine system performance

4.3. TURBINE SYSTEMS WITH DUCT REDUCER

A duct placed around a rotor significantly enhances the rotor's flow rate as water passes through its swept area. Therefore, the extracted power by a ducted turbine system is also higher than that extracted by a bare turbine [8, 33]. Two design factors can be added to the existing duct reducer to improve its performance: an outlet diffuser and a flange around the exit. Though, these two design factors were not applied because the water tunnel's size was limited.

Figure 17 shows the effect of duct reducer on the performance of a single-rotor and two-rotor turbine systems. The ducted turbine's output power is increased due to the increased flow velocity passes through the rotor. A comparison between ducted and bare single-rotor turbine indicates that the maximum C_P was improved by 311% for the velocity of 0.7272 m/s (Figure 17a). The ducted multi-turbine system's performance at this flow velocity was about 6 times the bare single-turbine. In Figure 17b, the ducted multi-turbine system, at the same flow velocity of 0.7272 m/s, shows improvement by approximately 250% compared to when it is bare. The ducted system's power curves were observed to shift significantly to higher *TSR*s. It can be inferred that the C_P peak of the ducted turbines occurred at a higher *TSR* as well. The velocity around the ducted rotor is high which means the optimum angle of attack requires the turbine to rotate at a fast angular velocity. This high rotational speed may eliminate the low-speed gearbox, which is one of the most expensive parts of a turbine system [41]. It should be noted that all ducted multi-turbine system results were presented at a relatively slower flow speed (0.7272 m/s). The reason was that, at higher flow speeds, the ducted multi-turbine system power curves were stopped early because of the clutch reached its maximum torque capacity (0.226 N.m) Therefore,

to provide meaningful comparison between the ducted and unducted turbine systems, the results were only considered at a flow speed of 0.7272 m/s. In general, the behavior of the results at different flow speeds was the same.

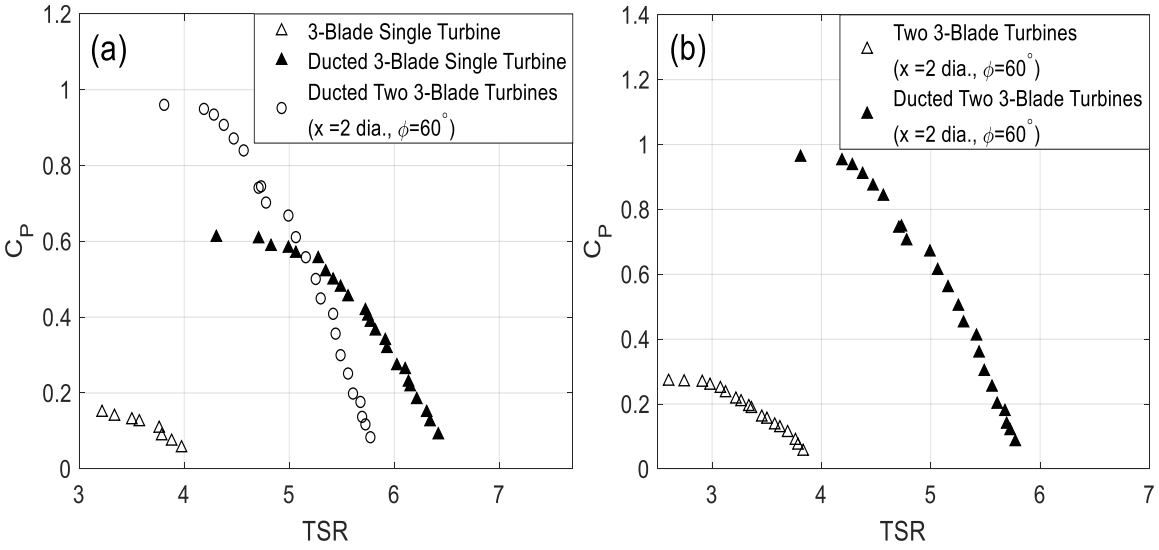

Figure 17. Duct effect on single- and two-rotor turbine systems

4.4. WAKE INVESTIGATION

Five hundred optical images of instantaneous 2D velocity measurements of the flow were acquired for each PIV visualization test. The captured images were processed using Insight 4G software and then imported to Tecplot 360 software. The Tecplot 360 calculated the average flow speed of every test for analysis. Figure 18 illustrates wake decay and expansion. In general, the wake's width increased slightly and the axial velocity deficit decreased as the flow traveled downstream. A comparison between the two rotors in Figure 18 reveals that the velocity deficit behind the 6-blade turbine (solidity, $\sigma = 0.147$) is higher

than it is behind the 3-blade turbine (solidity, $\sigma = 0.0735$). This indicates that the higher solidity 6-blade turbine captured more kinetic energy than the low solidity 3-blade turbine. Another observation is that the ratio U/U_∞ below the 6-blade rotor is higher than that of the 3-blade rotor. This means there is higher flow impedance at the higher solidity rotor. This higher flow (higher U/U_∞) under the higher solidity rotor is to compensate for the slower flow through this rotor and thus satisfies the conservation of mass at the rotor plane.

The highest axial velocity deficit was always located at the wake's center. Therefore, the axial wake centerline velocity deficit trend was investigated for both 3-blade and 6-blade turbines along a path length of 4 dia. The rate of recovery for the axial velocity through regions within 2 dia. behind the rotors was relatively small (see Figure 19). However, regions beyond two rotor diameter exhibited a relatively higher rate of recovery in the axial velocity profile. This dissipation in the velocity deficit was driven by the turbulent intensity in the ambient flow. Overall, the velocity deficit produced by a 6-blade turbine had a faster rate of recovery than the 3-blade turbine. However, the 6-blade curve exhibited a trend of gradual decrease in the slope toward 4 dia. Thus, further downstream locations need to be investigated.

If rotors with optimized solidity are integrated into the multi-turbine system, the second rotor should be placed at a downstream region where the flow experiences a faster rate of recovery so a higher performance is achieved.

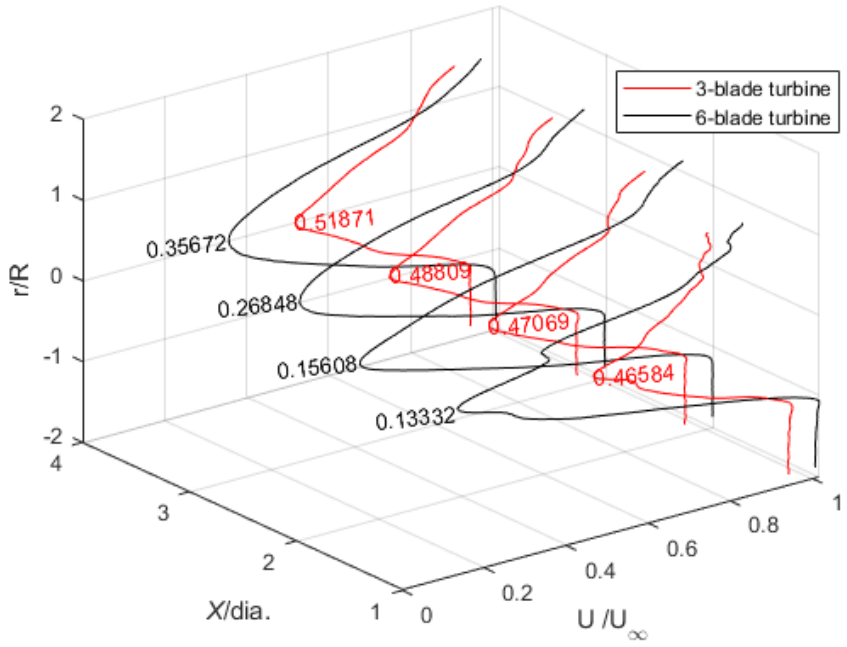

Figure 18. Axial velocity profile for both 3- and 6-blade turbines at different axial locations

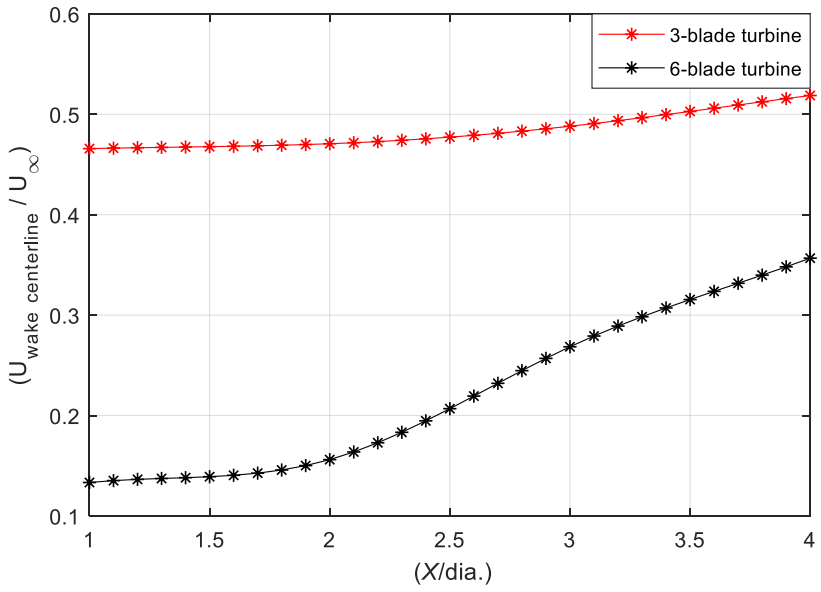

Figure 19. Centerline axial velocity deficit at different axial locations for both 3- and 6-blade turbines

5. CONCLUSION

A 3-blade horizontal axis composite turbine with Eppler 395 hydrofoil was manufactured using OOA technique and tested in a water tunnel. The generated power was found to increase when the pitch angle decreased. The optimum pitch angle for the Eppler 395 hydrofoil was found to be approximately 5º. The generated power decreased due to the stall effect when the pitch angle was lowered to 2º. The power curve peak shifted toward lower *TSR* and had a lower magnitude when the pitch angle increased. C_P increased for all pitch angles as the *TSR* decreased because α increased along the blade span.

Sets of two and three rotors were integrated into a multi-turbine system. The multi-turbine system performance improved as the number of rotors increased. This enhancement in the performance was accompanied by the lowering of the operational *TSR* due to the slower flow passing through the latter rotors. Due to the wake effect, the third rotor had less contribution to improving the performance compared to the second rotor. The turbine system configuration was also examined, and the results showed that the power output generated by the multi-turbine system improved as the axial distance between the rotors increased due to the wake recovery, whereas rotors' relative installation angles had an insignificant effect on the turbine system performance.

In the wake investigation, the velocity deficit behind the 6-blade turbine was higher than that behind the 3-blade turbine which indicates a higher kinetic energy absorption by the higher solidity 6-blade rotor. The velocity deficit resulted from the 6-blade turbine shows a faster rate of recovery compared to the 3-blade turbine but, the rate of recovery decreased toward the 4 dia. Therefore, in order for a high-solidity multi-turbine system to

operate with higher efficiency, the second rotor should be located in the downstream region where the flow has high rate of recovery.

REFERENCES

[1] A. Bahaj and L. Myers, "Fundamentals applicable to the utilisation of marine current turbines for energy production," *Renewable Energy,* vol. 28, no. 14, pp. 2205-2211, 2003.

[2] P. Jacobson, T. Ravens, K. Cunningham, and G. Scott, "Assessment and mapping of the riverine hydrokinetic resource in the continental United States," Electric Power Research Institute, Palo Alto, CA. 2012, Available: https://www.osti.gov/servlets/purl/1092058.

[3] S. Subhra Mukherji, N. Kolekar, A. Banerjee, and R. Mishra, "Numerical investigation and evaluation of optimum hydrodynamic performance of a horizontal axis hydrokinetic turbine," *Journal of Renewable and Sustainable Energy,* vol. 3, no. 6, pp. 1-18, 2011.

[4] W. M. J. Batten, A. S. Bahaj, A. F. Molland, and J. R. Chaplin, "Experimentally validated numerical method for the hydrodynamic design of horizontal axis tidal turbines," *Ocean Engineering,* vol. 34, no. 7, pp. 1013-1020, 2007.

[5] Z. N. Ashrafi, M. Ghaderi, and A. Sedaghat, "Parametric study on off-design aerodynamic performance of a horizontal axis wind turbine blade and proposed pitch control," *Energy Conversion and Management,* vol. 93, pp. 349-356, 2015.

[6] M. M. Duquette and K. D. Visser, "Numerical implications of solidity and blade number on rotor performance of horizontal-axis wind turbines," *Journal of Solar Energy Engineering,* vol. 125, no. 4, pp. 425-432, 2003.

[7] B. Gilbert and K. Foreman, "Experiments with a diffuser-augmented model wind turbine," *Journal of Energy Resources Technology,* vol. 105, no. 1, pp. 46-53, 1983.

[8] A. Nasution and D. W. Purwanto, "Optimized curvature interior profile for Diffuser Augmented Wind Turbine (DAWT) to increase its energy-conversion performance," *2011 IEEE First Conference on Clean Energy and Technology,* pp. 315-320, 2011.

[9] T. S. Kannan, S. A. Mutasher, and Y. K. Lau, "Design and flow velocity simulation of diffuser augmented wind turbine using CFD," *Journal of Engineering Science and Technology,* vol. 8, no. 4, pp. 372-384, 2013.

[10] B. Elie, G. Oger, P.-E. Guillerm, and B. Alessandrini, "Simulation of horizontal axis tidal turbine wakes using a Weakly-Compressible Cartesian Hydrodynamic solver with local mesh refinement," *Renewable Energy,* vol. 108, pp. 336-354, 2017.

[11] R. J. Stevens, L. A. Martínez-Tossas, and C. Meneveau, "Comparison of wind farm large eddy simulations using actuator disk and actuator line models with wind tunnel experiments," *Renewable Energy,* vol. 116, pp. 470-478, 2018.

[12] P.-Å. Krogstad, L. Sætran, and M. S. Adaramola, "“Blind Test 3” calculations of the performance and wake development behind two in-line and offset model wind turbines," *Journal of Fluids and Structures,* vol. 52, pp. 65-80, 2015.

[13] M. Calaf, C. Meneveau, and J. Meyers, "Large eddy simulation study of fully developed wind-turbine array boundary layers," *Physics of fluids,* vol. 22, no. 1, pp. 015110 (1-16), 2010.

[14] M. C. Rector, K. D. Visser, and C. Humiston, "Solidity, blade number, and pitch angle effects on a one kilowatt HAWT," presented at the 44th AIAA Aerospace Sciences Meeting and Exhibit, Reno, NV, January 09 -12, 2006.

[15] D. M. Grogan, S. B. Leen, C. Kennedy, and C. Ó. Brádaigh, "Design of composite tidal turbine blades," *Renewable energy,* vol. 57, pp. 151-162, 2013.

[16] P. Brøndsted, H. Lilholt, and A. Lystrup, "Composite materials for wind power turbine blades," *Annu. Rev. Mater. Res.,* vol. 35, pp. 505-538, 2005.

[17] A. Boisseau, P. Davies, and F. Thiebaud, "Sea water ageing of composites for ocean energy conversion systems: influence of glass fibre type on static behaviour," *Applied Composite Materials,* vol. 19, no. 3-4, pp. 459-473, 2012.

[18] M. S. Guney, "Evaluation and measures to increase performance coefficient of hydrokinetic turbines," *Renewable and Sustainable Energy Reviews,* vol. 15, no. 8, pp. 3669-3675, 2011.

[19] M. O. Hansen, *Aerodynamics of wind turbines*. Routledge, 2013.

[20] A. Ning, G. Hayman, R. Damiani, and J. M. Jonkman, "Development and validation of a new blade element momentum skewed-wake model within AeroDyn," *33rd Wind Energy Symposium,* pp. 5-9, 2015.

[21] P. J. Moriarty and A. C. Hansen, *AeroDyn theory manual*. National Renewable Energy Laboratory Golden, Colorado, USA, 2005.

[22] M. L. Buhl, *A new empirical relationship between thrust coefficient and induction factor for the turbulent windmill state*. National Renewable Energy Laboratory Golden, Colorado, USA, 2005.

[23] M. Drela, "XFOIL: An analysis and design system for low Reynolds number airfoils," in *Low Reynolds number aerodynamics*: Springer, 1989, pp. 1-12.

[24] M. Rahimian, J. Walker, and I. Penesis, "Performance of a horizontal axis marine current turbine–A comprehensive evaluation using experimental, numerical, and theoretical approaches," *Energy,* vol. 148, pp. 965-976, 2018.

[25] F. N. Coton, T. Wang, and R. A. M. Galbraith, "An examination of key aerodynamic modeling issues raised by the NREL blind comparison," *ASME 2002 Wind Energy Symposium,* pp. 168-178, 2002.

[26] Z. Du and M. S. Selig, "A 3-D stall-delay model for horizontal axis wind turbine performance prediction," *AIAA Paper,* vol. 21, pp. AIAA-98-0021(1-19), 1998.

[27] A. Eggers, K. Chaney, and R. Digumarthi, "An assessment of approximate modeling of aerodynamic loads on the UAE rotor," *ASME 2003 Wind Energy Symposium*, pp. 283-292, 2003.

[28] A. Abutunis, R. Hussein, and K. Chandrashekhara, "A neural network approach to enhance blade element momentum theory performance for horizontal axis hydrokinetic turbine application," *Renewable Energy*, (2018), https://doi.org/10.1016/j.renene.2018.09.105.

[29] J. Whelan, J. Graham, and J. Peiro, "A free-surface and blockage correction for tidal turbines," *Journal of Fluid Mechanics,* vol. 624, pp. 281-291, 2009.

[30] C. Thumthae and T. Chitsomboon, "Optimal angle of attack for untwisted blade wind turbine," *Renewable Energy,* vol. 34, no. 5, pp. 1279-1284, 2009.

[31] M.-H. Lee, Y. Shiah, and C.-J. Bai, "Experiments and numerical simulations of the rotor-blade performance for a small-scale horizontal axis wind turbine," *Journal of Wind Engineering and Industrial Aerodynamics,* vol. 149, pp. 17-29, 2016.

[32] H. Li, G. A. Taylor, A. M. Abutunis, K. Chandrashekhara, A. R. Kashyap, and J. W. Kimball, "Design and performance evaluation of a hydrokinetic composite turbine system," presented at the SAMPE, Long Beach, CA, 2013.

[33] F. Ponta and P. Jacovkis, "Marine-current power generation by diffuser-augmented floating hydro-turbines," *Renewable Energy,* vol. 33, no. 4, pp. 665-673, 2008.

[34] P. Aghsaee and C. D. Markfort, "Effects of flow depth variations on the wake recovery behind a horizontal-axis hydrokinetic in-stream turbine," *Renewable Energy,* vol. 125, pp. 620-629, 2018.

[35] J. Yan, X. Deng, A. Korobenko, and Y. Bazilevs, "Free-surface flow modeling and simulation of horizontal-axis tidal-stream turbines," *Computers & Fluids,* vol. 158, pp. 157-166, 2017.

[36] G. I. Comyn, D. S. Nobes, and B. A. Fleck, "Performance Evaluation and Wake Study of a Micro Wind Turbine," *Transactions of the Canadian Society for Mechanical Engineering,* vol. 35, no. 1, pp. 101-117, 2011.

[37] C. Garrett and P. Cummins, "The efficiency of a turbine in a tidal channel," *Journal of Fluid Mechanics,* vol. 588, pp. 243-251, 2007.

[38] T. Kinsey and G. Dumas, "Impact of channel blockage on the performance of axial and cross-flow hydrokinetic turbines," *Renewable Energy,* vol. 103, pp. 239-254, 2017.

[39] I. Herráez, B. Stoevesandt, and J. Peinke, "Insight into rotational effects on a wind turbine blade using Navier–Stokes computations," *Energies,* vol. 7, no. 10, pp. 6798-6822, 2014.

[40] S. Guntur and N. N. Sørensen, "A study on rotational augmentation using CFD analysis of flow in the inboard region of the MEXICO rotor blades," *Wind Energy,* vol. 18, no. 4, pp. 745-756, 2015.

[41] F. Ponta and G. Shankar Dutt, "An improved vertical-axis water-current turbine incorporating a channelling device," *Renewable Energy,* vol. 20, no. 2, pp. 223-241, 2000.

III. EXPERIMENTAL EVALUATION OF COAXIAL HORIZONTAL AXIS HYDROKINETIC COMPOSITE TURBINE SYSTEM

Abutunis, A., Fal, M., Fashanu, O., Duan, L., and Chandrashekhara, K.

Department of Mechanical and Aerospace Engineering

Missouri University of Science and Technology, Rolla, MO 65409

ABSTRACT

Hydrokinetic turbines extract energy from free-flowing water, such as river streams and marine currents. For river applications, the typical deployment location is highly space-constrained due to both the nature of the river (i.e., its natural width and depth) and the other usages of the river (e.g., transportation and fishing). Therefore, a modified design of a conversion device is desired to accommodate these space limitations. The objective of this work is to derive optimum design criteria for a coaxial horizontal axis hydrokinetic turbine (HAHkT) system utilizing both numerical and experimental approaches. Single-turbine systems configured with different blade sizes were numerically studied to obtain the optimum solidity. Furthermore, the blockage effects on the various-solidity rotors were examined. The numerical modeling was extended to analyze the performance of the coaxial multi-turbine system (equipped with optimum-solidity rotors) and characterize its ambient flow. The rotor with optimum solidity was manufactured and integrated into both the single-turbine and multi-turbine systems for performance evaluation and numerical validation. A particle image velocimetry (PIV) system was utilized to evaluate the wake structure and validate the numerical results of the flow characteristics. The performance of

the single-turbine system with an optimum-solidity of 0.22248 was twice that of the single-turbine with the smallest solidity of 0.07342. The optimum-solidity multi-turbine system further improved the performance by 47% when compared to the optimum-solidity single-turbine system. Increasing the number of rotors form three to five, slightly enhanced efficiency by about 4%.

Keywords: hydrokinetic turbine, multi-turbine system, computational fluid dynamics, solidity, blockage, particle image velocimetry, wake structure

1. INTRODUCTION

Horizontal axis hydrokinetic turbines (HAHkTs) are integrated turbine-generators for electricity generation from free streams. The HAHkT is similar to a wind turbine; they both comprise a rotor (multiple blades connected to a hub) mounted on a shaft, a generator, and a power conversion system that incorporates control features. As in a wind turbine, flow conditions must be managed and power extraction must be maximized either by varying the rotational speed or the pitch angle according to the incoming flow. The size of a HAHkT is smaller than a wind turbine due to the limited available operational space and other design concerns such as the high loading. Nonetheless, the size constraint for HAHkTs is mitigated by the much higher power density (kinetic energy) of flowing water, even at lower speeds than in wind. Unlike wind turbines, the flow of water toward the hydrokinetic turbines can be assumed unidirectional due to the more certain flow direction of the river streams and marine currents.

Several parameters can affect the performance of HAHkTs. These parameters are the flow velocity (U), pitch angle (θ), angle of attack (α), tip speed ration (TSR), solidity (σ), blade number (N), and rotor swept area (A). The main and interaction effects of these parameters all play a role in the design of the hydrokinetic turbines. Solidity, which was one of the design parameters considered in this study, can critically influence the performance of HAHkTs. Horizontal axis turbine efficiency augments as its rotor solidity goes higher. However, if the solidity increased beyond its optimum value, the performance of the turbine starts to decline due to the high flow impediment [1-5]. Moreover, a very high rotor solidity with increased chord length (c) requires a stronger blade structure to withstand the large thrust force exerted by the incoming water flow on the blade surface. Increasing the swept area (rotor diameter) also has a favorable influence on the generated power, but it is limited by the stream depth and the induced bending moment.

Numerous studies were conducted to better understand the aero/hydrodynamic of axial turbines for the sake of improving their efficiency. Madrigal et al. [4] utilized the shear-stress transport (SST) k–ω turbulence model with a moving reference frame technique to study the solidity effect on the performance of an axial water turbine operated at lower flow conditions than it was designed for. The solidity was controlled by altering the number of blades, though the number of blades has its own effect regardless of solidity variation [2, 3]. They suggested that the power coefficient (C_P) at the peak (notated as C_{P_peak}) increased by 2% for each added blade. Nevertheless, the increase in blade number (N) above the considered reference N was deemed worthless due to the very small efficiency enhancement. Moreover, the operational TSR range shrunk and the peak occurred at lower rotational speed as N increased. Morris et al. [5] also investigated the

effect of solidity on tidal turbine performance. He utilized both SST k–ω and Reynolds Stress Model (RSM) turbulence models in his study. Similar to [4], C_{P_peak} increased and shifted to lower *TSR* as solidity increased. The difference in CPs obtained by both models was found to be of little significance and had the same trend. In the current study, an effort was made to mitigate the constraints on the rotor solidity and rotor diameter through a numerical and experimental investigation of a multistage device for river and other low head and limited-space streams applications.

The interaction between turbines that operate within the same stream (i.e., a wind farm) has an essential effect on these turbines' efficiencies. Similarly, the performance of the downstream rotors in the suggested multi-turbine system is affected by the upstream rotor's wake. The study of the wake and wake-interaction is important for improving the overall performance of turbines operating interactively within the same site. Several researchers used experimental and numerical approaches (commonly, large eddy simulation) to study wake and wake-interaction and observed their effect on the turbines' efficiency [6-11]. Stergiannis et al. [10] used k–ω and k–ε turbulence models to simulate the wake of two wind turbines in an array and compared the results against a simplified actuator disk model (ADM). They incorporated a multiple reference frame approach to account for the rotational effects. They validated the numerical results of the upstream rotor wake with experimental measurements. The measurements showed better agreement with the turbulence models while the ADM underestimated the velocity deficit inside the wake. The k–ω model was found to have the least errors [10]. To reduce the grid size in the study of wake in a large wind farm, Stevens et al. [7] compared the performance of ADM and an actuator line model (ALM) in relatively coarse large eddy simulations (LES). The ALM

was found to have better performance than ADM within near wake region (up to 3 diameters) behind a single rotor. They also proposed that considering the nacelle and tower in the simulation improved the wake prediction, especially at the centerline. For the wind farm case, the ADM was more accurate even farther downstream when validated against experimental results. They concluded that ADM could be an appropriate technique when simulating a large wind farm using LES.

The presence of a turbine in a confined environment, such as the water tunnel, causes a partial blockage which alters the turbine performance. The effect of the blockage causes an augmentation of the flow speed around and through the rotor which enhances its efficiency [12, 13]. The reason is that the wake expansion behind the confined rotor is bounded by the surrounding effects such as bed, lateral walls, free surface (for water turbines), or turbulence generated by neighboring turbines [14, 15]. This raises the dynamic pressure at the rotor plane which in turn increases the flow speed and the exerted forces when compared to the unconfined turbine case. To increase the reliability of the design of the blades and turbine system, the blockage effects should be accounted for.

Blockage correction models are common tools to correct constrained turbine performance. Usually, these models are developed based on the actuator disk model [13, 14, 16-19] that requires the inputs of the thrust coefficient and blockage ratio of the confined rotor. The blockage ratio (ε) is defined as

$$\varepsilon = \frac{A}{A_T} \tag{1}$$

where A is the rotor swept area and A_T is the cross-sectional area of the flow domain (e.g., water tunnel). While these blockage correction models do not explicitly take into account

the solidity of the turbine, the implemented thrust coefficient does (thrust is proportional to solidity).

The hydrodynamic performance of single and multiple coaxial HAHkT systems with different configurations was studied experimentally in the authors' previous work. The study also investigated the flow behavior behind a single-rotor turbine system with a different number of blades [20]. The previous study was limited by the water tunnel test section size. The current work objective was to optimize the efficiency of the proposed multi-turbine system through the following: (a) investigation of the solidity, blockage, and their interactive effects, (b) further alteration of the system configuration, and (c) investigation of flow characteristics at the vicinity and downstream of the turbine system. The power coefficient was obtained numerically using computational fluid dynamics (CFD) and results were experimentally validated. PIV system was used to evaluate the velocity profile inside the wake under different conditions. The PIV was also used to validate the simulated flow.

2. COAXIAL MULTI-TURBINE SYSTEM

2.1. PROSPECTIVE IMPACT

A conventional hydrokinetic energy conversion system (HECS) consists of a metallic rotor and shaft, a generator, and a power conversion system. The overall efficiency of this system is hindered by several design parameters and material availability. The proposed system integrates multiple coaxial HAHkTs with composite blades. The composite blades are light, corrosion-resistant, and can operate under high flow speeds

with less bending [21]. More details about the design and manufacturing technique of the used composite blades were reported in the author's previous work [20]. The number of composite blades per each rotor was three. The HAHkT with an untwisted three-blade rotor was reported to provide higher energy than turbines with either two- or four-blades with the same solidity. The decline in efficiency for rotors with more than four blades was attributed to the increased blockage at a specific rotational speed [3]. The rotors of the suggested system are adequately spaced allowing sufficient flow recovery and thus efficient energy harvesting. The major benefit of this system is the increase in power output whilst rotor solidity and radius are kept moderate (extreme solidity causes high flow impediment and extensive blade loading). Another key advantage of the coaxial HAHkTs approach is that the increase in power requires only one large generator, rather than multiple small generators per turbine. This is expected to result in a further reduction in the installation and maintenance cost and in the electrical losses in the cables, joints, and generators. The system with multiple rotors mounted coaxially is expected to allow efficient power generation in streams with limited operational space.

2.2. SYSTEM CONFIGURATIONS

The multi-turbine system was arranged to have either three or five rotors attached to the same horizontal shaft. The rotors' blades were pitched to 20º to decrease the thrust loading (optimum pitching was found around 5o [20]. The axial distance between the rotors, x, was varied to 2 diameters (dia.) and 4 dia. The rotors' relative installation angle (the azimuth angle difference), ϕ, was fixed to 60º (ϕ has an insignificant effect on the turbine system performance [20]). Figure 1 demonstrates these two parameters.

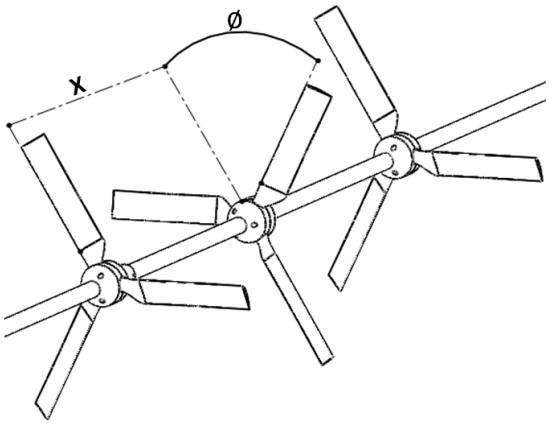

Figure 1. The multi-turbine system with axial distance and relative installation angle

3. HYDROKINETIC TURBINE PRINCIPLE TERMINOLOGY

A hydrokinetic turbine's performance is characterized by its power or power coefficient. Hydrokinetic turbines inherently exhibit a low efficiency, a primary obstacle to commercializing this technology [22]. Enhancing a HAHkT's performance requires an understanding of various interrelated design parameters, such as solidity, number of blades, tip speed ratio, rotational speed, pitch angle, and angle of attack. Moreover, a HAHkT's performance is affected by the flow characteristics, such as incident flow stream (free-stream velocity average) and free-stream turbulence. Important design parameters are presented and discussed in this section.

The power (P) generated by a turbine is calculated by multiplying the generated moment by the rotor angular velocity

$$P = M\Omega \tag{2}$$

where M is the turbine moment magnitude (N.m) and Ω is the turbine rotational speed (rad/sec). The power coefficient (C_P) is used to indicate the turbine's efficiency. It resulted

from non-dimensionalizing the power with respect to the available kinetic energy in the flowing water that passes the turbine swept area. It is given by

$$C_P = \frac{P}{\frac{1}{2}\rho U^3 A} \tag{3}$$

where ρ is the water density (kg/m^3). Similar to C_P, the thrust coefficient (C_T) is obtained by non-dimensionalizing the thrust force (T) with respect to the dynamic pressure exerted on the rotor's swept area and is defined as

$$C_T = \frac{T}{\frac{1}{2}\rho U^2 A} \tag{4}$$

The tip speed ratio (*TSR*) is used to control the turbine's performance. *TSR* is defined as the ratio of the blade's tip tangential speed (ΩR) to the incoming flow velocity and is given by

$$TSR = \frac{\Omega R}{U} \tag{5}$$

where R is the rotor radius. Turbine solidity is another important factor considered when designing an axial turbine. It is an indicator of how much of the blades' surface area occupies the rotor swept area. Increasing the solidity results in increasing the blade lift surface but also increases the flow impedance. Thus, an optimum value should be sought to enhance turbine efficiency. The solidity is defined as the ratio of the sum of chord length for all blades to the circumference of the rotor and is given by

$$\sigma = \frac{Nc}{2\pi R} \tag{6}$$

The local pitch angle (θ_r) is the angle between a blade local chord and the turbine plane of rotation. Similar to *TSR*, controlling the pitch angle is another way to adjust generated power. The sectional angle between the local relative flow velocity (U_{r_rel}) and the local blade chord is called the local angle of attack (α_r) and is calculated as

$$\alpha_r = \emptyset_r - \theta_r \tag{7}$$

where $\emptyset_r$ is the local incoming flow angle, which represents the angle between U_{r_rel} and the plane of rotation. This local angle $\emptyset_r$ is obtained using the local axial and tangential flow velocities as shown in Equation 8. The subscript *r* signifies the radial distance from the rotor center. Figure 2 illustrates all the local aforementioned angles.

$$\emptyset_r = arctan\left(\frac{(1-a)U}{(1+a')\omega r}\right), \tag{8}$$

where a and a' are the axial and tangential factors respectively.

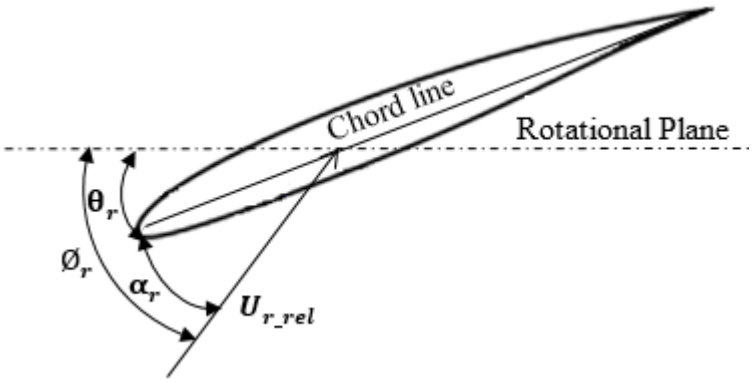

Figure 2. Local pitch angle, local angle of attack, and local incoming flow angle

4. COMPUTATIONAL FLUID DYNAMICS

The turbine system performance under different configurations was evaluated numerically. Multi-fidelity simulations were performed in this study. The multi-fidelity simulations combine (a) high-fidelity large eddy simulation (LES) used for inside-wake flow verification and (b) lower-fidelity Reynolds-averaged Navier–Stokes (RANS) used for power calculation, solidity and blockage effect investigation, and flow field examination. Experiments utilizing power measurement setup and PIV system were used in the water tunnel environment to validate the simulation results.

4.1. TURBULENCE MODELING

4.1.1. Shear-stress Transport k–ω Mode. For the turbine's performance evaluation, the SST k–ω turbulence model developed by Menter [23] was used to solve the RANS equations. The SST k–ω model is widely used for simulating the wind and water turbines due to its capability of coping with an adverse pressure gradient and separated flow [3, 24-27]. This allows the model to accurately predict the stall characteristics, which dominate the upper side of the blades when the rotor operates at optimum operational conditions [25]. The ability of a turbulence model that incorporates the eddy viscosity approach to predict the flow separation caused by a strong adverse pressure gradient is determined by the level of eddy viscosity in the wake [23]. Maintaining the proportionality between the principal turbulent shear stress and turbulent kinetic energy is essential to control the eddy viscosity level inside the wake region of the boundary layer (BL) in adverse pressure gradient flows [23, 28]. Due to the deficiency of the two-equation models

inaccurately predicting the pressure-induced separation, the eddy-viscosity formulation was modified in the SST k–ω model to account for the effect of transport of the principal turbulent shear stress. The SST k–ω model utilizes the k–ω model in the near wall region of the BL. Due to the k–ω model's strong sensitivity to the model's freestream values, a modified k–ε model is applied in the outer and far field regions [3, 23]. To trigger the appropriate model in the different regions, a blending function (F_1) was incorporated [23]. The governing equations for SST k–ω model are given by

$$\frac{\partial}{\partial t}(\rho \mathrm{k}) + \nabla \cdot \left(\rho \mathrm{k}\vec{U}\right) = \tau_{ij}\nabla\vec{U} - \beta^{*}\rho\omega\mathrm{k} + \nabla \cdot [(\mu + \sigma_k\mu_t)\nabla \mathrm{k}], \tag{9}$$

$$\begin{aligned}\frac{\partial}{\partial t}(\rho\omega) + \nabla \cdot \left(\rho\omega\vec{U}\right) = \frac{\gamma}{\nu_t}\tau_{ij}\nabla\vec{U} - \beta\rho\omega^2 + \nabla \cdot [(\mu + \sigma_\omega\mu_t)\nabla\omega] \\ +2(1 - F_1)\rho\sigma_{\omega 2}\frac{1}{\omega}\nabla k\nabla\omega,\end{aligned} \tag{10}$$

where μ is the dynamic viscosity, μ_t is the turbulent eddy viscosity, k is the turbulence kinetic energy, ω is the specific dissipation rate, and β^{*}, σ_k, σ_ω, γ, are the model's constants. τ_{ij} is Reynolds-stress tensor and is given by

$$\tau_{ij} = \mu_t\left(2\delta_{ij} - \frac{2}{3}\frac{\partial u_k}{\partial x_k}\,\delta_{ij}\right) - \frac{2}{3}\rho k\delta_{ij}, \tag{11}$$

where δ_{ij} is the mean strain-rate tensor. The model's constants and other variables definitions are given in the original work [23] and are not redefined for the sake of brevity.

4.1.2. Moving Reference Frame. For an application involving moving parts, such as blades of wind or water turbines, the flow becomes unsteady when seen from an inertial (stationary) reference frame. Moreover, the flow in the span-wise and chord-wise directions starts to accelerate under the effects of centrifugal and Coriolis forces,

respectively. Consequentially, the stall mechanism is altered [29, 30]. Considering these rotational effects along with the turbulent flow, the numerical modeling of HAHkTs becomes complicated, and solving the turbulent model's governing equations in a stationary frame of motion needs high computational requirements [3, 31]. Using a moving reference frame (MRF) approach, the flow around the rotating turbine is steady as seen by the turbine's blades, though additional terms need to be implemented to the MRF equations to account for the effects of the rotational forces [32].

For a turbine rotating at a constant speed of Ω (i.e., the frame is steadily rotating) and facing a steady incoming flow, the equations of fluid in MRF using relative velocity formulation are given below [3, 33, 34]

$$\nabla \cdot \vec{U}_{rel} = 0 \tag{12}$$

$$\frac{\partial}{\partial t}\left(\rho \vec{U}_{rel}\right) + \nabla \cdot \left(\rho \vec{U}_{rel}\vec{U}_{rel}\right) + \rho\left(2\vec{\Omega} \times \vec{U}_{rel} + \vec{\Omega} \times \vec{\Omega} \times \vec{r}\right) = -\nabla p + \nabla \cdot \tau_r, \tag{13}$$

where U_{rel} is the relative velocity seen from MRF and is given by $U_{rel} = \vec{U} - \vec{\Omega} \times \vec{r}$. The centrifugal and Coriolis forces in the momentum equation are represented by $\rho(2\vec{\Omega} \times \vec{U}_r)$ and $\rho(\vec{\Omega} \times \vec{\Omega} \times \vec{r})$ respectively. In the right side of the momentum equation, ∇p is the pressure gradient and τ_r is the viscous stress tensor, which is given by

$$\tau_r = (\mu + \mu_t)\left[\left(\nabla \vec{U} + \nabla \vec{U}^T\right) - \frac{2}{3}\nabla \cdot \vec{U} I\right], \tag{14}$$

where I is the identity tensor.

4.2. SOLVER AND BOUNDARY CONDITIONS

The flow in this work was considered steady and incompressible. The CFD simulation was performed by solving for the conservation of mass and momentum using a structured grid finite volume methodology in the commercial software of ANSYS 18.2/Fluent. The solver was set to Absolute Velocity Formulation, Steady, 3D Planar, and Pressure-Based (for incompressible flow). Figure 3 shows the boundary conditions of a turbine operating in a water tunnel. The inlet side of the water tunnel (marked green) was given a uniform inlet velocity of 0.91135 m/s boundary condition (BC). The inlet was assigned turbulent intensity (I_{in}) of 1% (as provided by water tunnel manufacturer). The inlet was also assigned turbulence length scale (l_{in}) that was calculated based on the used chord length (c) using the empirical relationships $l_{in} = 0.07 \times c$. The tunnel outlet (marked gray) was given pressure-outlet boundary condition with relative pressure set to zero (the operation pressure for simulations was set to atmospheric pressure). I_{out} of about 0.045 was obtained at the outlet using PIV. The outlet turbulence length scale (l_{out}) was identical to I_{in}. For an operating turbine, a multiple moving reference frames model was needed. The flow in each moving cell zone of the rotor domain was solved using MRF equations, and an approximation of a steady-state solution was attained. However, for the stationary (not rotating) water tunnel domain, the MRF equations were reduced to their stationary frames [34]. To apply the MRF technique, the flow domains surrounding the blades were set to a rotational frame of motion and assigned a rotational speed similar to that of the operating rotor. The walls and bed sides (marked blue) were set to stationary walls with no-slip BC. The blades and hub were considered as moving walls with zero relative velocity with respect to the rotating surrounding domains, while given no-slip as

shear condition specification. The free-surface was defined as a moving wall BC with zero shear. Second-Order upwinding discretization schemes were selected for solving all the flow governing equations. The Coupled algorithm was selected for solving pressure and velocity in a coupled manner. Convergence criteria have been set such that the residuals for the continuity, x-momentum, y-momentum, z-momentum, k, and ω were less than 5×10^{-5}. However, the solution conversion was also approved if the moment, thrust, and the mass flow converged.

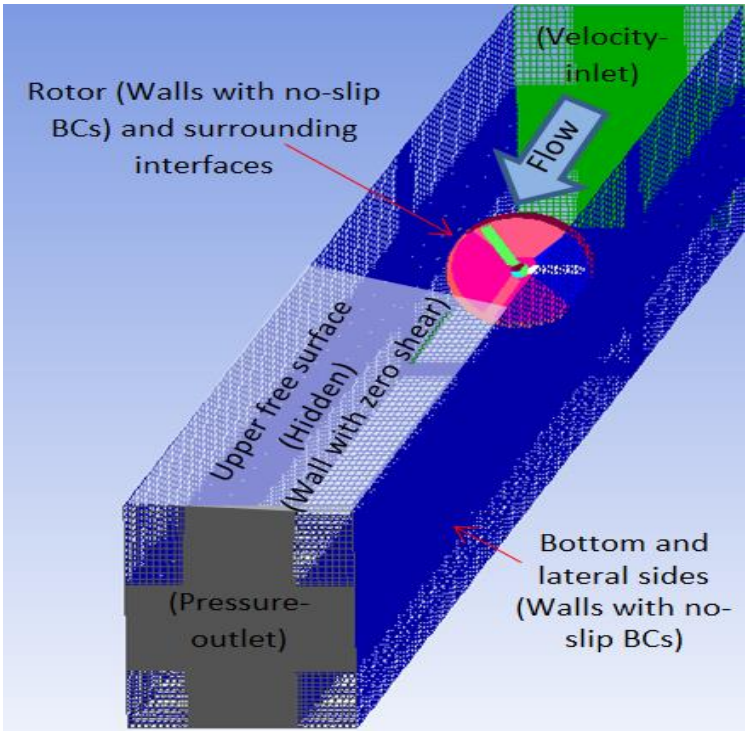

Figure 3. CFD model boundary conditions

4.3. GEOMETRY AND MESHING

The computational domain was designed to have an inner rotor domain an outer water tunnel domain. The geometry of the rotor domain was built and meshed using MATLAB and ANSYS 18.2/ICEM. Only one third of the rotor domain, which contains one blade and one third of the hub, was considered every time of meshing. The MATLAB was used to alter the hydrofoils' pitch angle, chord length, radial location, and curvature. MATLAB outputted a three-columns data matrix of all hydrofoils. The hub data was extracted from a three-dimensional (3-D) CAD model. The data coordinates, then, were imported to the ICEM to generate the hub, blade, and surrounding domain curves and surfaces (Figure 4a). Then volumes were generated utilizing a blocking technique. This technique was considered for its ease of use in generating a hexahedral mesh. Blocks edges were split to give more flexibility controlling the blocks' topology and grid density. The edges of the blocks were then associated with their corresponding geometry curves/surfaces. Associating the blocks' edges to the curved hydrofoils will allow the flow to follow the swirling streamlines (Figures 4a and 4b). The grid then was applied to the edges and hexahedral mesh was generated. The mesh was further refined in regions near the walls and towards the blade tip (more details regarding the mesh refining is discussed in Section 4.4). A meshed rotor with different scanning planes is presented in Figure 4c. A replay script, available in ICEM, was modified and utilized to accelerate the meshing process of other rotors with different solidities.

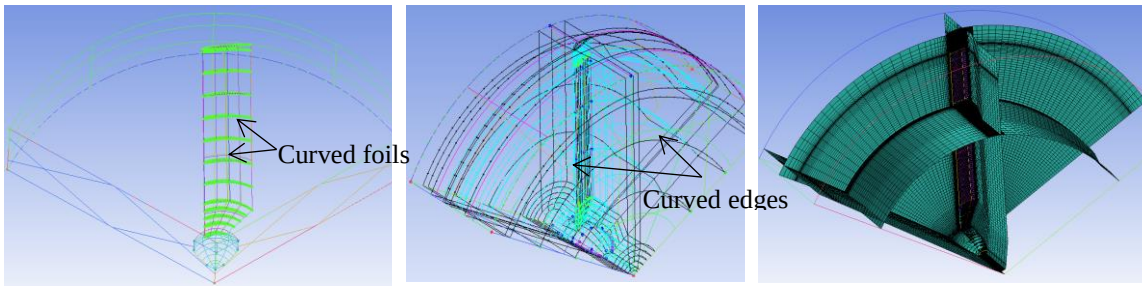

(a) (b) (c)

Figure 4. (a) One third of the rotor domain geometry, (b) the same domain was blocked for hexahedra meshing (curve edges included), and (c) the scanning planes for mesh illustration

The outer domain was meshed separately using the same blocking technique. This domain was designed to have the same water tunnel cross-sectional area but had a longer streamwise length of approximately 36 dia. The block representing the rotor domain was separated by splits and emptied to allow for later integration of the actual rotor domain. This emptied block was given the same experimental depth and lateral distances and was placed at 10 dia. from the input and 25 dia. from the output to capture both the near and far wake effects. The unstructured meshes of the three parts of the rotor domain and the water tunnel domain were combined in Fluent software. Since the whole computational domain comprised both stationary ($\Omega = 0$) and moving fluid zones, non-conformal (non-matched nodes) interfaces were generated to separate these zones. The interface allowed an easy connection between adjacent zones by passing fluxes from one mesh to another when the MRF approach was adopted. The flux characteristics were determinable because the interfaces permitted the transformation of velocity and velocity gradient. A list of geometrical and operational specifications considered in this study is given in Table 1.

Table 1. Geometrical dimensions and operational specifications

Geometry/Operation type	Description
Hydrofoil	Eppler 395
Chord length (*c*)	1.676, 2.54, 5.08, 7.62 cm (0.66, 1, 2, 3 in.)
Rotor radius *(R)*	10.902 cm (4.292 in.)
Number of blades (*N*)	3
Number of rotors (*NR*)	1, 3, 5
Distance between the rotors (*x*)	2 dia., 4 dia.
Pitch angle (θ)	20^o
Relative installation angle (ϕ)	60^o
Water tunnel cross-section	0.381 m × 0.508 m (15 in. × 20 in.)
Unconfined domain radius	0.508 m (20 in.)
Flow velocity (U)	0.91135 m/s

4.4. GRID INDEPENDENT STUDY

A grid convergence study was performed to verify that the solution is independent of mesh characteristics. The mesh size of both the rotor (c = 0.66 in.) and water tunnel domains was varied and the torque generated by the rotor was observed. For all cases used in the grid-independent study, the rotor was exposed to a flow speed of 0.91135 m/s (close to the highest water tunnel flow speed), and it was slightly loaded so the resulted rotational speed was 376 revolutions per minute (*RPM*). These operational characteristics were identical to experimental conditions. The residuals (described in Section 4.2) were, in some cases, given smaller values to allow for converged torque and thrust (i.e., the simulation was run until the torque and the thrust was converged).

4.4.1. Grid Sensitivity to the Mesh Size.

Rotor Domain: The grid size was altered along the hydrofoil while fixed to 100 grids along the blade span. The water tunnel domain was assigned approximately 6.95 million elements. The independence between the generated torque and the rotor mesh size was approved at approximately 5.55 million elements. The resulted absolute relative approximate error (ϵ_a) was about 0.233% when using the next refined (denser) rotor mesh size of 6.42 million elements. The resulted ϵ_a was about 4.417% when using the finest rotor mesh size of 12.72 million elements (see Figure 5). For this approved grid resolution, the number of grids assigned along the hydrofoil was 165. The pseudo transient time step for the rotor domain mesh study was set to 0.001 sec. The absolute relative approximate error was calculated based on the following equation

$$\epsilon_a = \left|\frac{C_{M2}-C_{M1}}{C_{M2}}\right| \times 100, \quad (15)$$

where C_{M2} is the moment coefficient produced by the rotor at a specific mesh and C_{M1} is the moment coefficient produced by the rotor at previous or at the finest mesh.

Water Tunnel Domain: The mesh size for the water tunnel domain was also changed such that the girds toward the rotor domain and at the rotor domain interface (interface in the water tunnel side) were varied. During the tunnel mesh study, the rotor mesh size was fixed to 6.42 million elements, while the pseudo transient time step was set to 0.1 sec. This time step value was approved in the time step study (see Table 4). Table 2 indicates that the water tunnel mesh size of 1.8 million elements had an absolute relative approximate error of 3.569 % with respect to the densest mesh and was the fastest to converge; therefore, it was considered.

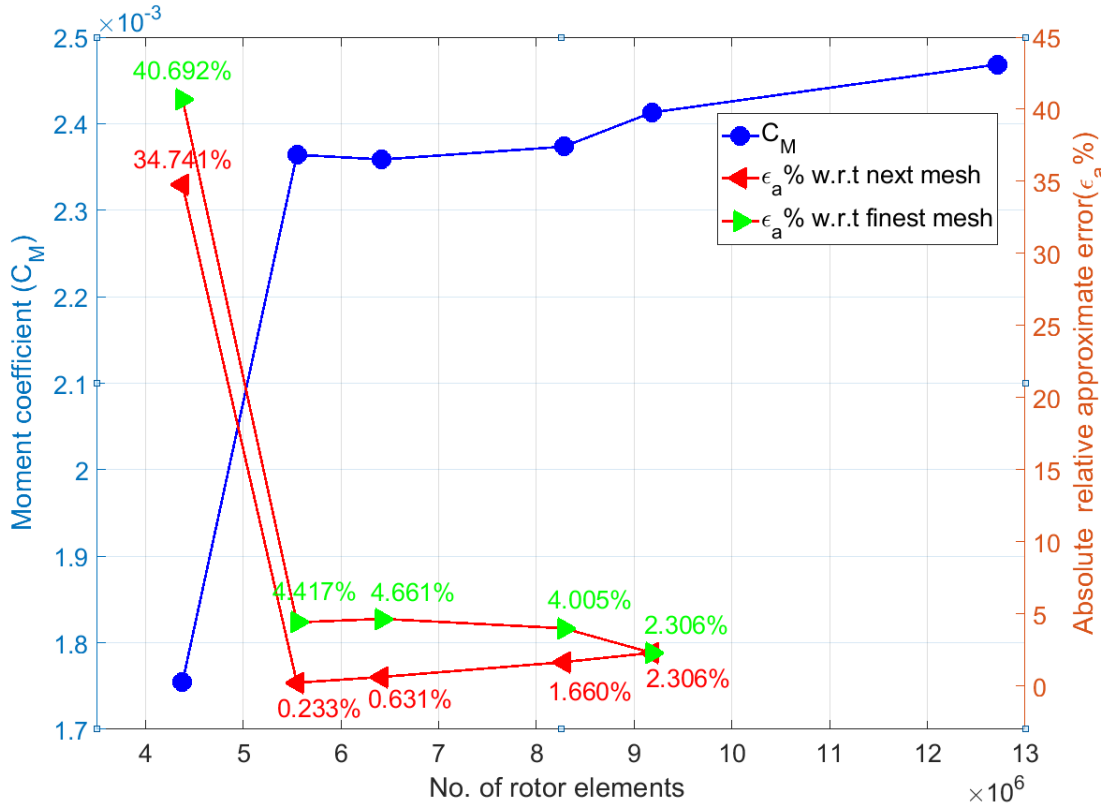

Figure 5. Rotor mesh independence study

Table 2. Water tunnel mesh independence study

Water tunnel mesh size (million)	Rotor mesh size (million)	C_M	ϵ_a w.r.t finest mesh (%)
1.8	6.42	2.299×10^{-3}	3.569
3.55		2.334×10^{-3}	2.021
6.95		2.360×10^{-3}	0.931
11.02		2.382×10^{-3}	—

4.4.2. Grid Sensitivity to the First Wall Spacing. The initial wall spacing (y') of a computational grid can affect the turbulence model accuracy [35]. This spacing needs to be small to resolve the BL on the blade surfaces. A blade element momentum (BEM) theory model with an integrated blockage correction model [18, 36] was utilized to calculate rotor flow characteristics that were used to obtain the proper grid y'. The BEM model was run at a flow velocity of 0.91135 and a pitch angle of 20º. The sectional axial and tangential velocities at three representative stations along the blade (see Table 3) were obtained at the operational *TSR* (power peak). These three sectional velocities were then inputted into a two-dimensional (2-D) SST k–ω turbulence model that solved the flow over the Eppler 395 foil. The 2-D simulation was performed in Fluent 18.2. The solver and methods were similar to those described in 3-D simulation. The assigned BCs and the meshed flow domain are shown in Figure 6. The first grid from the hydrofoil surface, y', was varied for each run until the parameter y^+ had a maximum value close to unity (listed in Table 3), which is required by most of the low-Re RANS models [37]. The parameter y^+ is an important dimensionless wall distance for a turbulent boundary layer which represents a distance from the wall normalized by the viscous length scale [38]. The approved y' at the three locations along the blade span was then used in the 3-D turbine CFD model. A linear interpolation was assumed to define the y' for other sections along the span. The maximum value of y^+ for 3-D model (the rotor with a chord of 0.66 in.) was also calculated using the SST k–ω model and was found either less than or close to unity. The y^+ values for 3-D model are reported in the last column of Table 3. The values of y^+ along the blade were fixed for both the RANS and LES and for all solidities.

Table 3. First grid distance calculated using BEM and CFD models

r/R	Tangential velocity (m/s)	Axial velocity (m/s)	y' (in.)	y^+ 2-D CFD	y^+ 3-D CFD
0.9465	2.17025	0.89724	7×10^{-5}	0.89	1.018536
0.5187	1.21054	0.87489	1.3×10^{-4}	1.01	1.07
0.0979	0.38241	0.85031	3×10^{-4}	1.06	0.6076881

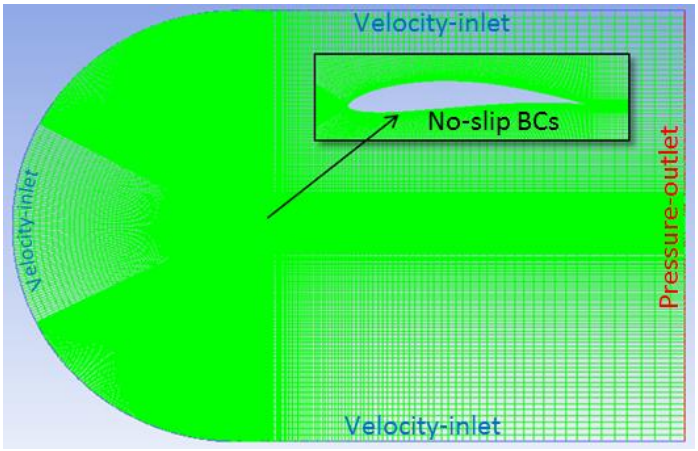

Figure 6. Meshed 2-D flow domain and boundary conditions

4.5. TIME STEP EFFECT STUDY

The pseudo-transient provided in Fluent is a form of implicit under-relaxation. It is used to accelerate the conversion of a steady-state solution. The time step size of this technique was examined. The results at three sizes of time step are listed in Table 4 below. The effect of changing the time step within this range was insignificant on the calculated C_M. The time step of 0.1 sec was considered in this study for solution acceleration. However, at some operating conditions during this study, the solution started to diverge, so the smaller time steps were considered.

Table 4. Time step effect on the solution

3.4.3 Pseudo-transient time step (sec)	Rotor/Tunnel mesh size (million)	C_M
0.1		2.3008×10^{-3}
0.01	1.85/1.8	2.3023×10^{-3}
0.001		2.3035×10^{-3}

5. NUMERICAL VERIFICATION

In this section, the performance of the SST k–ω model with the MRF approach was compared against a transient sliding mesh modeling and large eddy simulation for performance verification.

5.1. SLIDING MESH MODELING FOR MOMENT VERIFICATION

The sliding mesh modeling (SMM), available in Fluent, was used to calculate C_M over a full cycle of rotation. The results were then used to verify the MRF calculation. The C_M was obtained every 5^o of rotation. The used rotor had a chord length of 1.676 cm (0.66 in.) and was rotated at 125 RPM and exposed to a water flow of 0.91135 m/s. The time step (the time required for the rotor to rotate 5^o) was calculated based on the degree of step rotation and the rotational speed and was found 0.00667 sec. The total number of steps for a full cycle was 72. The number of iterations per step was set to 200 iterations to allow for step convergence. The results of the averaged azimuthal C_M calculated using SMM are

presented in Figure 7. The averaged C_M using SMM was 6.913×10^{-3}, which is satisfactorily close to the C_M obtained using MRF (6.575×10^{-3}). This indicates that the approximated solution of the frozen rotor (fixed rotor mesh) using MRF is satisfactory for this rotor solidity and other rotors with higher solidities. The SMM is preferred if the rotor has very low solidity (where results depend on rotor position) and also if the unsteady interactions (e.g., wake and shock interactions) are important, yet SMM requires more computational time.

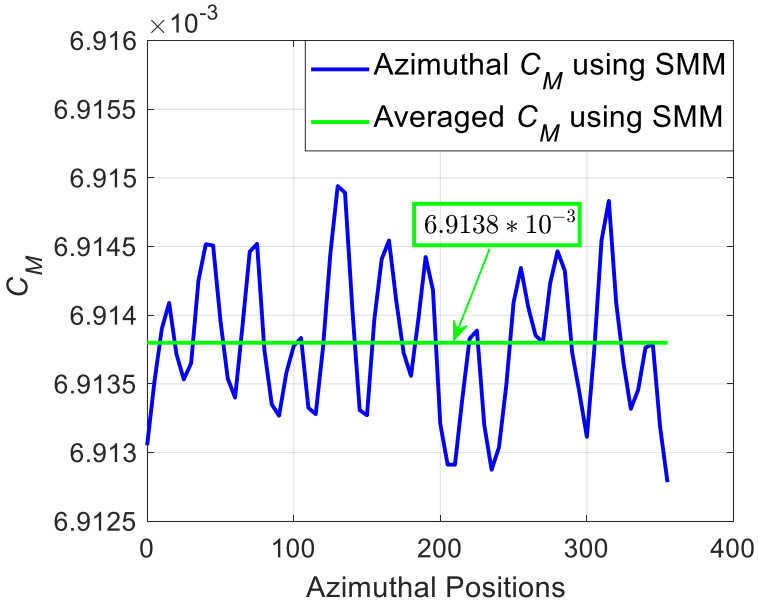

Figure 7. Azimuthal and averaged C_M obtained using SMM

5.2. LARGE EDDY SIMULATION FOR WAKE VERIFICATION

The large eddy simulation (LES) model employs spatially-filtered Navier–Stokes equations to compute structures that are not smaller than the grid size while utilizing a subgrid-scale model (Fluent utilizes Boussinesq hypothesis [39]) to simulate the smaller

scales of the flow structure, which are considered mostly isotropic. The model has become a common tool for performing a high-fidelity numerical simulation to observe the wake of wind/water turbines [6, 7, 40, 41]. Nevertheless, using LES at wall vicinities (e.g., blades BL) is computationally expensive due to the fact that all eddies are small at wall vicinity [37]. Furthermore, modeling using LES becomes extremely more expensive when simulating multiple turbines (e.g., wind farm and multi-turbine system). Hence, RANS simulations are often employed. The drawback of using RANS models to simulate the wake is that they may overpredict the amount of diffusion [32]. A way to reduce the computational requirements of LES is to couple it with RANS models, which gives the hybrid-model of Detached Eddy Simulation (DES) [32, 42], often referred to as the hybrid LES/RANS. However, the weakness of using this model is the response to the ambiguous grids' size (a fine wall-parallel grid reigns) [42, 43]. For the case when BL of the turbine blades are of less importance and the focus is on the free shear turbulence in the wake, the LES grid could be coarsened and the rotor presented by an actuator disk [7, 9, 40, 41, 44]. The DES turbulence model provided in Fluent 18.2 was used. The used DES model was based on SST k–ω.

The axial (streamwise) normalized velocity (u/U) profiles were extracted from vertical center lines at 1 dia. and 3 dia. downstream locations. u/U profiles were plotted against the water tunnel height (y) in Figures 8a and 8b. The used rotor and operational conditions are similar to those used in Section 5.1 (moment verification). The SST k–ω model provided a satisfactory axial velocity profile at the location of 1 dia. when compared to the DES model (Figure 8a). However, SST k–ω model showed a faster rate of recovery

as the flow traveled farther downstream to the location of 3 dia., as shown in Figure 8b. This may slightly alter the prediction of C_P for the multi-turbine system.

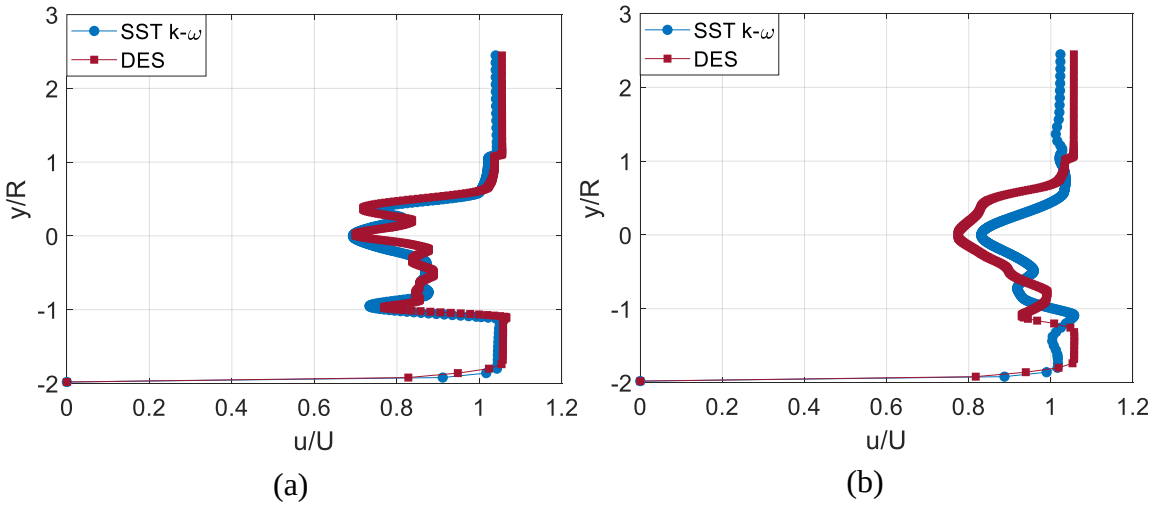

Figure 8. Comparison u/U profiles produced by SST k–ω and DES at two different downstream locations, (a) 1 dia. and (b) 3 dia.

6. EXPERIMENTAL METHODOLOGY

Power measurement and flow visualization experiments were conducted in a water tunnel to validate the simulation results, evaluate the hydrodynamic efficiency, and visualize wake characteristics. A description of the experimental work is given in this section. Detailed information on the experimental setup and experimental procedure can be found in a previous work by the authors [20]. The setup for the power measurement in the current work was modified from the previous work such that the thrust force can be acquired through a swinging mechanism. More details about the upgraded setup are provided in Section 6.2.

6.1. WATER TUNNEL

The proposed hydrokinetic turbine systems were tested at the water tunnel facility at Missouri University of Science and Technology (Missouri S&T). The Water Tunnel Laboratory at Missouri S&T is a Rolling Hills Research Corp. model 1520-HK. It had a test section width, depth, and length of 0.381 m × 0.508 m × 1.524 m (15 in. × 20 in. × 60 in.), respectively, and a maximum water velocity of approximately 1 m/s. A speed controller was used to vary a pump engine frequency in the range between 2.5 to 40 Hz so that the flow speed in the test section could be controlled. The test section had four surfaces made principally of tempered glass (lateral sides, bottom, and downstream) to allow maximum viewing of the tested model. An illustration of the facility used in this study is given in Figure. 9.

Figure 9. Water tunnel facility

6.2. EXPERIMENTAL SETUP AND PROCEDURE

6.2.1. Power Experiment. The setup for power measurement had two assemblies: (a) fixed assembly and (b) swinging assembly. The fixed assembly comprised a platform mounted upon the water tunnel shoulders. The swinging assembly was to allow thrust force transmission and was comprised of all the other components such as shafts, sensors, gears, bearings, and the rotor. The swinging assembly was attached to the fixed platform by a pillow block bearing. Figures 10a and 10b are an image and a schematic of the experimental setup for power measurement. The thrust force exerted by the flow on the rotor(s) was measured using a loading cell (maximum load of approximately 67 N). The swinging mechanism allowed the thrust force on the rotor(s) to be conveyed to the loading cell through a vertical pipe and the pillow block bearing. The swinging mechanism was balanced vertically to eliminate the system components' mass effect. The vertical pipe was also used to enclose the rotatory vertical power shafts. The vertical pipe itself was then enclosed by a composite shield to prevent the water flow from exerting forces on the submersed segment of this vertical pipe. Thus, the only considered thrust force is that exerted on the rotor(s). The composite shield had a symmetrical hydrofoil cross-section. The shield was manufactured using the same composite materials and fabrication process used for the composite blades (described in Section 6.2.3).

The torque and rotational speed required for power calculation were measured using a 0.353 N.m FUTEK time-average reaction torque (TART) sensor and a time-average rotational speed (TARS) sensor. The mechanical work generated by the system's rotor(s) was conveyed to the torque and rotational speed sensors through horizontal and vertical transmission shafts. Bevel gears were used to connect these vertical and horizontal

transmission shafts. The relationship between the power coefficient (C_P) and the *TSR* was obtained by gradually increasing an applied load. The applied load was altered by the mean of a magnetic particle clutch (maximum torque of 0.226 N.m) that was run by a power supply with controllable voltage and current.

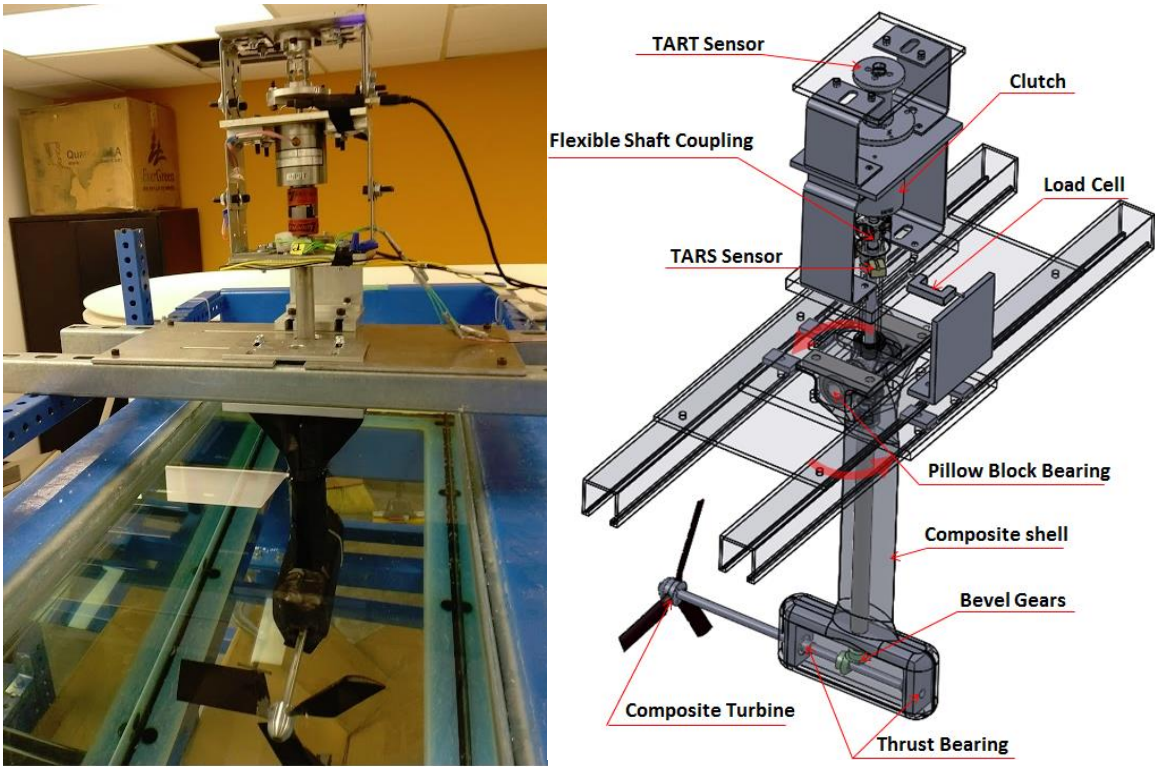

(a) (b)

Figure 10. (a) Turbine system operating in the water tunnel and (b) schematic of the experimental setup for power measurement

6.2.2. PIV Experiment. The water tunnel flow was seeded with glass spheres particles (density of 1100 kg/m3 and an average diameter of 9-13 μm and a). A Nd:YAG laser was aligned horizontally and pointed towards a mirror at the bottom of the test section.

The mirror reflected the laser sheet upward to visualize the investigated flow region. A digital camera was adjusted to digitize the illuminated area of interest. The laser sheet was placed at 1 dia. behind the multi-turbine system rotors at two radial locations off the center. The PIV experiment specifications are listed in Table 5. The PIV system components are illustrated in Figure 11a. Figure 11b shows a visualized flow field during the PIV experiment.

Table 5. PIV experiment specifications

Flow velocity (m/s)	Rotational speed (*RPM*)	Downstream location (dia.)	r/R
0.91135	165 225	1	35% & 75%

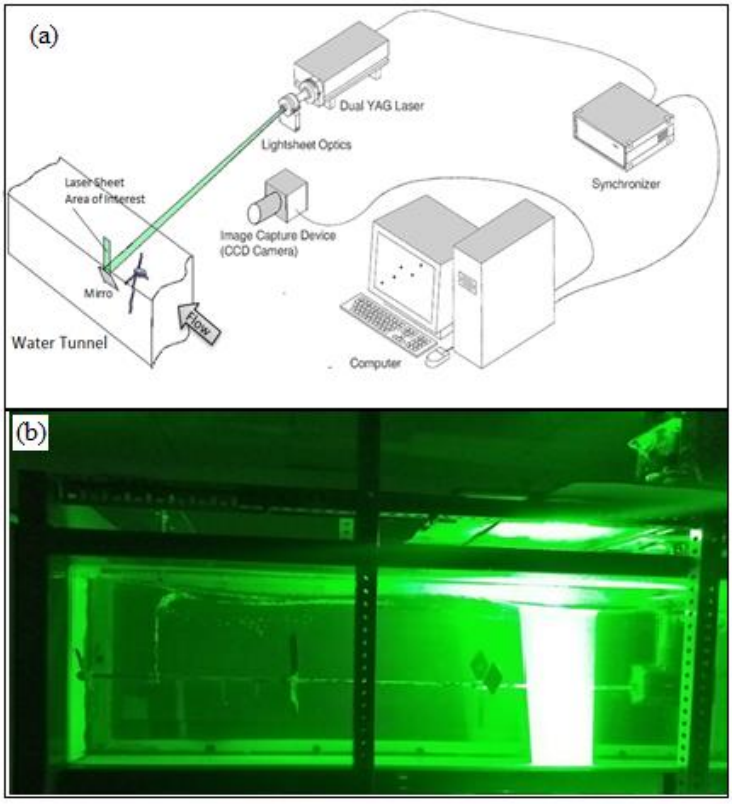

Figure 11. (a) Schematic of the PIV system and (b) PIV experiment

6.2.3. Rotor and Composite Blade. A composite three-blade HAHkT was used in this study. The composite material selected for the blades was carbon/epoxy prepreg. The technique utilized for blade fabrication was out-of-autoclave (OOA) [20]. The manufactured blade had Eppler 395 hydrofoil. The blades were untwisted and had a fixed chord length of 5.08 cm (2 in.). This blade was found to have optimum performance in the solidity numerical investigation (Sections 7.2 and 7.3). The blade span was cut to 96.32 mm (3.792 in.) to mitigate the blockage effects (blockage ratio was approximately 20%). The manufactured blade is shown in Figure 12. An aluminum hub with diameter and length of 25.4 mm (1 in.) was used. The hub had set screws at the back to hold the blades' root. The manufactured rotor was placed perpendicular to the incoming flow with its center located at a depth of 26.67 cm (10.5 in.) from the free surface.

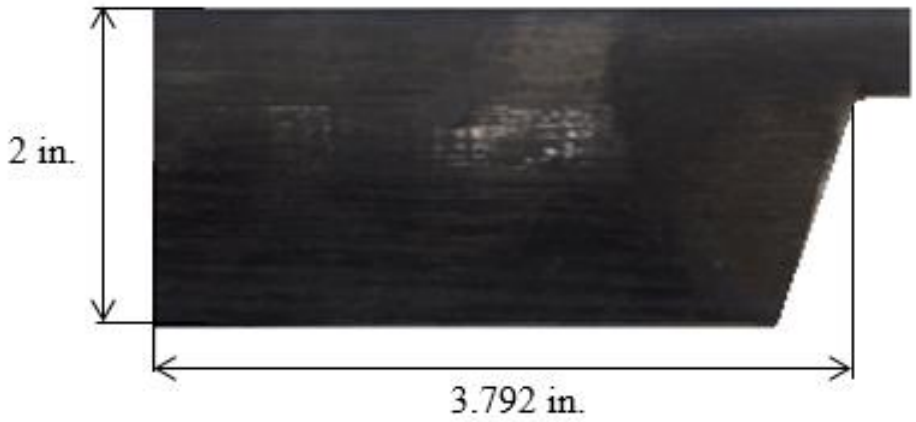

Figure 12. Manufactured blade with Eppler 395 hydrofoil and optimized solidity

7. RESULTS AND DISCUSSION

7.1. EXPERIMENTAL VALIDATION

In this section, the CFD simulation results of power coefficients and downstream velocity profiles are validated against the current work experimental results.

7.1.1. Power Validation. The power and thrust coefficients were obtained experimentally to validate the simulation results. The experiment setup described in Section 6.2 was used for the experimental measurement. The blades were pitched to 20^{o} and the rotor was exposed to a water flow of 0.91135 m/s. The turbine was loaded gradually using the magnetic particle clutch while torque, thrust, and rotational speed were acquired using the TART sensor, loading cell sensors, and TARS sensor, respectively. Finally, the power and thrust coefficients were calculated using Equations 3 and 4, respectively.

Figures 13a and 13b show, respectively, the power and thrust coefficients that were generated by the CFD (SST k–ω) and validated against the experimental results. The predicted power coefficient (Figure 13a) showed a good agreement in the regions of *TSR* higher than the peak. Nevertheless, CFD slightly overpredicted the C_{P_peak}. This overprediction was attributed to SST k–ω slightly overestimating the lift coefficient at the stalled angle of attacks [36]. The angle of attack increased and approached the stall value as the *TSR* was decreased. This happened because of the fact that the *TSR* is reduced by lowering the rotational speed, Ω, as defined in Equation 5. Consequently, the incoming flow angle, Ø, along the blade increases (Ø has a reciprocal relationship with Ωr, Equation 8). This, in turn, will result in a gradual increase of the angle of attack, α, toward the blade root (Equations 7 and 8). This eventually will cause an increase in the inboard segment of

the blade that operates at the stall conditions [20]. Thus overestimation of the predicted torque and generated power resulted as shown in Figure 13a. In Figure 13b, SST k–ω constantly underpredicted the thrust coefficient by about 5.03-6.31% at the regions of *TSR* higher than the peak. The simulated thrust coefficient approached the experimental measurements as *TSR* decreased.

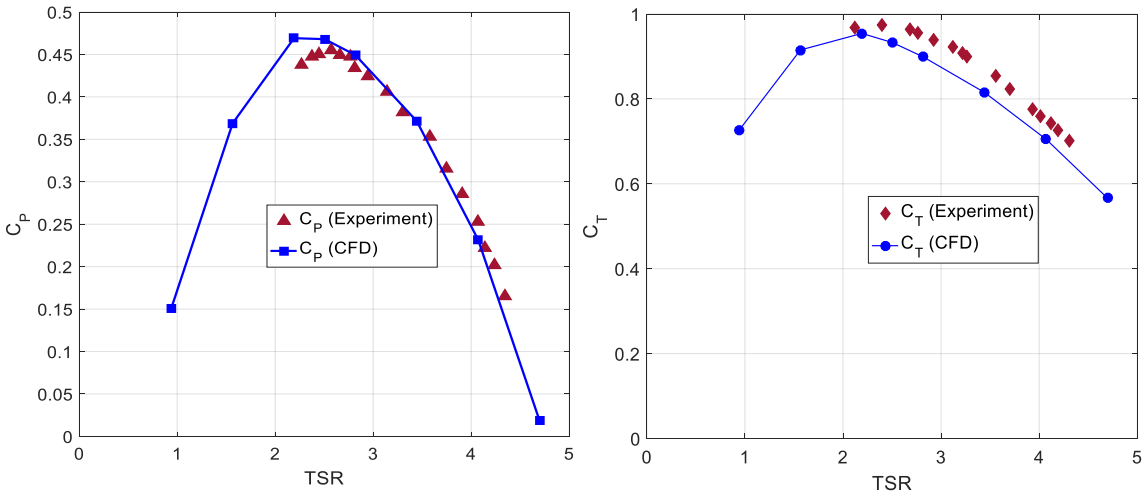

(a) (b)

Figure 13. Experimental validation of 2 in. chord blade turbine: (a) C_P and (b) C_T

7.1.2. Wake Validation. The axial velocity profiles at 1 dia. behind the rotors of the multi-turbine system were extracted at two radial locations (r/R = 0.35 and r/R = 0.75) from both the CFD (SST k–ω) and PIV results. The used multi-turbine system had three rotors with x = 2 dia. between them. The flow velocity and rotational speed were 0.91135 m/s and 165 RPM (*TSR* = 2.067), respectively. A number of 100 optical images were taken for each PIV test. The instantaneous 2-D velocities from the PIV measurements were processed, post-processed, and averaged. The CFD velocity profiles were extracted at the

radial locations from both sides (left and right) downstream of the rotors. The two left and right profiles for each case were then averaged to mitigate the stationary rotors position-effects (recall that CFD used MRF). The highest velocity deficit did not always occur at the centerline behind the rotors. However, for the sake of comparison, the highest velocity deficit was shifted to the zero height (centerline). The same was considered in Figure 28.

The results show that the CFD overestimated the highest velocity deficit behind the first rotor when r/R=0.35 (Figure 14a). However, CFD acceptably predicted the highest velocity deficit behind the second rotor at the same radial location (Figure 14b). The velocity profiles behind the second and third rotors at r/R=0.75 are illustrated in Figures 14c and 14d. The highest velocity deficit was fairly predicted by CFD at these locations. However, averaging the CFD axial velocity data had less effect on smoothing the velocity profiles. Therefore, the profiles were more distorted. If sliding mesh modeling (SMM) sampled data is used, the CFD velocity profile will likely be smoother, yet the SMM is computationally expensive (see Section 5.1). Interestingly, the highest velocity deficit behind the second rotor was higher than that behind the third rotor in both PIV and CFD results. This is likely attributed to the fact that, at this rotational speed, the third rotor absorbed smaller kinetic energy compared to the second rotor, as we will see in Figure 23a. That means the decrease in flow momentum through the third rotor was smaller than that through the second rotor. Considering the accumulated wake effects and the wake expansion and recovery as the flow travels downstream, the velocity profile behind the third rotor had a smaller velocity deficit compared to the velocity profile behind the second rotor.

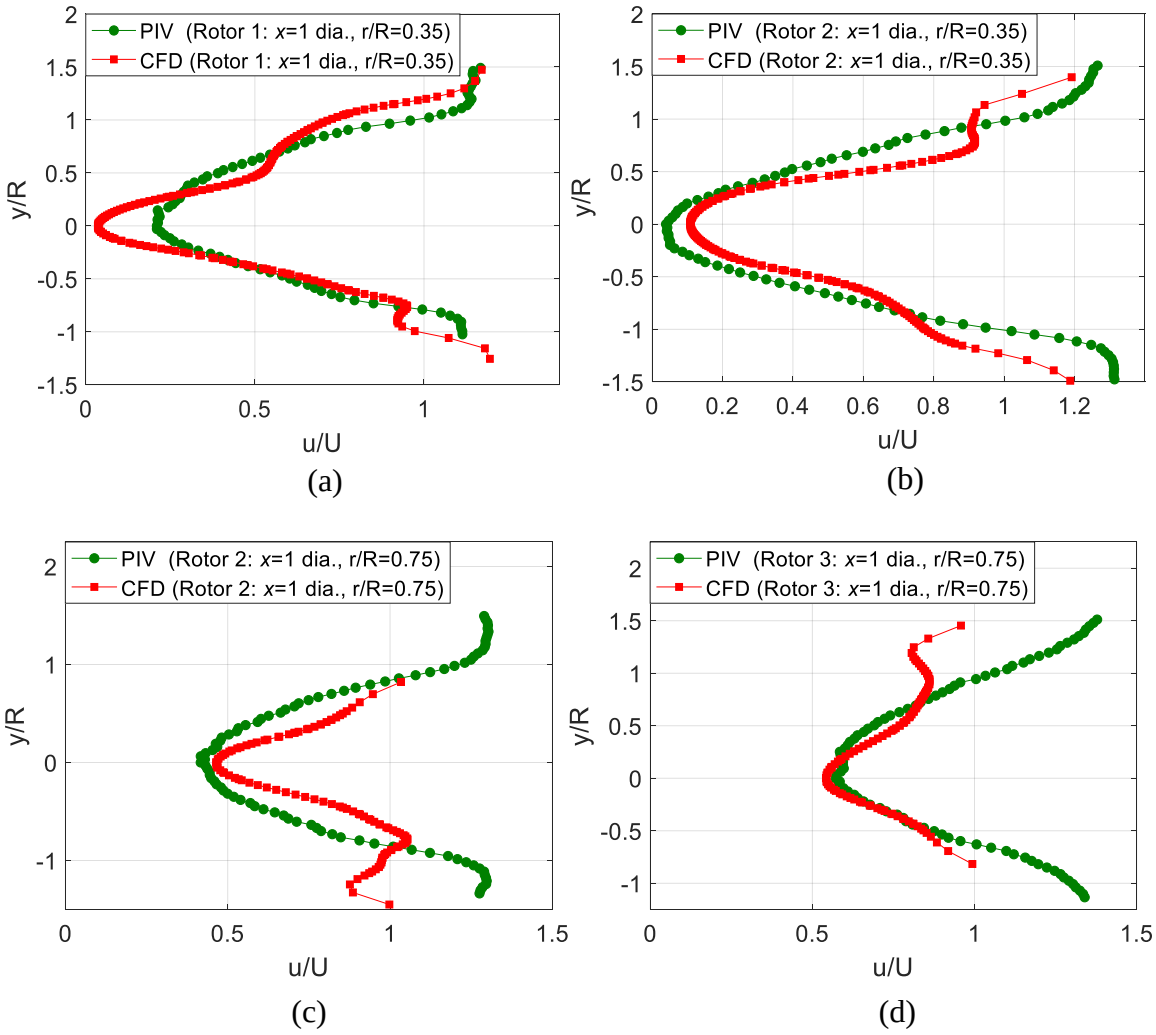

Figure 14. CFD wake validation against PIV results

7.2. SOLIDITY STUDY

The power harvested by a turbine is augmented by increasing both the flow speed and the thrust exerted by the turbine on the flow. Solidity is an important factor that controls the amount of thrust. Nevertheless, the increase in the thrust is accompanied by an increase in the flow impedance which in turn reduces the kinetic flux passes through the rotor. Therefore, there is a critical level of the solidity beyond which the flow impedance becomes critically high and the harvested power starts to decline. In this section, a 3-D numerical

simulation was performed in order to locate the best solidity at which the rotor will have the highest efficiency. Four rotors with different blade chord length and a similar radius were utilized in this solidity study. For all studied rotors, the operational conditions were the same and similar to those used in the grid independent study. However, the *TSR* range was varied so the highest C_p is included. Table 6 shows the geometric characteristics of the studied rotors while Figure 15 shows their structured mesh.

Table 6. Rotors' geometrical properties

	Rotor radius	Chord length (c)	Number of blades	Solidity (σ)
Rotor 1	10.902 cm (4.292 in)	1.676 cm (0.66 in.)	3	0.07342
Rotor 2		2.54 cm (1 in.)	3	0.11124
Rotor 3		5.08 cm. (2 in.)	3	0.22248
Rotor 4		7.62 cm (3in.)	3	0.33372

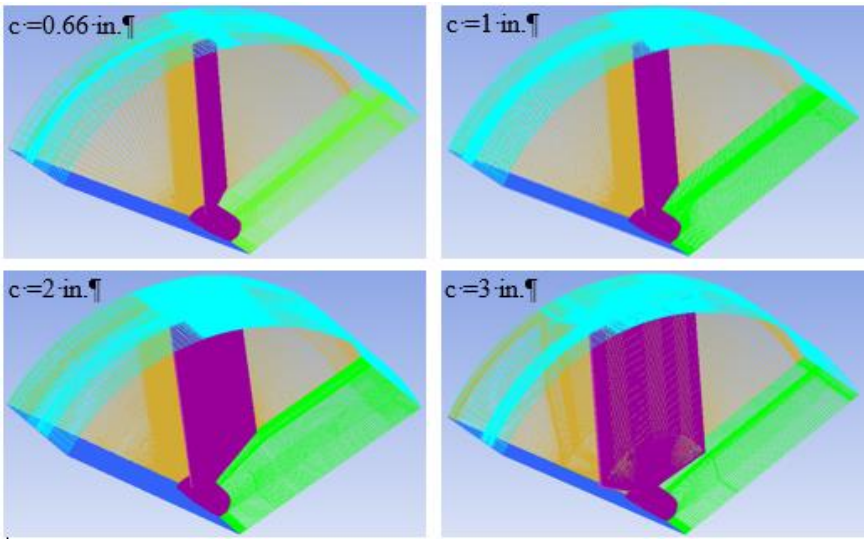

Figure 15. Structured mesh for the studied rotors

Figure 16 shows that the power coefficient was almost doubled as solidity increased from $\sigma = 0.07342$ (c = 0.66 in.) to $\sigma = 0.22248$ (c = 2 in.). However, increasing the solidity to 0.33372 (c = 3 in.) caused a decrease in the power coefficient due to the high flow impedance (less kinetic flux passes through the rotor). Increasing the solidity was always associated with a shift in C_{P_peak} toward lower *TSR*. The decrease in the operational *TSR* (*TSR* at the C_{P_peak}) as solidity increased was attributed to the slower stream velocity (higher flow impedance) through the rotor. This requires slower rotational speed to get a larger angle of attack along the blade span and thus larger lift and better turbine performance. Keep in mind that the velocity used to define the *TSR* is the free stream velocity (Equation 5), so the operational *TSR* at the C_{P_peak} is smaller as the solidity increased. Another observation was that as solidity decreased, the operational range of *TSR* increased (flatter peak) which was also reported in [1]. Varying the pitch angle of the different solidity blade may improve the performance even further [4, 5], but this was out of the scope of this study.

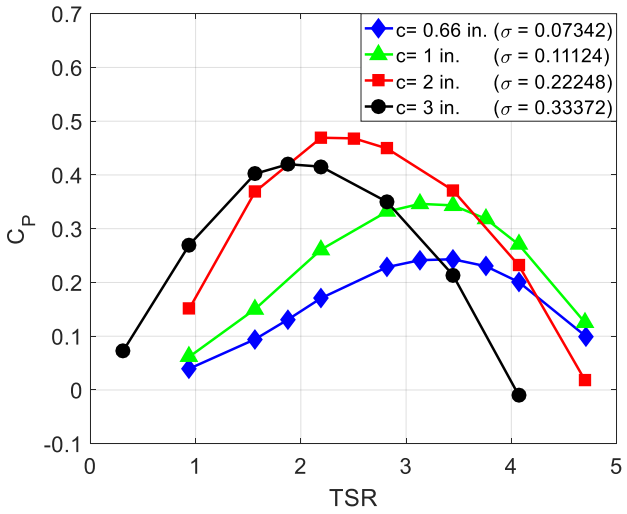

Figure 16. C_P vs *TSR* generated by rotors with different solidities

7.3. BLOCKAGE EFFECTS INVESTIGATION

The investigation of the solidity effect in Section 7.2 was performed by simulating the different solidity rotors operating in a water tunnel domain. This was to allow validation of the CFD simulation results against the water tunnel measurements. All rotors used in this study had the same diameter, thus, generated the same blockage ratio ($\varepsilon \sim 20\%$). However, rotors' efficiencies may show different responses to the blockage effects due to their various solidities, which may modify the considered rotor optimum solidity. Therefore, the performance of the confined rotors was corrected to account for these blockage effects. The thrust coefficients from the simulated confined rotors were used in the blockage correction model. A discussion of the employed blockage correction model can be found in [13, 19, 45]. The corrected confined results were compared against CFD unconfined results. This was to examine the correction model accuracy. The outer flow domain for the CFD unconfined case had a cylindrical shape with a radius of 0.508 m (20 in.). The downstream and upstream lengths were similar to the water tunnel in the confined case. The outer cylindrical domain cross-section yielded a blockage ratio of 4.6%, which was considered effectively unblocked [18]. The solver, boundary conditions, mesh density, and other simulation inputs of the unconfined simulation are similar to those used in the confined simulation.

The results comparison from confined CFD, unconfined CFD, and the blockage correction model are demonstrated in Figure 17. The sensitivity to the blockage effects for the two low-solidity rotors, $\sigma = 0.07342$ and $\sigma = 0.11124$, was insignificant at low *TSR*s up to 2.25 and 2, respectively. For all studied solidities, the blockage correction model had a satisfactory prediction at *TSR*s lower than the operational *TSR* (the C_{P_peak} region).

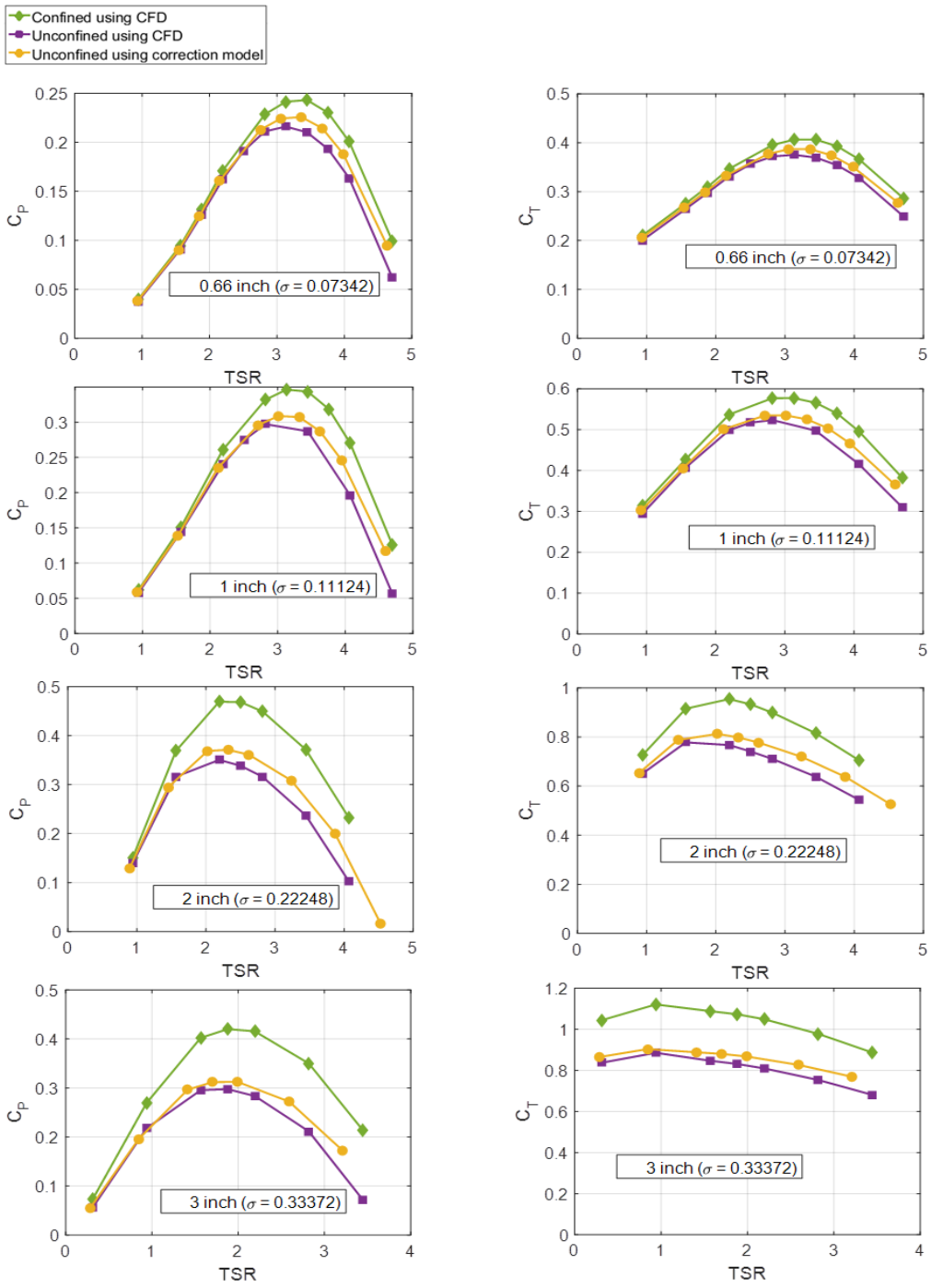

Figure 17. C_P vs *TSR* generated by CFD modeling confined rotors, CFD modeling unconfined rotors, and blockage correction of confined rotors

Then, the correction model started to slightly overestimate the C_P as *TSR* increased towards and beyond the peak point. Unlike a large-scale turbine, a lab-scale turbine needs to rotate

at a higher speed to achieve higher *TSR* (see Equation 5). When a turbine rotates with a high speed relative to incoming flow speed, the rotor inters the turbulent wake status (also known as “brake state”). Turbulent wake increases as more outer flow propagates into the wake [9, 24]. In such conditions, applying Bernoulli’s equations in the wake to correct the blockage effects is not accurate. A complementary empirical model is needed to correct the blockage effects in this region of high *TSR* [18].

Analysis of the all unconfined results (Figure.18) reveals that the rotor with σ = 0.22248 (c = 2 in.) still had the best performance when operated in an open environment. The operational *TSR* for all solidities was found to be insensitive to the blockage effects.

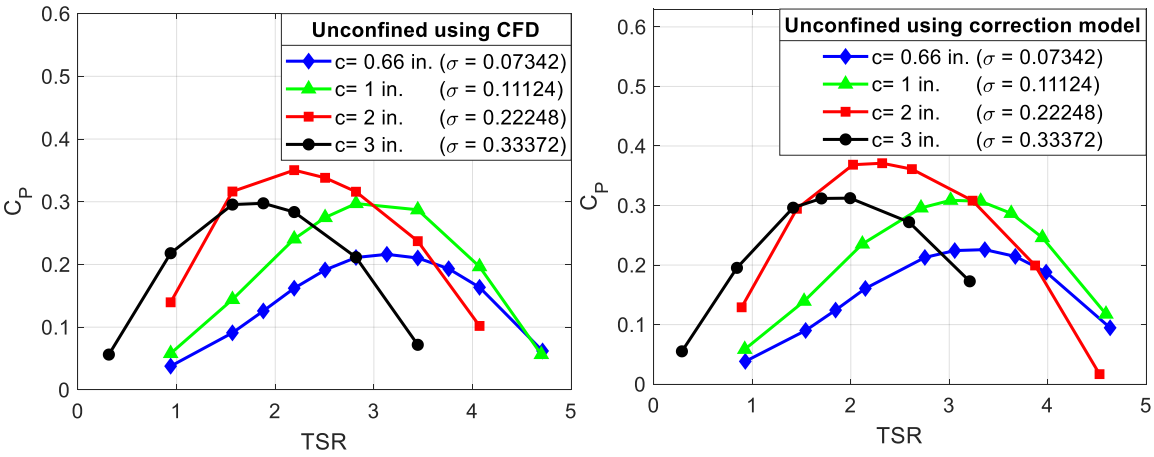

Figure 18. Unconfined results generated by (a) CFD and (b) blockage correction model

Figure 18 also reveals that the rotor with the highest solidity (σ = 0.33372 and c = 3 in.) had the highest drop in C_{P_peak} when operated in the unconfined flow. The C_{P_peak} for this unconfined rotor was 0.2975, which was almost equal to that of the unconfined rotor with

the second-lowest solidity ($\sigma = 0.11124$ and c = 1 in.), which was $C_{P\_peak} = 0.2971$. The rotor with the highest solidity had the largest blade chord, which meant the largest lift surface. However, it also had the highest flow impedance; therefore, less kinetic flux passed its rotor when operated in the open flow.

The change in C_{P_peak} due to blockage effects was found to be proportional to the turbine solidity. The increase ratio in C_{P_peak} under confinement effect was calculated using Equation 16 and the results are listed in Table 7.

$$C_{P\_\text{peak}}\ \text{increase ratio} = \left|\frac{Confined\ C_{P\_peak} - \ unconfined\ C_{P\_peak}}{unconfined\ C_{P\_peak}}\right| \times 100 \qquad (16)$$

Table 7. Confinement effect on C_P peak for various solidities

Turbine solidity (σ)	C_{P_peak} increase ratio (%)
0.07342	12.5142
0.11124	16.5237
0.22248	33.9161
0.33372	41.1475

7.4. MULTI-TURBINE SYSTEM PERFORMANCE ANALYSIS

The multi-turbine system comprised several rotors mounted to the same shaft. These rotors were designed to have the optimum solidity ($\sigma = 0.22248$) and the previously mentioned small radius of 10.902 cm (4.292 in.) and were appropriately placed apart. This will allow this multi-stage conversion device to efficiently operate in limited-space sites,

such as rivers and artificially-made channels. For better understanding of the multi-turbine system design criteria, its configuration was varied as described in Section 2.2. Each configuration was modeled using similar solver, boundary conditions, mesh density, and other simulation inputs used in the single-turbine system simulation. The water tunnel streamwise length was expanded such that the 10 dia. between the first rotor and the input and 25 dia. between the last rotor and the output was maintained. The shaft between the rotors was rotated to resemble the real case (Figure 19a). The shaft was modeled to have a thin surrounding cylindrical flow domain (Figure 19b) to allow the implementation of the moving reference frame technique, similar to that considered when simulating the rotors. In Figure 19b, some interfaces of the first rotor and all of the water tunnel were hidden to allow an illustration of the meshed surfaces and interfaces. Figure 19c shows the system imported into Fluent for components combining and simulation.

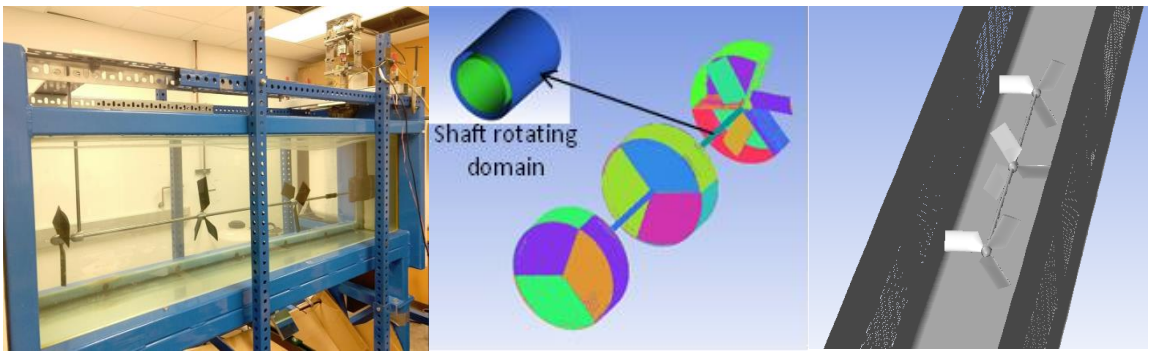

(a) (b) (c)

Figure 19. Multi-turbine system comprised three rotors placed 2 dia. apart: (a) experiment setup for validation, (b) meshed rotors and rotating shaft, and (c) the system configured in Fluent for CFD simulation

The predicted performance of the multi-turbine system (NR = 3 and x = 2 dia.) was validated against the experiment result. Figures 20a and 20b show, respectively, the validation of the predicted C_P and C_T using CFD (SST k–ω). Similar to the single-turbine case, the CFD has a slightly higher C_P peak (Figure 20a). This was attributed to the larger staled blade span segment where SST k–ω slightly overestimated the lift coefficient [36]. In Figure 20b, SST k–ω underpredicted C_T at *TSRs* higher than the operational value. The simulated C_T approached the experimental results as *TSR* decreased towards the C_T peak.

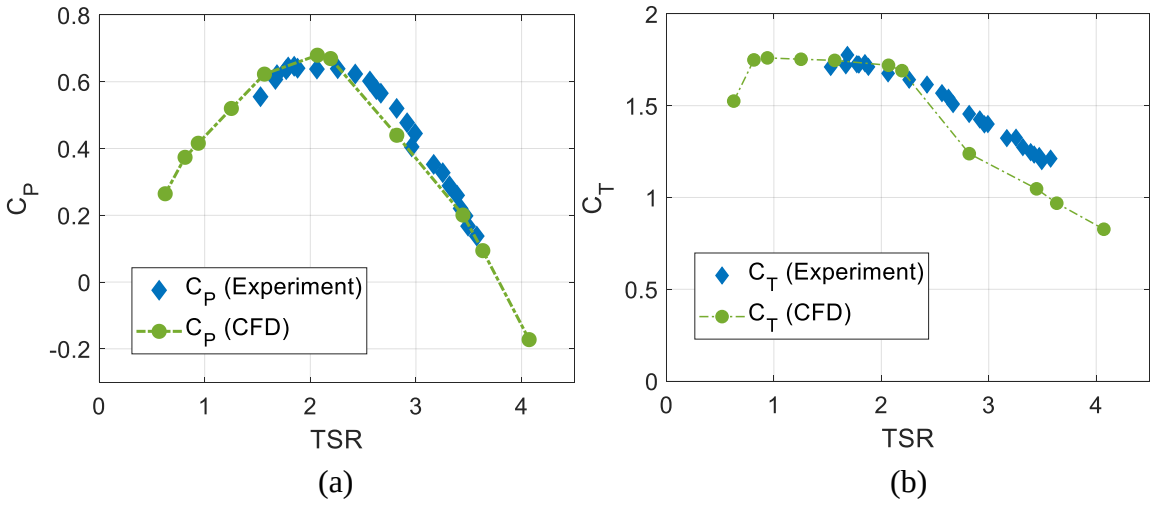

Figure 20. Experimental validation of CFD modeling multi-turbine system (NR = 3, and x = 2 dia.) with optimized solidity: (a) C_P and (b) C_T

A performance comparison between the single-rotor turbine system and a three-rotor multi-turbine system with an axial distance between the rotors set to 2 dia. is presented in Figure 21. The C_P of the multi-turbine system increased by about 47% and shifted to lower *TSR* (Figure 21a). The multi-turbine system had higher blade surfaces exposed to the flow which resulted in higher torque force, and, thus, higher extracted energy. The left shift

in C_{P_peak} was attributed to slower kinetic flux through the downstream rotors. The slower flow required slower rotational speed to generate an increased α that yields a higher lift force. The thrust coefficient of the multi-turbine system was also increased; the increase ratio was about 83% at the peak, as shown in Figure 21b.

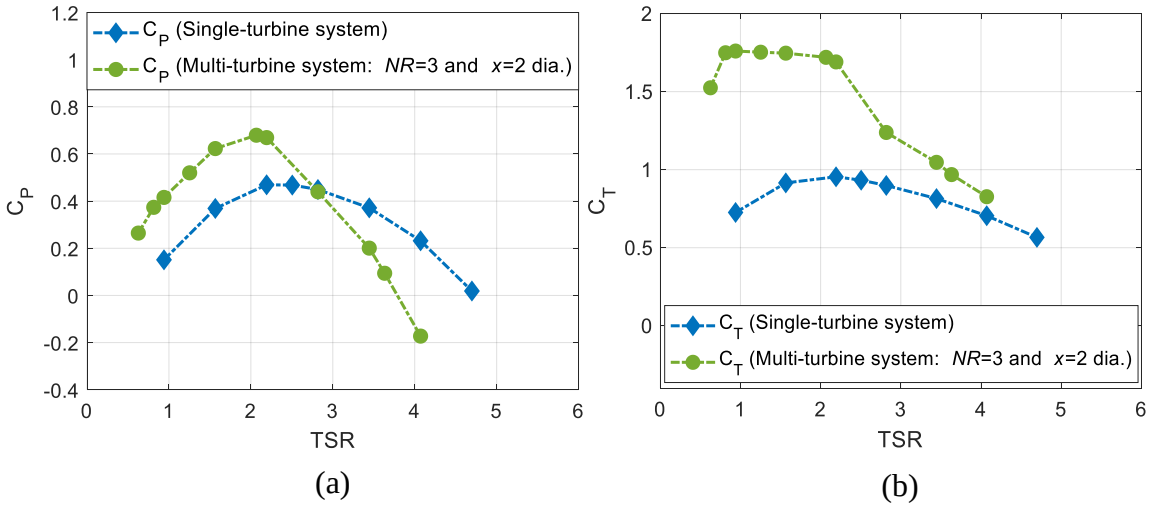

Figure 21. Comparison between single-turbine system and multi-turbine system (NR = 3 and x = 2 dia.): (a) C_P and (b) C_T. Both systems utilized optimum-solidity rotors

The multi-turbine system's performance response to the axial distance between the rotors was investigated and the results are illustrated in Figure 22. Increasing the distance between the optimum-solidity rotors from x = 2 dia. to x = 4 dia. had an insignificant effect on the C_{P_peak} amplitude and C_T curve. However, the multi-system with x = 4 dia. had the advantage of a flatter C_{P_peak} (wider operational range of TSR). This was due to the earlier occurrence (at $TSR \geq 2.82$) of an opposite torque generated by the second and third rotors of the multi-turbine system with x = 2 dia. (Figure 23a), while the multi-turbine system with x = 4 dia. had a delayed opposite torque generated by the second and third rotors at

$TSR \geq 3.45$ (Figure 23b). The earlier opposite torque caused a faster drop in the accumulated C_P curve of the multi-turbine system with x = 2 dia.

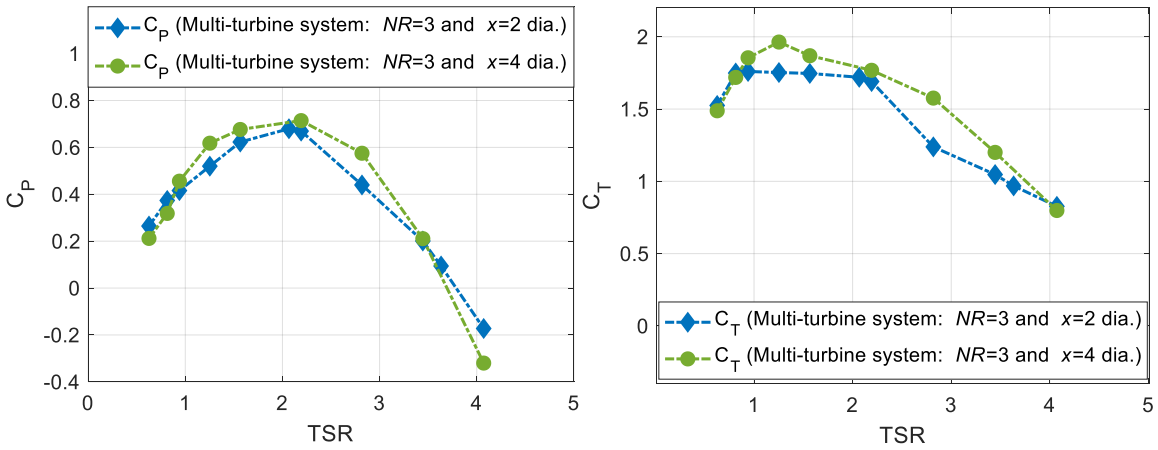

(a) (b)

Figure 22. Effect of the distance between rotors on the multi-turbine system: (a) C_P and (b) C_T. Both systems utilized optimum-solidity rotors

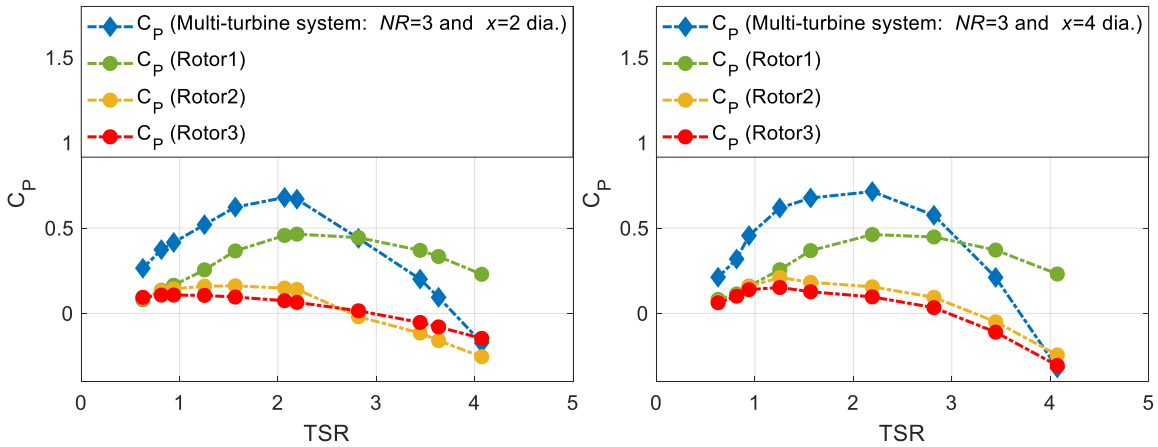

(a) (b)

Figure 23. Performance per each rotor of multi-turbine systems configured with (a) NR = 3 and x = 2 dia. and (b) NR = 3, and x = 4 dia.

To investigate the source of the opposite torque in more detail, the angles of attack along the leading-edge span of the first and third rotors' blades were obtained at the rotational speed of 290 RPM (*TSR* = 3.632). The first and third rotors were considered because they had the same azimuthal angle, so the position effect is eliminated. First, the incoming flow angles were attained via extracting the components of the axial and tangential velocities at different locations in front of the blades' LE span (offset = 2 mm). Then the angle of attack (α) was calculated using Equation 7. As expected, the first rotor had α decreased toward the blade tip as shown in Figure 24. The negative angle of attack at the outboard region was caused by the increased tangential velocity, which resulted in a small positive incoming flow angle ($\emptyset$). For $\emptyset$ with values smaller than the pitch angle (θ), α had negative values (see Equation 8). Regarding the third rotor, it was observed that within the span range of $0.3 < r/R < 0.85$, the flow streamed toward the leading edge with a negative $\emptyset$. This meant that the flow stream was attacking the LE from the suction side. This, in turn, produced a negative angle of attack. This was believed to be due to the very high rotational speed of the third rotor, which was mainly caused by the first rotor (the rotors are connected by a shaft). Meanwhile, the incoming flow approached the third rotor with very slow speed due to the wake effects. This caused the third rotor to work as a fan that got its energy from the first rotor; it thus generated the opposite torque at these high *TSR*. The negative angle of attack at the tip region ($r/R > 0.85$) was attributed to the increased tangential velocity, similar to the first rotor case.

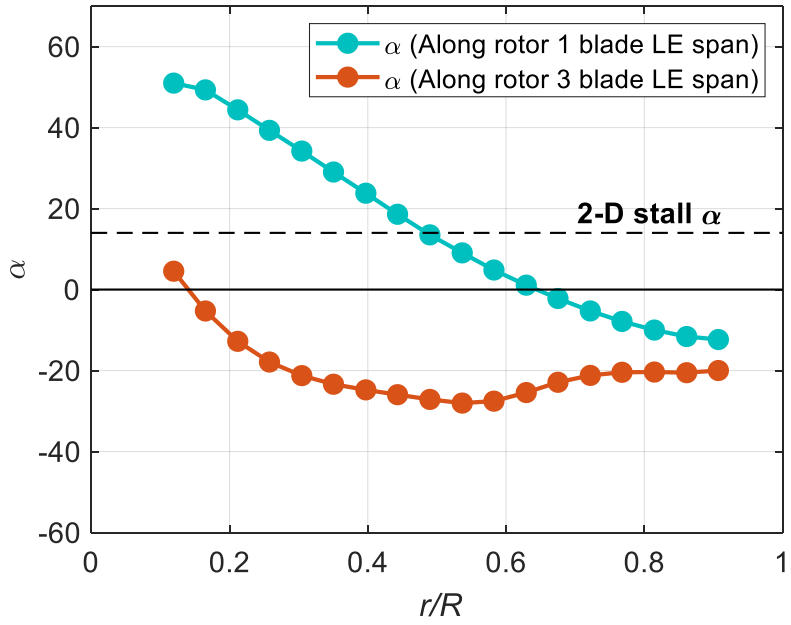

Figure 24. The angle of attack distribution along the LE span of first and third rotors' blades

To further investigate the effects of this negative angle of attack, the pressure coefficient ($C_{pressure}$) was obtained at different chordwise locations (L) at various sections along the blades of the first and third rotors of the multi-turbine system and at the same rotational speed of 290 *RPM*. The $C_{pressure}$ is calculated as

$$C_{pressure} = \frac{p - p_{ref}}{0.5\,\rho U^2} \tag{16}$$

where p is the local static pressure, p_{ref} is the reference static pressure (p_{ref} = atmospheric pressure + $\rho g h$, where h is the height of the fluid at that location). The first rotor's blade inboard segment ($r/R \leq 0.6$) was characterized by pressure coefficients with negative peaks at the LE on the suction side (Figure 25a). The inboard segment ($r/R \leq 0.6$) of the third rotor's blade and the outboard segments ($r/R \geq 0.7$) of the first and third rotors'

blades all had pressure coefficient with positive peaks at the LE on the suction side (Figure 25b-d). This was compatible with the angle of attack distribution at these segments in Figure 24. For all these segments with positive $C_{pressure}$ peaks at the LE on the suction side there were corresponding negative $C_{pressure}$ peaks at the LE on the pressure side. This kind of pressure distribution yielded unfavorable forces that generated torque in the opposite direction.

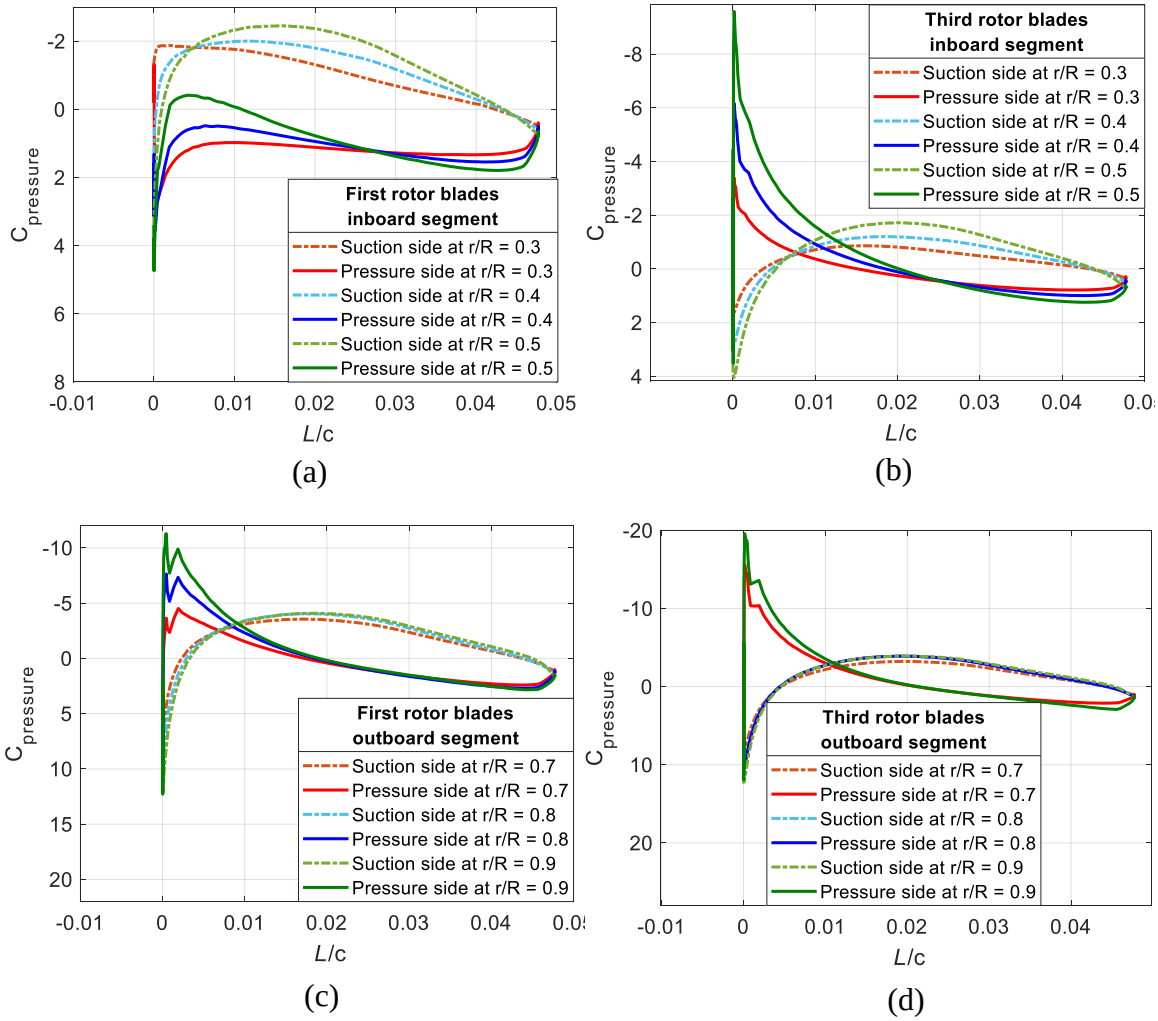

Figure 25. $C_{pressure}$ distribution along the LE span of first and third rotors' blades

The power coefficients produced by rotors were staked in columns in Figure 26 to show each rotor contribution to the overall system. Figures 26a and 26b both show that as the *TSR* increased toward the C_{P_peak}, the first rotor contribution dominated. This was attributed to wake effects. As the first rotor rotational speed increased (rotor unloaded), it absorbed more kinetic energy (efficiency increased) and generated wake with a higher velocity deficit. Therefore, the latter rotors were exposed to a slower kinetic flux that passed through their swept areas, and thus they generated lesser energy. The first rotor contribution still dominated over the others even when *TSR* increased beyond the C_{P_peak}. In Figures 26a and 26b, the system's C_P curve (dashed green) passing through the columns at the high *TSRs* indicates the unfavorable opposite torque effect. The overall increase and decrease in the power coefficient as *TSR* increased were ascribed to the angle of attack distribution along the blades span. The angle of attack is influenced by the magnitude of the rotational speed and the incoming flow.

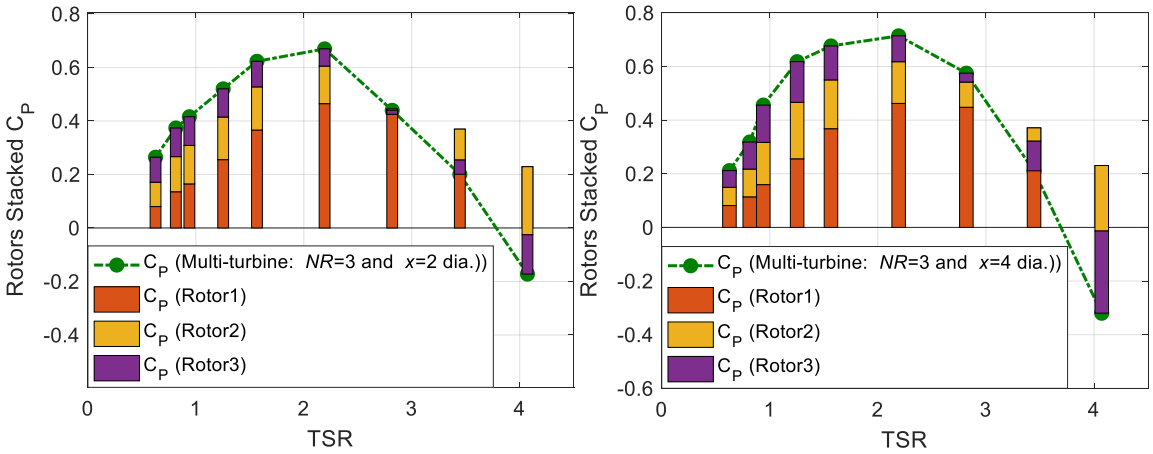

Figure 26. Stacked rotors' performance to show their contribution effect on the overall system efficiency (a) *NR* = 3 and *x* = 2 dia. and (b) *NR* = 3 and *x* = 4 dia.

Five-rotor multi-turbine system was also simulated in this study to examine the effect of increasing the number of rotors on the multi-turbine system performance. Figure 27a shows that the performance of the multi-turbine system was slightly improved at the C_{P_peak} by about 4% when the number of rotors was increased from three to five. At the peak region, the added fourth and fifth rotors were exposed to a low kinetic flux due to the wake-interaction effects (see Figure 30). At the peak region, the upstream rotors had the highest absorption of the passing kinetic energy which resulted in the highest velocity deficit inside the wake. The system's maximum thrust was increased by about 45%.

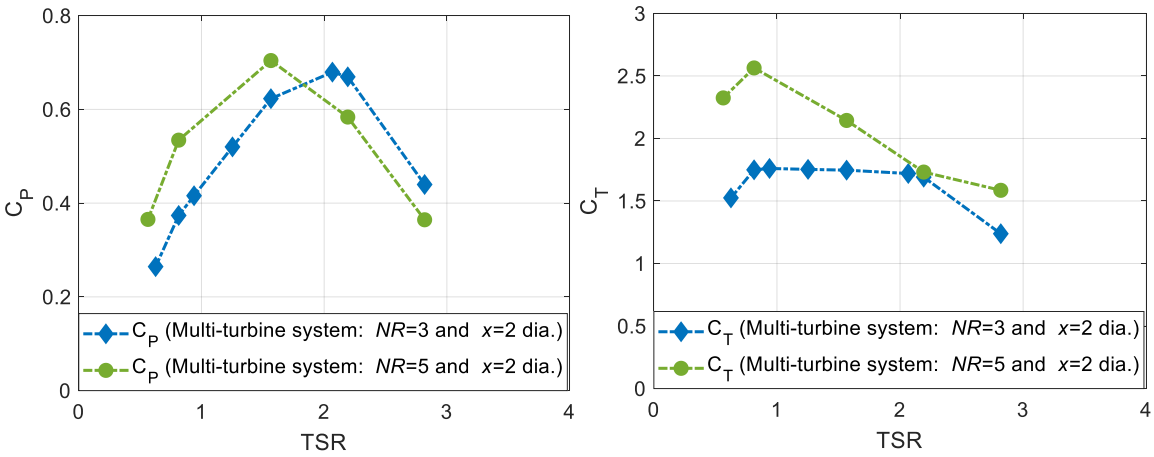

(a) (b)

Figure 27. Effect of increasing the number of rotors on the multi-turbine system (x = 2 dia.)

7.5. WAKE INVESTIGATION

When turbines operate on the same site, their efficiencies are altered due to the effects of their wakes and wake-interaction. Understanding wake behavior is essential to

optimize the arrangement of these neighboring turbines and to enhance the overall performance. In this study, the wakes and wake-interaction structures were investigated experimentally and numerically to enhance the performance of the proposed multi-turbine system.

7.5.1. PIV Experimental Results. The PIV experimental results were post-processed using Tecplot 360 software. Axial velocity profiles were extracted from vertical lines located on the post-processed 2-D flow domains. The 2-D flow domains were considered at different radial locations during the PIV experiment. The vertical lines were located at 1 dia. downstream from each rotor. The PIV experimental configurations are listed earlier in Table 5.

Figures 28a-28f summarize important observations from the PIV experiment. The axial velocity profiles at 1 dia. behind the three rotors at 35% of the blade span were normalized and presented in Figures 28a and 28b. The highest velocity deficit was found behind the second rotor rather than the third rotor for both tested rotational speeds of 165 *RPM* (*TSR* = 2.067) and 225 *RPM* (*TSR* = 2.818). The reason was likely attributed to the very low kinetic energy absorbed by the third rotor (Figure 23.a). This, in turn, resulted in a smaller velocity deficit profile (after recovery) behind the third rotor compared to that behind the second rotor. This observation was also explained in Section 7.1.2 in more detail. It was also observed that the profile with the highest velocity deficit was the widest. This was for the flow to maintain the conservation of mass. The velocity deficit at 0.35R was higher than at 0.75R, as shown in Figures 28c and 28d. This increased velocity deficit was attributed to the increase of the turbulence kinetic energy towards the wake centerline [3, 46]. The effect of varying the rotational speed was also examined and presented in

Figures 28e and 28f and was found insignificant at these considered operational conditions. At the rotational speed of 165 *RPM*, both profiles behind the second and third rotors had a slightly higher velocity deficit compared to the 225 *RPM* rotational speed case. That was due to the higher efficiency of the rotors at the 165 *RPM* rotational speed (see Figure 23a). The higher efficiency indicates higher harnessing of the kinetic flux and, thus, slower flow. This conclusion can also be drawn from Figures 28a and 28b, though the first rotor wake appeared to be less responsive to varying the rotational speed within this investigated range. In all figures, the bypass section (the region between the wake boundary and the surrounding surfaces, such as tunnel bed and free surfaces), had u/U exceeded 1 due to the blockage effects.

7.5.2. CFD Numerical Results. The CFD simulation allows for analysis and visualization of flow regions that cannot be visualized by the PIV system due to structure obstruction or turbulence disturbance.

The velocity characteristics downstream of the various-solidity rotors are analyzed and presented in Figure 29. The axial and tangential flow velocities were extracted at lines spanned downstream of the rotors. The axial velocity data line was located at the centerline, where the highest velocity deficit likely occurred. The tangential velocity (u_T) data line was located on a vertical mid-plane at 0.5R above the rotor. Since the rotational speed had an insignificant effect on the axial velocity deficit (Figure 28), the optimum operational rotational speeds were considered for the various-solidity rotors. Figures 29a and 29b show that increasing the rotor's solidity resulted in increased initial axial velocity deficit and tangential velocity. This was due to the increased flow impedance as solidity increased.

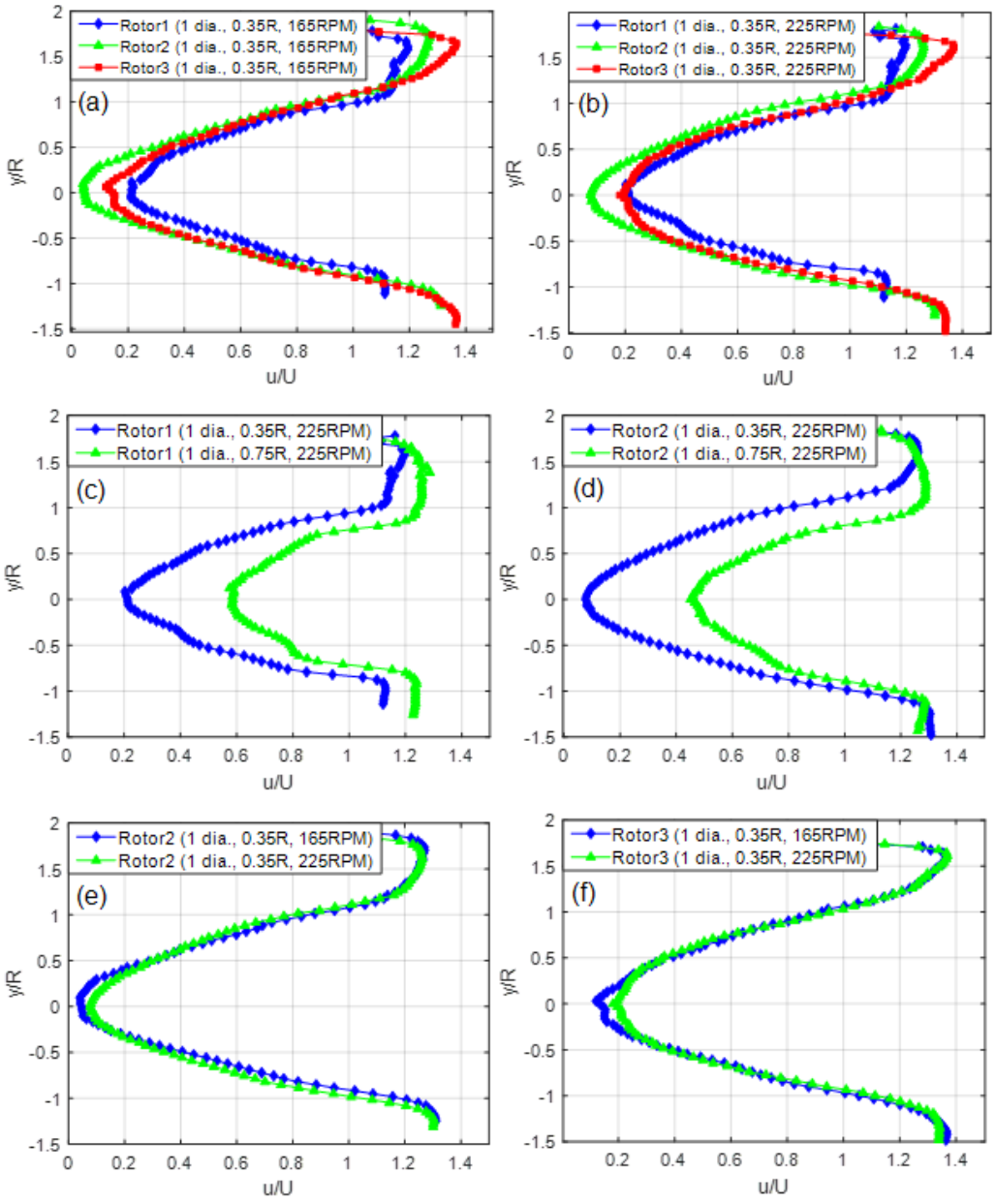

Figure 28. Velocity profiles from PIV measurements at 1 dia. behind the rotors of the multi-turbine system (NR = 3 and x = 2 dia.)

The rotor with the second highest solidity ($\sigma = 0.22248$) had an initial axial velocity deficit close to the rotor with the highest solidity ($\sigma = 0.33372$). This was due to the fact that, besides the relatively high flow impedance caused by this rotor ($\sigma = 0.22248$), this

rotor had the highest momentum absorption. Up to about x = 8 dia., all rotors' wakes showed high but slightly different rates of recovery of the flow's axial velocity (Figure 29a). The rate of recovery was proportional to the level of solidity. Beyond the x = 8 dia., the wakes' rates of recovery decreased and had relatively the same slope. Figures 29a and 29b both illustrate that as the axial velocity deficit recovers, the tangential velocity decays.

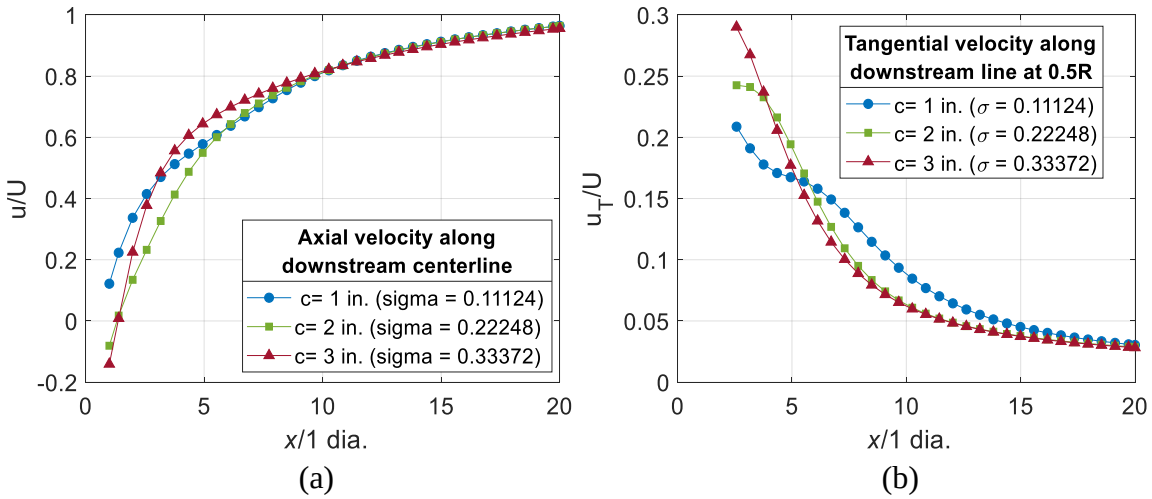

Figure 29. Solidity effect on the distribution of (a) u/U and (b) u_T/U along downstream lines

Figure 30 shows the flow's axial and tangential velocities downstream of the rotors of a multi-turbine system that had rotors placed 4 dia. apart. The lines used to collect the velocities' data were located at 50% of the rotor radius on both left and right sides, spanned downstream the rotors. The rotational speed was 125 RPM and flow speed was 0.91135 m/s. At x = 1 dia., the order of the velocity deficit caused by the three rotors agrees with the PIV results in Figure 28. However, the system's configuration and rotational speeds were different in both figures. The first and second rotors showed the flow's axial velocity

recovery up to about x = 3.25 dia. (Figure 30a). After this x distance, the flow's axial velocity started to decline due to the flow impedance imposed by the downstream rotors. The third rotor showed a comparatively more linear rate of recovery of the flow's axial velocity. However, it is likely that this rate of recovery will decline at a farther downstream distance (similar to Figure 29). The flow tangential velocity showed an initial increase then decrease as flow traveled downstream. The initial increase was likely due to the angular momentum exerted by the rotors' blades on the passing flow.

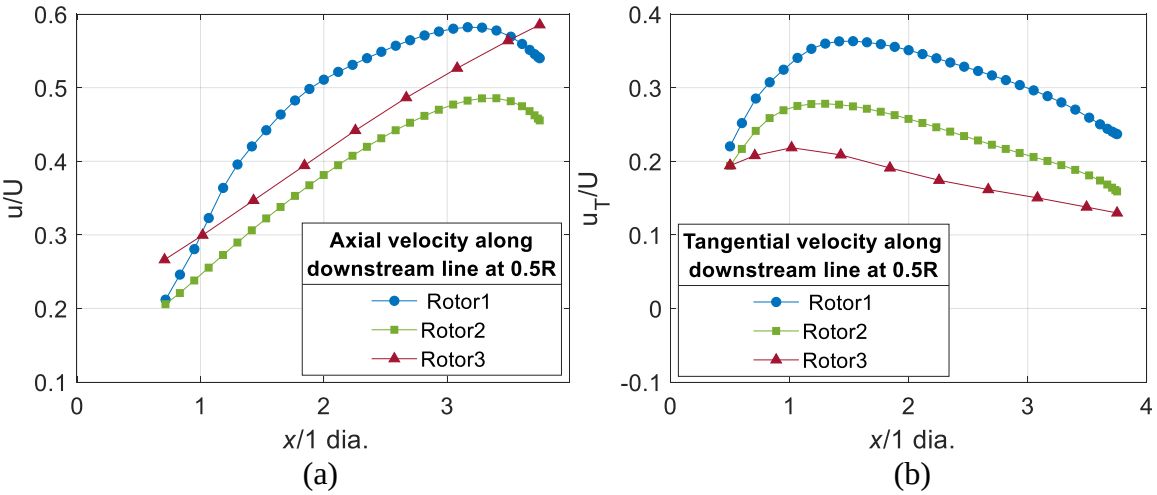

Figure 30. The distribution of (a) u/U and (b) u_T/U along downstream lines behind the rotors of the multi-turbine system (NR = 3 and x = 4 dia.)

The wake share layer width (generated by the all rotors) along the water tunnel streamwise horizontal mid-plane is presented in Figure 31. The black streamline represents the flow with a speed magnitude of 0.91135 m/s (similar to the inlet velocity). This streamline shows wake expansion as the flow travels away from upstream rotors and wake reduction as the flow streams toward downstream rotors. The black streamline at the sides

shows the thickness of the walls' boundary layers. The faded red color represents the accelerated flow between the rotors/rotors' wakes and the lateral walls.

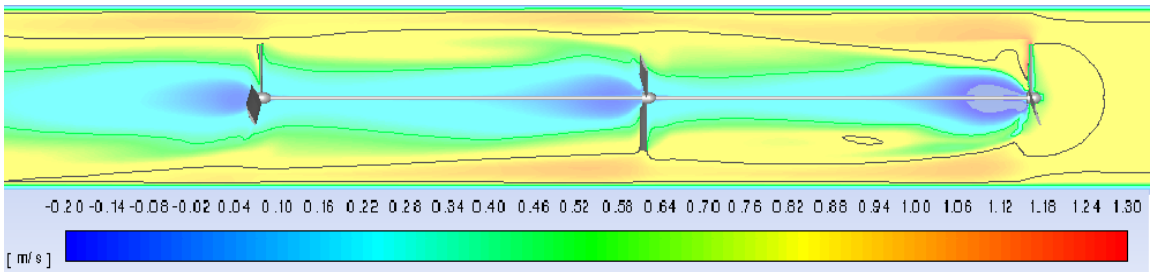

Figure 31. Upper view of the flow domain with a multi-turbine system (*NR* = 3 and *x* = 4 dia.) operating at a rotational speed of 125 RPM

8. CONCLUSIONS

This work focused on optimizing the performance of a coaxial horizontal axis hydrokinetic turbine system for low hydraulic head and limited operational space applications. An experimental apparatus was developed for power and thrust evaluation and for simulation validation. A particle image velocimetry was used to visualize the downstream flow and validate simulations results. Computational fluid dynamics simulations were performed throughout this work for studying and optimizing the proposed multi-turbine system. Grid and time step independent studies were performed to enhance CFD simulation reliability.

Rotors with different chord lengths were simulated using SST k–ω turbulence model with the MRF approach to investigate the solidity effects on the turbine performance. The blockage effect on the performance of the various-solidity rotors was

also studied. The rotor with a chord length of 2 in. ($\sigma = 0.22248$) was found to have the best performance in both confined and unconfined flows. The power coefficient was almost doubled when using this optimum solidity compared to the lowest-solidity rotor ($\sigma = 0.07342$). The effect of the blockage was found to increase with increasing the turbine solidity.

The rotor with optimum solidity was built and integrated into both the single- and multi-turbine systems. This was to evaluate the systems' performance and validate the CFD simulation results. The predicted C_P for both single- and multi-turbine systems were in good agreement with the experimental measurements. Nevertheless, CFD slightly overpredicted the C_{P_peak} due to the stall effects. The simulated C_T was slightly underestimated. However, the C_T peak magnitude was satisfactorily estimated by CFD.

The multi-turbine system (NR = 3 and x = 2 dia.) enhanced the efficiency by 47% compared to the single-turbine system when both systems utilized optimum-solidity rotors. Increasing the distance between the rotors from x = 2 dia. to x = 4 dia. had not significantly increased C_{P_peak} magnitude. However, the C_{P_peak} was flattened (i.e., the operational range of TSR was increased) as the distance between the rotors increased from x = 2 dia. x = 4 dia. The effect of increasing the number of rotors on the performance of the multi-turbine system was also studied. The multi-turbine system with NR = 5 and x = 2 dia. improved efficiency by only 4% compared to the multi-turbine system with NR = 5 and x = 2 dia. However, further investigation of adjusting the pitch angle of the downstream rotors may improve the overall system efficiency (the current system rotors had a fixed pitch angle of 20^o).

Finally, the wake downstream of differently configured turbines were studied and their effects on the turbines' performance were analyzed.

ACKNOWLEDGMENTS

The authors would like to acknowledge the financial support received from the Department of Mechanical and Aerospace Engineering at Missouri University of Science and Technology and the support of the Office of Naval Research (Grant # N000141010923).

REFERENCES

[1] M. C. Rector, K. D. Visser, and C. Humiston, "Solidity, blade number, and pitch angle effects on a one kilowatt HAWT," presented at the 44th AIAA Aerospace Sciences Meeting and Exhibit, Reno, NV, January 09 -12, 2006.

[2] M. M. Duquette and K. D. Visser, "Numerical implications of solidity and blade number on rotor performance of horizontal-axis wind turbines," *Journal of Solar Energy Engineering*, vol. 125, no. 4, pp. 425-432, 2003.

[3] S. Subhra Mukherji, N. Kolekar, A. Banerjee, and R. Mishra, "Numerical investigation and evaluation of optimum hydrodynamic performance of a horizontal axis hydrokinetic turbine," *Journal of Renewable and Sustainable Energy*, vol. 3, no. 6, pp. 1-18, 2011.

[4] T. Hernandez Madrigal, A. Mason-Jones, T. O'Doherty, and D. O'Doherty, "The effect of solidity on a tidal turbine in low speed flow," presented at the 2th European Wave and Tidal Energy Conference (EWTEC), Cork, Ireland, August 27-September 1, 2017. Available: http://orca.cf.ac.uk/id/eprint/105214

[5] C. Morris, A. Mason-Jones, D. M. O'Doherty, and T. O'Doherty, "The influence of solidity on the performance characteristics of a tidal stream turbine," presented at the European Wave and Tidal Energy Conference, Nantes, France, September 6-11, 2015. Available: http://orca.cf.ac.uk/id/eprint/81362

[6] B. Elie, G. Oger, P.-E. Guillerm, and B. Alessandrini, "Simulation of horizontal axis tidal turbine wakes using a Weakly-Compressible Cartesian Hydrodynamic solver with local mesh refinement," *Renewable Energy,* vol. 108, pp. 336-354, 2017.

[7] R. J. Stevens, L. A. Martínez-Tossas, and C. Meneveau, "Comparison of wind farm large eddy simulations using actuator disk and actuator line models with wind tunnel experiments," *Renewable Energy,* vol. 116, pp. 470-478, 2018.

[8] P.-A. Krogstad, L. Sætran, and M. S. Adaramola, "“Blind Test 3” calculations of the performance and wake development behind two in-line and offset model wind turbines," *Journal of Fluids and Structures,* vol. 52, pp. 65-80, 2015.

[9] M. Calaf, C. Meneveau, and J. Meyers, "Large eddy simulation study of fully developed wind-turbine array boundary layers," *Physics of fluids,* vol. 22, no. 1, pp. 015110 (1-16), 2010.

[10] N. Stergiannis, C. Lacor, J. Beeck, and R. Donnelly, "CFD modelling approaches against single wind turbine wake measurements using RANS," in *Journal of Physics: Conference Series*, 2016, vol. 753, no. 3, pp. 1-16: IOP Publishing.

[11] Y.-T. Wu and F. Porté-Agel, "Large-eddy simulation of wind-turbine wakes: evaluation of turbine parametrisations," *Boundary-layer meteorology,* vol. 138, no. 3, pp. 345-366, 2011.

[12] T. Chen and L. Liou, "Blockage corrections in wind tunnel tests of small horizontal-axis wind turbines," *Experimental Thermal and Fluid Science,* vol. 35, no. 3, pp. 565-569, 2011.

[13] T. Kinsey and G. Dumas, "Impact of channel blockage on the performance of axial and cross-flow hydrokinetic turbines," *Renewable Energy,* vol. 103, pp. 239-254, 2017.

[14] A. Bahaj, L. Myers, R. Rawlinson-Smith, and M. Thomson, "The effect of boundary proximity upon the wake structure of horizontal axis marine current turbines," *Journal of Offshore Mechanics and Arctic Engineering,* vol. 134, no. 2, pp. 021104 (1-8), 2012.

[15] N. Kolekar and A. Banerjee, "Performance characterization and placement of a marine hydrokinetic turbine in a tidal channel under boundary proximity and blockage effects," *Applied Energy,* vol. 148, pp. 121-133, 2015.

[16] C. Garrett and P. Cummins, "The efficiency of a turbine in a tidal channel," *Journal of Fluid Mechanics,* vol. 588, pp. 243-251, 2007.

[17] G. Houlsby, S. Draper, and M. Oldfield, "Application of linear momentum actuator disc theory to open channel flow," University of Oxford, Oxford, UK, Technical report no. 2296-08, 2008.

[18] J. Whelan, J. Graham, and J. Peiro, "A free-surface and blockage correction for tidal turbines," *Journal of Fluid Mechanics,* vol. 624, pp. 281-291, 2009.

[19] M. Barnsley and J. Wellicome, "Final report on the 2nd phase of development and testing of a horizontal axis wind turbine test rig for the investigation of stall regulation aerodynamics," Carried out under ETSU Agreement E.5A/CON5103/1746, April 1990.

[20] A. Abutunis, G. Taylor, M. Fal, J. Nicholas, and K. Chandrashekhara, "Performance evaluation of coaxial horizontal axis hydrokinetic composite turbine system," presented at the Composites and Advanced Materials Expo (CAMX) Conference, Dallas, TX, October 26 - 29, 2015.

[21] P. Brøndsted, H. Lilholt, and A. Lystrup, "Composite materials for wind power turbine blades," *Annu. Rev. Mater. Res.,* vol. 35, pp. 505-538, 2005.

[22] S. L. Dixon, *Fluid mechanics and thermodynamics of turbomachinery*. Butterworth-Heinemann, 2005.

[23] F. R. Menter, "Two-equation eddy-viscosity turbulence models for engineering applications," *AIAA journal,* vol. 32, no. 8, pp. 1598-1605, 1994.

[24] K. Gharali and D. A. Johnson, "Numerical modeling of an S809 airfoil under dynamic stall, erosion and high reduced frequencies," *Applied Energy,* vol. 93, pp. 45-52, 2012.

[25] L. J. Vermeer, J. N. Sørensen, and A. Crespo, "Wind turbine wake aerodynamics," *Progress in Aerospace Sciences,* vol. 39, no. 6-7, pp. 467-510, 2003.

[26] M. Rahimian, J. Walker, and I. Penesis, "Performance of a horizontal axis marine current turbine–A comprehensive evaluation using experimental, numerical, and theoretical approaches," *Energy,* vol. 148, pp. 965-976, 2018.

[27] C.-J. Bai, W.-C. Wang, and P.-W. Chen, "Experimental and numerical studies on the performance and surface streamlines on the blades of a horizontal-axis wind turbine," *Clean Technologies and Environmental Policy,* vol. 19, no. 2, pp. 471-481, 2017.

[28] D. A. Johnson and L. King, "A mathematically simple turbulence closure model for attached and separated turbulent boundary layers," *AIAA journal,* vol. 23, no. 11, pp. 1684-1692, 1985.

[29] S.-P. Breton, "Study of the stall delay phenomenon and of wind turbine blade dynamics using numerical approaches and NREL's wind tunnel tests," PhD, Department of Civil and Transport Engineering, Norwegian University of Science and Technology, 2008.

[30] I. Herráez, B. Stoevesandt, and J. Peinke, "Insight into rotational effects on a wind turbine blade using Navier–Stokes computations," *Energies*, vol. 7, no. 10, pp. 6798-6822, 2014.

[31] C. Thumthae and T. Chitsomboon, "Optimal angle of attack for untwisted blade wind turbine," *Renewable Energy*, vol. 34, no. 5, pp. 1279-1284, 2009.

[32] B. Sanderse, "Aerodynamics of wind turbine wakes - literature review," Energy Research Center of the Netherlands (ECN), Petten, The Netherlands, Report no. ECN-E-09-016, 2009.

[33] N. Kolekar and A. Banerjee, "A coupled hydro-structural design optimization for hydrokinetic turbines," *Journal of Renewable and Sustainable Energy*, vol. 5, no. 5, pp. 053146 (1-22), 2013.

[34] A. Fluent, "18.2, Theory Guide, ANSYS Inc," *Canonsburg, PA*, 2017.

[35] R. H. Nichols, *Turbulence models and their application to complex flows* (University of Alabama at Birmingham, Revision). 2010, p. 89.

[36] A. Abutunis, R. Hussein, and K. Chandrashekhara, "A neural network approach to enhance blade element momentum theory performance for horizontal axis hydrokinetic turbine application," *Renewable Energy*, vol. 136, pp. 1281-1293, 2019.

[37] D. C. Wilcox, *Turbulence modeling for CFD*. DCW industries La Canada, CA, 2006.

[38] S. B. Pope, *Turbulent flows*. Cambridge University Press, Cambridge, UK, 2001.

[39] J. Hinze, *Turbulence*. McGraw-Hill Publishing Co, New York, 1975.

[40] Y.-T. Wu and F. Porté-Agel, "Simulation of turbulent flow inside and above wind farms: model validation and layout effects," *Boundary-layer meteorology*, vol. 146, no. 2, pp. 181-205, 2013.

[41] M. Churchfield *et al.*, "A large-eddy simulation of wind-plant aerodynamics," presented at the 50th AIAA Aerospace Sciences Meeting including the New Horizons Forum and Aerospace Exposition, Nashville, TN, January 09 -12, 2012.

[42] P. R. Spalart, "Detached-eddy simulation," *Annual Review of Fluid Mechanics*, vol. 41, pp. 181-202, 2009.

[43] P. R. Spalart, S. Deck, M. L. Shur, K. D. Squires, M. K. Strelets, and A. Travin, "A new version of detached-eddy simulation, resistant to ambiguous grid densities," *Theoretical and computational fluid dynamics*, vol. 20, no. 3, pp. 181–195, 2006.

[44] L. A. Martinez, C. Meneveau, and R. Stevens, "Wind farm large-eddy simulations on very coarse grid resolutions using an actuator line model," presented at the 34th Wind Energy Symposium, San Diego, CA, January 4-8, 2016.

[45] A. S. Bahaj, A. F. Molland, J. R. Chaplin, and W. M. J. Batten, "Power and thrust measurements of marine current turbines under various hydrodynamic flow conditions in a cavitation tunnel and a towing tank," *Renewable Energy*, vol. 32, no. 3, pp. 407-426, 2007.

[46] H. Xiao, L. Duan, R. Sui, and T. R¨osgen, "Experimental Investigations of Turbulent WakeBehind Porous Disks," presented at the Proceedings of the 1st Marine Energy Technology Symposium, Washington, D.C., April 10 - 11, 2013.

SECTION

4. CONCLUSIONS

The first paper involved the development and integration of BEM theory and NN models. The integrated BEM-NN model aimed to overcome the inherent convergence failure that usually happens during the BEM theory iteration and hinders the blade design process. The other role of the neural network model was to estimate the sectional blade hydrodynamic characteristics needed during the BEM model iteration. Different BEM correction models from the literature were integrated to improve the model's performance. Various structures of the NNs relating to the calculation of the hydrodynamic characteristic were examined to enhance the prediction of the sectional CL and CD. The approved NNs were satisfactorily able to estimate the sectional CL and CD in the overall range of the operational conditions, within the practical range of α. This approved NNs further enhanced the proposed model prediction compared to the classical BEM theory, which uses a constant Re. Moreover, the coupled BEM-NN successfully predicted the induction factors that failed to converge during the BEM iteration, even at high *TSR*. The BEM-NN was easily modified to accommodate a blockage correction model that does not require thrust measurements, and the results were satisfactory when validated against the experimental results of a low-solidity turbine operated in the water tunnel.

In the second paper, a multi-coaxial, three-blade HAHkT system was designed, built, and tested in the water tunnel. This modified energy conversion device was developed to operate in streams with low hydraulic head and small operational space. This

work aimed to evaluate and enhance the performance of the suggested multi-turbine system. The experiment setup was equipped with a clutch, time-averaged torque, and time-averaged RPM sensors for more accurate time-averaged power measurements. The blades had Eppler 395 hydrofoil with a chord length of 0.66 in. The blades were manufactured of composite materials using the OOA technique. The effects of flow velocity, pitch angle, and number of blades were investigated for the single-turbine system. The effects of the number of rotors, the distance between rotors, the rotors' relative installation angle, and shrouding were studied for the muli-turbine system. A particle image velocimetry was used to both investigate the wake velocity profiles and validate the CFD model. The optimum pitch angle for the blade using Eppler 395 hydrofoil was approximately 5o. The power curve peak shifted toward lower *TSR* and had a lower magnitude when the pitch angle increased. The two-rotor turbine system improved the performance by approximately 75% compared to the single-rotor turbine system. Adding the third rotor further improved the performance of the multi-turbine system by about 32%. This smaller improvement by the third rotor was attributed to the effect of the slower wake. The effect of the relative installation angle on the performance of the multi-turbine system (x = 2 dia. and x = 4 dia.) was found insignificant. The system performance was improved by about 11% when the distance between rotors was increased form x = 2 dia. to x = 4 dia. This performance increase was ascribed to the wake recovery. The shrouded multi-turbine system showed a significant performance enhancement. Integrating the duct improved the multi-turbine system performance by approximately 250%. In the wake investigation, the velocity deficit behind the six-blade turbine was higher than that behind the three-blade turbine, which indicates a higher kinetic energy absorption by the higher-solidity six-blade rotor. The

velocity deficit resulting from the six-blade turbine shows a faster rate of recovery compared to the three-blade turbine, but the rate of recovery decreased toward the 4 dia.

In the third paper, a computational fluid dynamics simulation utilizing the SST k–ω turbulence model and MRF technique was conducted to simulate the single- and multi-turbine systems. The simulation intended to optimize the performance of the proposed multi-turbine system that operates at sites with low head and limited operational space. The previous experimental setup was upgraded to allow for thrust measurement and blockage correction. The system configuration was altered, then its performance and flow characteristics were investigated. The simulation results for both the single- and multi-turbine systems showed a good agreement with experimental results. Solidity, blockage, and their interactive effects were investigated. The rotor with $\sigma = 0.22248$ had the best performance in both confined and unconfined flows. This rotor doubled the efficiency compared to the rotor with the lowest solidity of $\sigma = 0.07342$ (this low solidity was used in the previous work). The blockage effects on the turbine performance increased as the solidity increased. The multi-turbine system with $NR = 3$ and $x = 2$ dia. enhanced the efficiency by 47% compared to the single-turbine system. No significant increase in the power coefficient peak was observed when the distance between the rotors was increased from $x = 2$ dia. to $x = 4$ dia. However, the operational *TSR* range was increased due to the delay in the occurrence of opposite torque experienced by the downstream rotors. Increasing the number of rotors from three to five enhanced the performance by only 4%. Particle image velocimetry was used to investigate the velocity profiles inside the wake and validate the CFD results. The flow characteristics and their effects on the performance of the different turbine configurations were analyzed.

BIBLIOGRAPHY

[1] S. L. Dixon, *Fluid mechanics and thermodynamics of turbomachinery*. Butterworth-Heinemann, 2005.

[2] M. M. Duquette and K. D. Visser, "Numerical implications of solidity and blade number on rotor performance of horizontal-axis wind turbines," *Journal of Solar Energy Engineering,* vol. 125, no. 4, pp. 425-432, 2003.

[3] S. Subhra Mukherji, N. Kolekar, A. Banerjee, and R. Mishra, "Numerical investigation and evaluation of optimum hydrodynamic performance of a horizontal axis hydrokinetic turbine," *Journal of Renewable and Sustainable Energy,* vol. 3, no. 6, pp. 1-18, 2011.

[4] M. C. Rector, K. D. Visser, and C. Humiston, "Solidity, blade number, and pitch angle effects on a one kilowatt HAWT," presented at the 44th AIAA Aerospace Sciences Meeting and Exhibit, Reno, NV, January 09 -12, 2006.

[5] M. O. Hansen, *Aerodynamics of wind turbines*. Routledge, 2013.

[6] D. C. Wilcox, *Basic fluid mechanics*. DCW industries, 2010.

[7] T. Burton, N. Jenkins, D. Sharpe, and E. Bossanyi, *Wind energy handbook*. John Wiley & Sons, 2011.

[8] A. Bahaj, L. Myers, M. Thomson, and N. Jorge, "Characterising the wake of horizontal axis marine current turbines," *Proc. 7th EWTEC,* 2007.

[9] L. J. Vermeer, J. N. Sørensen, and A. Crespo, "Wind turbine wake aerodynamics," *Progress in Aerospace Sciences,* vol. 39, no. 6-7, pp. 467-510, 2003.

[10] B. Sanderse, "Aerodynamics of wind turbine wakes - literature review," Energy Research Center of the Netherlands (ECN), Petten, The Netherlands, Report no. ECN-E-09-016, 2009.

[11] T. Göçmen, P. Van der Laan, P.-E. Réthoré, A. P. Diaz, G. C. Larsen, and S. Ott, "Wind turbine wake models developed at the technical university of Denmark: A review," *Renewable and Sustainable Energy Reviews,* vol. 60, pp. 752-769, 2016.

[12] M. Magnusson and A.-S. Smedman, "Air flow behind wind turbines," *Journal of Wind Engineering and Industrial Aerodynamics,* vol. 80, no. 1-2, pp. 169-189, 1999.

[13] A. Bahaj, L. Myers, R. Rawlinson-Smith, and M. Thomson, "The effect of boundary proximity upon the wake structure of horizontal axis marine current turbines," *Journal of Offshore Mechanics and Arctic Engineering*, vol. 134, no. 2, p. 021104, 2012.

[14] A. Crespo and J. Herna, "Turbulence characteristics in wind-turbine wakes," *Journal of wind engineering and industrial aerodynamics*, vol. 61, no. 1, pp. 71-85, 1996.

[15] D.-m. Hu and Z.-h. Du, "Near Wake of a Model Horizontal-Axis Wind Turbine," *Journal of Hydrodynamics, Ser. B*, vol. 21, no. 2, pp. 285-291, 2009.

[16] T. Chen and L. Liou, "Blockage corrections in wind tunnel tests of small horizontal-axis wind turbines," *Experimental Thermal and Fluid Science*, vol. 35, no. 3, pp. 565-569, 2011.

[17] T. Kinsey and G. Dumas, "Impact of channel blockage on the performance of axial and cross-flow hydrokinetic turbines," *Renewable Energy*, vol. 103, pp. 239-254, 2017.

[18] N. Kolekar and A. Banerjee, "Performance characterization and placement of a marine hydrokinetic turbine in a tidal channel under boundary proximity and blockage effects," *Applied Energy*, vol. 148, pp. 121-133, 2015.

[19] H. Yang, W. Shen, H. Xu, Z. Hong, and C. Liu, "Prediction of the wind turbine performance by using BEM with airfoil data extracted from CFD," *Renewable Energy*, vol. 70, pp. 107-115, 2014.

[20] W. Batten, A. Bahaj, A. Molland, and J. Chaplin, "The prediction of the hydrodynamic performance of marine current turbines," *Renewable Energy*, vol. 33, no. 5, pp. 1085-1096, 2008.

[21] J. Chapman, I. Masters, M. Togneri, and J. Orme, "The Buhl correction factor applied to high induction conditions for tidal stream turbines," *Renewable Energy*, vol. 60, pp. 472-480, 2013.

[22] A. S. Bahaj, W. M. J. Batten, and G. McCann, "Experimental verifications of numerical predictions for the hydrodynamic performance of horizontal axis marine current turbines," *Renewable Energy*, vol. 32, no. 15, pp. 2479-2490, 2007.

[23] H. Li, G. A. Taylor, A. M. Abutunis, K. Chandrashekhara, A. R. Kashyap, and J. W. Kimball, "Design and performance evaluation of a hydrokinetic composite turbine system," presented at the SAMPE, Long Beach, CA, 2013.

[24] M. McWilliam and C. Crawford, "The behavior of fixed point iteration and Newton-Raphson methods in solving the blade element momentum equations," *Wind Engineering,* vol. 35, no. 1, pp. 17-32, 2011.

[25] D. C. Maniaci, "An investigation of WT_perf convergence issues," presented at the 49th AIAA Aerospace Sciences Meeting including the New Horizons Forum and Aerospace Exposition, Orlando, FL, January 04 -07, 2011.

[26] I. Masters, J. Chapman, M. Willis, and J. Orme, "A robust blade element momentum theory model for tidal stream turbines including tip and hub loss corrections," *Journal of Marine Engineering & Technology,* vol. 10, no. 1, pp. 25-35, 2011.

[27] S. A. Ning, "A simple solution method for the blade element momentum equations with guaranteed convergence," *Wind Energy,* vol. 17, no. 9, pp. 1327-1345, 2014.

[28] A. Ning, G. Hayman, R. Damiani, and J. M. Jonkman, "Development and validation of a new blade element momentum skewed-wake model within AeroDyn," *33rd Wind Energy Symposium,* pp. 5-9, 2015.

[29] J. Whelan, J. Graham, and J. Peiro, "A free-surface and blockage correction for tidal turbines," *Journal of Fluid Mechanics,* vol. 624, pp. 281-291, 2009.

[30] W. M. J. Batten, A. S. Bahaj, A. F. Molland, and J. R. Chaplin, "Hydrodynamics of marine current turbines," *Renewable Energy,* vol. 31, no. 2, pp. 249-256, 2006.

[31] W. M. J. Batten, A. S. Bahaj, A. F. Molland, and J. R. Chaplin, "Experimentally validated numerical method for the hydrodynamic design of horizontal axis tidal turbines," *Ocean Engineering,* vol. 34, no. 7, pp. 1013-1020, 2007.

[32] T. Hernandez Madrigal, A. Mason-Jones, T. O'Doherty, and D. O'Doherty, "The effect of solidity on a tidal turbine in low speed flow," presented at the 2th European Wave and Tidal Energy Conference (EWTEC), Cork, Ireland, August 27-September 1, 2017. Available: http://orca.cf.ac.uk/id/eprint/105214

[33] C. Thumthae and T. Chitsomboon, "Optimal angle of attack for untwisted blade wind turbine," *Renewable Energy,* vol. 34, no. 5, pp. 1279-1284, 2009.

[34] C. Consul, R. Willden, E. Ferrer, and M. McCulloch, "Influence of solidity on the performance of a cross-flow turbine," in *8th European Wave and Tidal Energy Conference. Uppsala, Sweden*, 2009.

[35] C. Lawn, "Optimization of the power output from ducted turbines," *Proceedings of the Institution of Mechanical Engineers, Part A: Journal of Power and Energy,* vol. 217, no. 1, pp. 107-117, 2003.

[36] B. Kirke, "Developments in ducted water current turbines," *Tidal paper,* no. 25-04, pp. 1-12, 2006.

[37] B. Gilbert and K. Foreman, "Experiments with a diffuser-augmented model wind turbine," *Journal of Energy Resources Technology,* vol. 105, no. 1, pp. 46-53, 1983.

[38] T. Setoguchi, N. Shiomi, and K. Kaneko, "Development of two-way diffuser for fluid energy conversion system," *Renewable Energy,* vol. 29, no. 10, pp. 1757-1771, 2004.

[39] A. Nasution and D. W. Purwanto, "Optimized curvature interior profile for Diffuser Augmented Wind Turbine (DAWT) to increase its energy-conversion performance," *2011 IEEE First Conference on Clean Energy and Technology,* pp. 315-320, 2011.

[40] N. Stergiannis, C. Lacor, J. Beeck, and R. Donnelly, "CFD modelling approaches against single wind turbine wake measurements using RANS," in *Journal of Physics: Conference Series* 753 032062, vol. 753, no. 3, pp. 1-16, 2016

[41] R. J. Stevens, L. A. Martínez-Tossas, and C. Meneveau, "Comparison of wind farm large eddy simulations using actuator disk and actuator line models with wind tunnel experiments," *Renewable Energy,* vol. 116, pp. 470-478, 2018.

[42] L. P. Chamorro, D. R. Troolin, S.-J. Lee, R. E. A. Arndt, and F. Sotiropoulos, "Three-dimensional flow visualization in the wake of a miniature axial-flow hydrokinetic turbine," *Experiments in Fluids,* vol. 54, no. 2, pp. 1-12, 2013.

VITA

Abdulaziz Abutunis was born in Sebha, Libya. He received his B.S. degree with honors in Mechanical Engineering in May 1997 from the College of Engineering Technology, Houn, Libya (Formerly the Higher Institute of Engineering).

In March 1999, he joined as a Technical Engineer in a textile factory. From March 2004 to November 2006, he worked as a Technical Engineer involved in maintaining and renewing subsidiary and main sewage stations in Sabha, Libya. The project was led by Alnafitha and Chemistry & Technology Company. From September 2007 to February 2008, he worked as an Assistant Mechanical Engineer for a water supply trail program in Libya. The project was led by Chemistry & Technology Company and CASON Engineering Plc. In March 2008, Abdulaziz joined the College of Engineering Technology, Houn, Libya. He worked as a Laboratory Instructor until May 2010.

Abdulaziz joined Missouri University of Science and Technology, Rolla, Missouri, USA in August 2011. He worked as a Graduate Teaching Assistant at Missouri University of Science and Technology. He received his Master's Degree in December 2014. Since January 2015, Abdulaziz Abutunis has been enrolled in the Ph.D. program at Missouri University of Science and Technology. He held both the Graduate Research Assistant and the Graduate Teaching Assistant positions throughout his Ph.D. program. In May 2020, he received his Ph.D. degree in Mechanical Engineering from Missouri University of Science and Technology.

.